EBERHARD KARLS
UNIVERSITÄT
TÜBINGEN

Zentrum für Angewandte Geowissenschaften (ZAG)

TÜBINGER GEOWISSENSCHAFTLICHE ARBEITEN (TGA)

Reihe C: Hydro-, Ingenieur- und Umweltgeologie

Schriftleitung: P. Grathwohl, G. Teutsch

Martin Beinhorn

Contributions to computational hydrology

Non-linear flow processes in subsurface and surface hydrosystems

TGA, C90, 2005

Contributions to computational hydrology

Non-linear flow processes in subsurface and surface hydrosystems

Dissertation

zur Erlangung des Grades eines Doktors der Naturwissenschaften

der Geowissenschaftlichen Fakultät

der Eberhard-Karls-Universität Tübingen

vorgelegt von

MSc. BSc. Martin Beinhorn

aus Bad Sobernheim

2005

Tag der mündlichen Prüfung: 10.06.2005

Dekan: Prof. Klaus G. Nickel, Ph.D.

1. Berichterstatter: Prof. Dr.-Ing. Olaf Kolditz

2. Berichterstatter: Prof. Dr.sc.techn. Hans-Jörg Diersch

Herausgeber: Institut für Geowissenschaften der Universität Tübingen
Sigwartstraße 10, D-72076 Tübingen

Schriftleitung der Reihe C: Zentrum für Angewandte Geowissenschaften (ZAG)
Lehrstuhl für Angewandte Geologie

Prof. Dr. Thomas Aigner
Prof. Dr. Erwin Appel
Prof. Dr. Peter Grathwohl
Prof. Dr. Stefan Haderlein
Prof. Dr.-Ing. Olaf Kolditz
Prof. Dr. Georg Teutsch

Redaktion: Dipl.-Geol. Björn Sack-Kühner

ISSN 0935-4948 (Print)
ISSN 1610-4706 (Internet)

Zusammenfassung

Zielsetzung des Fachgebietes Computational Hydrology ist die Entwicklung und Verbesserung mathematischer und numerischer Methoden zur Betrachtung natürlicher Hydrosysteme. Die Methoden dienen der Verbesserung des Systemverständnisses und machen Prognoseaussagen hinsichtlich des Systemverhaltens möglich. Ein natürliches Hydrosystem besteht aus den Teilsystemen Grund- und Oberflächenwasser, die gegenseitiger Wechselwirkung unterliegen. Wechselwirkungen werden in einem numerischen Modell durch die Kopplung verschiedener Prozesse berücksichtigt. Die vorliegende Arbeit behandelt zunächst die Komponenten Grundwasser und Oberflächenwasser als isolierte Systeme, ist aber in folgendem Kontext zu sehen: Die neu erstellten Programmteile, die nun Teil des Finiten Elemente Programms GeoSys/ RockFlow bilden, dienen dem ferneren Ziel ein Programmsystem anzubieten, das eine ganzheitliche Betrachtungsweise natürlicher Hydrosysteme mit den beiden Teilsystemen Grund- und Ober- flächenwasser innerhalb eines integrierenden numerischen Modells möglich macht.

Hydrogeologische Systeme können aufgrund ihres Schichtaufbaus zumeist gut mit Dreiecksprismen diskretisiert werden. Ein weiterer Vorteil der Dreiecksprismen ist, dass eine numerische Quadratur nicht erforderlich ist und die Integrationen geschlossen durchführbar sind. Deshalb wurde der neue Elementtyp unter Verwendung der analytischen Integration implementiert. Die Prozesse Grundwasserströmung und Transport sind dabei berücksichtigt. Eine Überprüfung der neuen analytischen Methode erfolgte anhand eines Vergleichs der Lösungen mit dem herkömmlichen numerischen Verfahren sowie teilweise anhand analytischer Lösungen. Die Leistungsfähigkeit des analytischen Verfahrens wurde mit einem Transport Rechenbeispiel überprüft. Im Vergleich zu der herkömmlichen numerischen Methode wurde die Berechnungszeit zum Aufbau der Elementmatrizen auf ein fünftel verkürzt. Da oftmals ungespannte Systeme berücksichtigt werden müssen, wurde die Grundwasserströmung auch im ungespannten Aquifer modelltechnisch umgesetzt. Dafür wurde die Methode der beweglichen Gitterknoten verwendet, die mit Hilfe einer Picard Iteration realisiert wurde. Die Verifizierung dieser Methode erfolgte ebenfalls anhand einer analytischen Lösung.

Oberflächenabfluss ist eine wichtige Komponente eines Hydrosystems und wurde deswegen als weiterer Prozess in das bestehende Programm aufgenommen. Die Strömung wird dabei mit einer Diffusions-Wellengleichung, einer vereinfachten Form der Flachwassergleichungen, beschrieben. Modellergebnisse wurden wiederum anhand einer analytischen Lösung verifiziert oder mit Ergebnissen eines anderen numerischen Models verglichen.

Anwendungsbeispiele sind die Modellierung eines geringmächtigen Aquifers im Gebiet um Jericho, die Bewertung von Dichteffekten auf die Ausbreitung einer Tracerwolke anhand einer Modellstudie und die Modellierung eines 3-schichtigen Aquifersystems in Jordanien.

Summary

Research in computational hydrology aims at the development and improvement of mathematical and numerical methods used to understand and predict the behavior of hydrologic systems. A hydrologic system consists of a subsurface- and a surface system, both interacting to various degrees. Interaction of different system components is achieved by process coupling and has received considerable attention by the modelling community. The issue of process coupling is not addressed in this work. The work presented here deals with subsurface- and surface systems as stand alone components, but is to be looked at in a wider context: The new features incorporated into the finite element (FE) program GeoSys/RockFlow (Kolditz et al. (2003)) serve to achieve the overall aim to create a software package to simulate large scale hydrologic systems within one integrating numerical model by closing some existing gaps of the program version from 2002.

Due to the layered structure of most subsurface systems they can best be discretized with triangular prismatic elements. The computationally most efficient method for the calculation of their element matrices is the analytical integration of element matrix expressions. Hence triangular prismatic elements were implemented using an analytical integration for the element matrix expressions. The porous medium processes fluid flow and tracer transport were considered. The new method was crosschecked using results of the traditional numerical evaluation scheme and partly verified with analytical results. The performance of the new method was evaluated using a transport example. A comparison of the new analytical method with the traditional numerical method did show that the computation time required for setting up the element matrices is reduced by a factor 0.2. Hydrogeological systems are often formed by unconfined aquifers so that the model must be capable to properly represent unconfined groundwater flow. A method to calculate unconfined groundwater flow was therefore implemented into the existing simulator GeoSys/RockFlow. The method chosen is the moving mesh approach realized with a Picard iteration. The implemented method was also verified using analytical results. The next important process on the land phase of the hydrological cycle that has been implemented is overland

flow. Based on a literature study a choice has been made in favor of the diffusive wave approach. Results were compared to analytical solutions and crosschecked with results from another numerical model.

Application examples are a modelling study of a shallow aquifer in the Jericho area, the numerical evaluation of density effects on tracer tests and a modelling study of a multi layer aquifer system in central Jordan.

Acknowledgements

I would like to thank Dr.-Ing. Olaf Kolditz for the supervision of my work. I will not forget his never ending optimism and enthusiasm. Thanks also go to Prof. Dr.sc.techn. Hans-Jörg Diersch for the amount of time he allocated to review the thesis and for his hints and suggestions. I would also like to extent my appreciation to Prof. Dr. Martin Sauter who put forward the GIJP project. And finally I want to thank my colleagues of the working group. In particular I am indebted to Wenqing Wang, the master of math, for sharing some of his knowledge of FEM and C++.

Contents

List of Figures

List of Tables

1 Introduction

Research in computational hydrology aims at the development and improvement of mathematical and numerical methods used to understand and predict the behavior of hydrologic systems. A hydrologic system consists of a subsurface- and a surface system, both interacting to various degrees. Interaction of different system components is achieved by process coupling and has received considerable attention by the modelling community recently (eg. Gunduz and Aral (2005), Hydrosphere (2004), WASY (2005), HYDROGeoLogic (2005) and IGSM (2005)). The issue of process coupling is not addressed in this work. The work presented here deals with subsurface- and surface systems as stand alone components, but is to be looked at in a wider context: The new features incorporated into the finite element (FE) program GeoSys/RockFlow (Kolditz et al. (2003)) serve to achieve the overall aim to create a software package to simulate large scale hydrologic systems including dynamic coupling of ground- and surface water processes by closing some existing gaps of the program version from 2001.

Subsurface systems can best be discretized with triangular prismatic elements and the computationally most efficient method for the calculation of their element matrices is the analytical integration of element matrix expressions. Hence the first aim of the study is to implement prismatic elements using an analytical integration for the element matrix expressions. As hydrogeological systems can be formed by unconfined aquifers the model must be capable to properly represent unconfined groundwater flow. Hence, the second aim of the study is to implement a method to calculate unconfined groundwater flow. The next process not considered in the program version of 2001 is overland flow even though it is an important process on the land phase of the hydrological cycle. It controls streamflow generation via Horton or Dunne overland flow during rainfall runoff events and impacts groundwater recharge when flooding occurs. The implementation of the new overland flow component is therefore an essential step towards developing a physically based, spatially distributed modelling tool. Following objectives were identified and pursued in order to accomplish these aims:

- To gain an understanding of the FE Method.
- To gain an understanding of the programming language C and object oriented programming concept.
- To gain an understanding of the existing FE simulator RockFlow.
- To derive the equations for the analytical integration of element matrix expressions.
- To implement triangular prismatic elements and their analytic evaluation for the element matrix expressions.

- To implement a method to calculate unconfined groundwater flow.
- To implement the process of overland flow.

The first three objectives do not lead to presentable results. However they are prerequisites for the programming work done and are therefore considered as major achievements accomplished during the research. The presentable part of the work is outlined in this report: Section 2 gives a broad overview of the theory of linear and non-linear groundwater flow, overland flow and channel flow. Section 3 contains a description of the numerical methods used for the implementation, the finite element method and the finite difference approach. The chapter is based on literature, mainly Kolditz (2002), and serves as an introduction to the programming work done. Section 4 deals with the program concept which constitutes the framework for the implementation of new processes and features. In section 5 different test examples that were used to verify new program parts are presented. A variety of program applications are shown in section 6.

Some of the work is also documented in technical reports, publications at conferences and submitted papers. These documents are referred to at places. A list of publications is given in section 9.8.

2 Theory

2.1 Linear groundwater flow

Fundamental to understanding the porous medium processes groundwater flow and transport is the continuum approach. The concept is described below together with the processes to be considered and their governing equations.

Porous medium flow and transport

In a porous medium the material parameters change rapidly at a microscopic scale. It becomes impossible to describe the complex geometry of the solid matrix at a microscopic level. Therefore all material parameters are averaged over a larger volume performing a transition to the macroscopic scale. The volume which is sufficiently big to describe the porous medium at that scale is called representative elementary volume (REV), see Fig. 1. Material parameters such as porosity, storativity, permeability, dispersivity etc. and the mathematical formulations used in the following sections are based on the REV concept. We now have created a macroscopic model in a procedure called the continuum approach. Groundwater flow is the movement of water through the porous medium as a result of gravity and external pressure counteracted by shear-forces resulting from the fluid viscosity. Flow is assumed to be laminar and dominated by advective transport, i.e. diffusive fluxes can be neglected. The fluid phase may carry solutes resulting in advective transport of solutes. Also, solutes move via diffusion forced by concentration gradients. Additional mixing of solutes occurs as a consequence of dispersion. Details of groundwater flow and transport theory are given in Bear (1972), Diersch (1985) and Bear and Bachmat (1990).

Mathematical model

Following Hassanizadeh and Leijnse (1988) the simplified form of the mass balance equation of the fluid phase is given by

$$S_0^p \frac{\partial p}{\partial t} + \nabla \cdot \mathbf{q} = Q_\rho \tag{1}$$

with the specific storativity of the porous medium S_0^p, the Darcy velocity vector $\mathbf{q}$ and a source term Q_ρ. The simplification consists of introducing the Boussinesq approximation, i.e. density variations within the mass balance equation of the fluid phase are neglected, but are included by the buoyancy term of the Darcy equation (see Diersch and Kolditz (2002) and Kolditz et al. (1998) for details). Darcy's equation gives an expression for $\mathbf{q}$ and can be written in terms of pressure

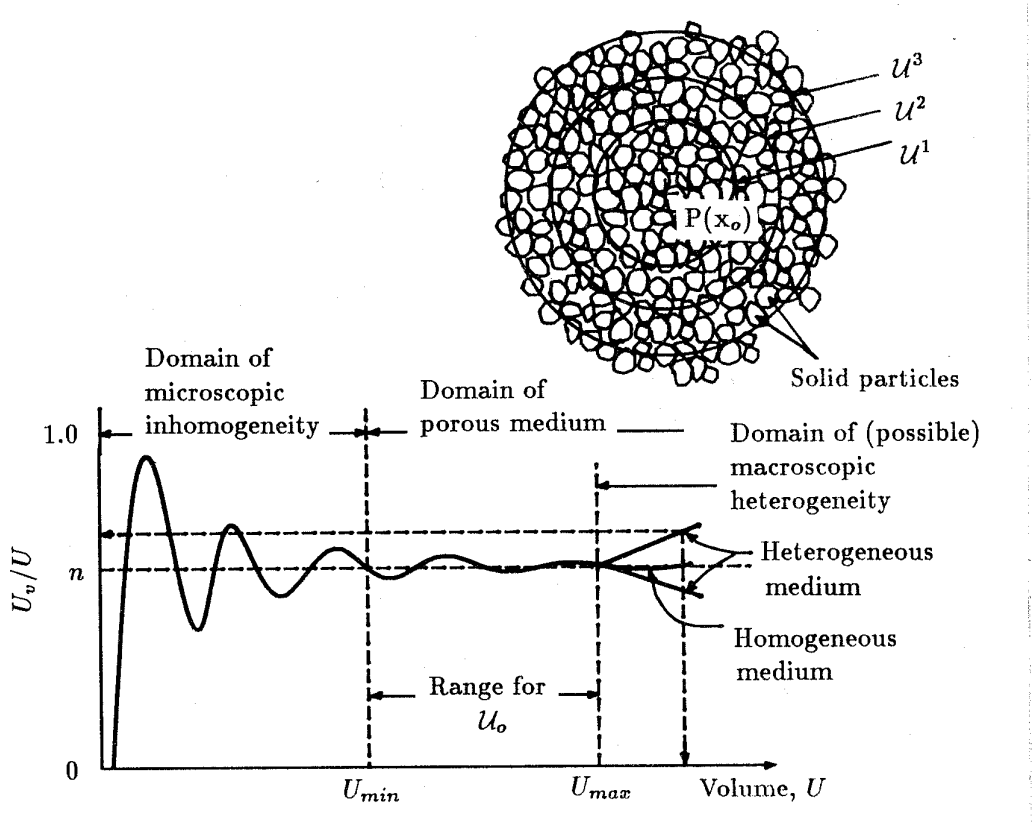

Figure 1: Representative elementary volume (REV), Bear and Bachmat (1990)

or hydraulic head

$$\mathbf{q} = -\mathbf{K} \cdot \left(\nabla h - \frac{\rho - \rho^w}{\rho^w} \frac{\mathbf{g}}{|g|} \right) = -\frac{\mathbf{k}}{\mu} \cdot (\nabla p - \rho \mathbf{g}) \tag{2}$$

where $\mathbf{k}$ the tensor of permeability, $\mathbf{K}$ the tensor of hydraulic conductivity, μ fluid viscosity, ρ mass density of the fluid, ρ^w mass density of water, p dynamic pressure, h hydraulic heads and $\mathbf{g}$ the gravity vector.

A corresponding mass balance equation of solute mass conservation written in terms of mass concentrations is

$$\frac{\partial nC}{\partial t} + \nabla \cdot (\mathbf{v} nC) - \nabla \cdot (n\mathbf{D} \cdot \nabla C) = Q_C \tag{3}$$

where $\mathbf{v}$ is the pore velocity vector given by $\mathbf{q}/n$, Q_C is a source term of the solute component and $\mathbf{D}$ is the hydrodynamic dispersion tensor according to Bear (1972) given by

$$\begin{aligned} \mathbf{D} &= D_d \mathbf{I} + \mathbf{D}_m \\ \mathbf{D}_m &= \alpha_L |\mathbf{v}| \mathbf{I} + (\alpha_L - \alpha_T) \frac{\mathbf{v} \otimes \mathbf{v}}{|\mathbf{v}|} \end{aligned} \tag{4}$$

where D_d is a coefficient of molecular diffusion, $\mathbf{I}$ is the identity tensor, $\mathbf{D}_m$ is the tensor of mechanical dispersion, $\otimes$ denotes the dyadic product and α_L and α_T are the longitudinal and transverse dispersivities respectively.

2.2 Non-linear groundwater flow

2.2.1 Unsaturated groundwater flow

The most rigorous approach to model flow through an unsaturated porous medium would be to represent fluid flow and flow of air in an multiphase model (eg. Helmig (1993) Thorenz (2001) or Kolditz and de Jonge (2004)). Another method would be to use the Richards approximation (Richards (1931)) which means essentially a simplified formulation of a multiphase flow problem. Richards equation is given below

$$S_0^p Sa \frac{\partial \rho}{\partial t} + n \frac{\partial Sa}{\partial t} + \nabla \cdot (\frac{k_{\mathsf{rel}} \mathbf{k}}{\mu} \cdot (\nabla p - \rho \mathbf{g})) = Q_\rho \tag{5}$$

with the relative permeability k_{rel} as a function of the saturation Sa. The parametric functions used in this approach are based on work of Brooks and Corey (1964), Haverkamp et al. (1977) and Van Genuchten (1980) and are briefly described below:

Capillary pressure–p_{c}

The capillary pressure can be defined as the tendency of a porous medium to suck in the wetting fluid phase or to repel the non-wetting phase. Capillary pressure results from the pressure discontinuity at the interface between two immiscible fluids. It depends on the geometry of the void space, on the nature of solids and liquids and on the degree of saturation. In porous media the geometry of the void space is idealized. Thus, the dependence reduces to saturation for any given porous media. Care has to be taken, as capillary pressure is not the same for drainage and re-wetting. The function connecting capillary pressure and saturation has to be determined by laboratory experiments for every new porous medium. As an approximation a linear relationship can be used. There are, however, analytical functions that can be used, such as given in Van Genuchten (1980)

$$Sa_{\mathsf{eff}} = \frac{Sa^w - Sa_r^w}{1 - Sa_r^w} = (1 + (\alpha\, p_{\mathsf{c}})^n)^m \qquad , \qquad p_{\mathsf{c}} > 0 \tag{6}$$

$$p_{\mathsf{c}} = \begin{cases} 0 & Sa^w > Sa_{\mathsf{max}}^w \\ \frac{\rho^w g}{\alpha} (Sa_{\mathsf{eff}}^{-1/m} - 1)^{1/n} & Sa_r^w < Sa^w < Sa_{\mathsf{max}}^w \\ p_{\mathsf{c\ max}} & Sa^w < Sa_r^w \end{cases} \tag{7}$$

Brooks and Corey (1964) developed another equation to relate capillary pressure to saturation

$$Sa_{\mathsf{eff}} = \frac{Sa^w - Sa_r^w}{1 - Sa_r^w} = \left(\frac{p_b}{p_{\mathsf{c}}}\right)^{\lambda} \qquad , \qquad p_{\mathsf{c}} \geq p_b \tag{8}$$

$$p_{\mathsf{c}} = \begin{cases} 0 & Sa^w > Sa^w_{\mathsf{max}} \\ p_b \left(\frac{1}{Sa_{\mathsf{eff}}}\right)^{1/\lambda} & Sa_r^w < Sa^w < Sa^w_{\mathsf{max}} \\ p_{\mathsf{c\ max}} & Sa^w < Sa_r^w \end{cases} \tag{9}$$

where p_b is the so-called bubbling pressure, the minimum pressure at which the gaseous phase exists, λ is the pore size distribution index.

Another model is that of Haverkamp et al. (1977), where the formulas are given in terms of pressure head $h = p^w/g\rho^w$ and moisture content $\theta = nSa^w$. Parameters for that model are summarized in Table 1.

$$\theta = \frac{\alpha(\theta_s - \theta_r)}{\alpha + |h|^{\beta}} + \theta_r \tag{10}$$

$$h = \left(-\frac{\alpha}{\theta}(\theta - \theta_s + \theta_r)\right)^{1/\beta} \tag{11}$$

θ	volumetric water (moisture) content		$[cm^3/cm^3]$
θ_r	residual volumetric water content	0.075	$[cm^3/cm^3]$
θ_s	saturated volumetric water content	0.287	$[cm^3/cm^3]$
$h(\theta)$	soil water pressure head relative to the atmosphere		$[cm]$
α		1.611×10^6	$[Pa^{-1}]$
β		3.96	

Table 1: Model parameters for the Havercamp model

Relative permeability–k_{rel}

For a partially saturated porous medium the concept of relative permeability is introduced. The relative permeability is used to calculate the effective permeability $(k_{\mathsf{rel}}^{\gamma} Sa^{\gamma})\mathbf{k}$ and strongly depends on the saturations. Different relationships can be specified: user-defined functions, linear functions, potential functions, or functions found in literature, such as the van Genuchten Model (Van Genuchten (1980)) as shown in an exemplary graph in Fig. 2.

$$k_{\mathsf{rel}}(h) = \frac{1-(\alpha h)^{n-2}\left[1+(\alpha h)^{n}\right]^{-m}}{\left[1+(\alpha h)^{n}\right]^{2m}} \tag{12}$$

or the relationship developed by Haverkamp et al. (1977)

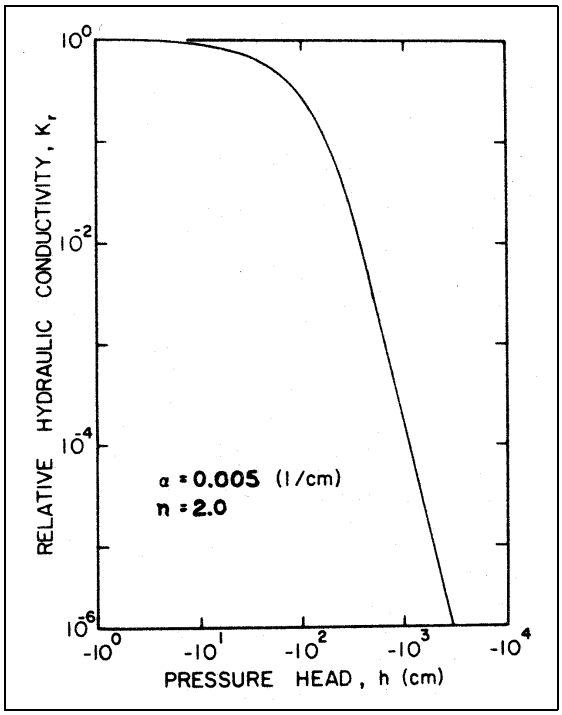

Figure 2: Relative permeability functions, Van Genuchten (1980)

$$k_{\mathsf{rel}}(h) = K_s \frac{A}{A+|h|^{\beta}} \tag{13}$$

$$h = \left(-\frac{\alpha}{\theta}(\theta-\theta_s+\theta_r)\right)^{1/\beta} \tag{14}$$

or the Brooks and Corey (1964) model

$$Sa_{\mathsf{eff}} = \frac{Sa^{w}-Sa_r^{w}}{Sa_{\mathsf{max}}^{w}-Sa_r^{w}} \tag{15}$$

$$k_{\mathsf{rel}}^{w} = S a_{\mathsf{eff}}^{4} \tag{16}$$

2.2.2 Unconfined groundwater flow

A confined aquifer is bounded above and below by impervious formations. The aquifer is completely saturated. An unconfined aquifer is only partially saturated and the water table separates the saturated from the unsaturated zone. The water table or free surface is defined as the region where pore water pressure equals atmospheric pressure. The most rigorous approach to model an unconfined aquifer would be to represent fluid flow and flow of air in an multiphase model (eg. Kolditz and de Jonge (2004)). Another method would be to use the Richards approximation which means essentially a simplified formulation of a multiphase flow problem. Both methods are computationally expensive and require difficult-to obtain data like initial saturation states or a function relating capillary pressure with saturation. For large areas it becomes impossible to obtain such data so that in groundwater modelling, especially for regional groundwater models, a simplified process model is preferred: Only the saturated zone is considered. As the water table may vary through time the boundary of the modelled domain is a moving boundary. The same set of equations as for the confined aquifer can be used only that the boundaries are changing, i.e. we deal with a kinematic boundary condition. In terms of groundwater modelling the simplified process model results in two different modelling approaches:

Most groundwater flow modelling is carried out using two-dimensional, vertically integrated models. The governing Boussinesq equation accounts for changes in saturated thickness by changes in transmissivity. The mesh can stay fixed during the process; hence the name 'fixed mesh approach'. In the second approach, used for three-dimensional models, the elevation of the top of the grid system is set to be equal to the water table. This is achieved by lengthening or shortening of elements, i.e. moving of mesh nodes; hence the name moving mesh approach. Problems associated with the moving mesh approach include the numerical stability in cells with large aspect ratios. One solution is to adjust element width as well as element height as proposed by Fenton and Griffiths (1997) or to generate or delete new elements as the deformation of cells reaches a certain threshold (Crow et al. (1999)). Another difficulty arises if we deal with stratified aquifers and mesh distortion results in distortion of the original geometry. The method proposed by Diersch (2001a) ensures the hydrostratigraphical consistence of multilayered systems throughout the simulation. The idea is to adapt the moving mesh as best as possible to the original geometry.

2.2.3 Density dependent flow

Considerable research on variable-density flow in porous media has been done during the last 30 years. A comprehensive review of the subject and the related

issue of benchmarking is given in Diersch and Kolditz (2002) and in the textbooks Nield and Bejan (1999) or Holzbecher (1998) . Oswald and Kinzelbach (2004) designed the most recent three-dimensional physical benchmark experiment to test numerical variable-density flow models and Weatherill et al. (2004) suggest several further test cases. Other examples used as benchmarks to test numerical models are given in Diersch (2002). The subject of variable-density flow in heterogeneous porous media is addressed in Simmons et al. (2001).

Density dependent flow is also described by equations 1and 2, but now the density of the fluid ρ is a function of solute concentration C and can be approximated by

$$\rho = \rho^w + C \tag{17}$$

Effects of temperature and pressure variations on density can be disregarded. Variations in fluid viscosity μ do influence both the vertical and the horizontal flow component and therefore are assumed to be negligible when examining density effects.

2.2.4 Fracture flow

Based on Forchheimer's law the following generalization of Darcy's law for non-linear laminar fracture flow is used.

$$\mathbf{q} = -\mathbf{K}(h, \nabla h)\nabla h \tag{18}$$

This means that the hydraulic conductivity becomes dependent on head and velocity itself. The non-linearity basically results from inertial effects, e.g. due to flow channelling in rough fractures (see Kolditz (2001)).

2.3 Overland flow

Overland flow is an important process on the land phase of the hydrological cycle. It controls streamflow generation via Horton or Dunne overland flow during rainfall runoff events and impacts groundwater recharge when flooding occurs. Implementation of the new overland flow component is therefore an essential step towards developing a physically based, spatially distributed modelling tool that allows for dynamic coupling between the ground- and surface water component. This section contains a description of the mathematical model of the overland flow process.

Mathematical model

The two dimensional shallow water equations are derived from the Navier-Stokes equations by integrating over the depth using kinematic boundary conditions. Underlying assumptions are: pressure distribution is hydrostatic and horizontal shear stresses are small (see Rijn (1986), Vreugdenhil (1994) or Jain (2001) for details). As a result we have the fully dynamic unsteady flow equations given by the mass balance equations

$$\frac{\partial h}{\partial t} + \frac{\partial (uH)}{\partial x} + \frac{\partial (vH)}{\partial y} = Q_\rho \tag{19}$$

and the two momentum equations

$$\frac{\partial (uH)}{\partial t} + \frac{\partial (u^2 H)}{\partial x} + \frac{\partial (uvH)}{\partial y} + gH\frac{\partial h}{\partial x} + gHS_{fx} = 0 \tag{20}$$

$$\underbrace{\underbrace{\frac{\partial (vH)}{\partial t} + \frac{\partial (v^2 H)}{\partial y} + \frac{\partial (uvH)}{\partial x} + gH\frac{\partial h}{\partial y}}_{diffusive\ wave} + \underbrace{gHS_{fy} = 0}_{kinematic\ wave}}_{fully\ dynamic\ wave} \tag{21}$$

, where H is the water depth, h is the hydraulic head ($h = H + z$), $S_f x$ and $S_f x$ are the friction slopes in x- and y-direction, g is acceleration due to gravity, Q_ρ a source term and v and u are depth averaged flow velocities. Depending on the simplifications introduced to these equations three different models can be distinguished. Fully dynamic models solve the complete equation. Neglecting the acceleration terms leads to a non-linear diffusion equation, also called diffusive wave or zero-inertia approach. A further simplification consists of neglecting the gradient of hydraulic head, i.e. setting the bottom slope equal to the friction slope which results in the kinematic wave approach (eg. Schmitz et al. (2002)). In the systems to be looked at we deal with slow regional flow dynamics in low gradient situations so that both the kinematic and diffusive wave approaches seem appropriate. (The conditions under which complete St. Venant equations have to be used can be determined using the guidelines proposed by Ponce et al. (1978)). However, a basic assumption of the kinematic wave approach is that the downstream boundary condition does not have an effect on overland flow (Morgali (1970)), so that the method does not allow for backfacing slopes in the flow field. The limitation of not being able to model backwater effects does not exist for the diffusive wave approach so that the diffusive wave approach has been chosen as proposed by Xanthopoulos and Koutitas (1976) and also chosen in the

studies by (Hromadka et al. (1985), Hromadka et al. (1987) Hromadka and Yen (1987), Abbott et al. (1987a), Abbott et al. (1987b), Govindaraju et al. (1988), Zang and Cundy (1989), Giammarco et al. (1996), Feng and Molz (1997) and VanderKwaak and Loague (2001). As a result of the simplification the equations are not hyperbolic and the resulting parabolic equations easier and faster to solve numerically (Ames (1992)). Using the diffusion approach the momentum equations (equations 20 and 21) are replaced by

$$S_{fx} + \frac{\partial h}{\partial x} = 0 \qquad and \qquad S_{fy} + \frac{\partial h}{\partial y} = 0 \tag{22}$$

so that the friction slopes $S_f x$ and $S_f x$ and the slope of the water surface $\frac{\partial h}{\partial x}$ and $\frac{\partial h}{\partial y}$ become the same. As shown in (Giammarco et al. (1996) and Hromadka et al. (1985)) applying the Manning-Strickler law which relates water depth to flow velocity the velocity components u and v can be expressed using

$$u = -\frac{\partial h}{\partial x} \quad \frac{H^{2/3}}{n^2} \quad \frac{1}{\left[\left(\frac{\partial h}{\partial x}\right)^2 \frac{1}{n^4} + \left(\frac{\partial h}{\partial y}\right)^2 \frac{1}{n^4}\right]^{1/4}} \tag{23}$$

$$v = -\frac{\partial h}{\partial y} \quad \frac{H^{2/3}}{n^2} \quad \frac{1}{\left[\left(\frac{\partial h}{\partial x}\right)^2 \frac{1}{n^4} + \left(\frac{\partial h}{\partial y}\right)^2 \frac{1}{n^4}\right]^{1/4}} \tag{24}$$

where n is the Manning-coefficient. Now the variable k_{eq} is introduced with

$$k_{eq} = \frac{H^{2/3}}{n^2} \quad \frac{1}{\left[\left(\frac{\partial h}{\partial x}\right)^2 \frac{1}{n^4} + \left(\frac{\partial h}{\partial y}\right)^2 \frac{1}{n^4}\right]^{1/4}} = \frac{H^{2/3}}{n^2} \frac{1}{Ss^{1/4}} \tag{25}$$

so that the velocities can be expressed as

$$u = -\frac{\partial h}{\partial x} \quad k_{eq} \tag{26}$$

$$v = -\frac{\partial h}{\partial y} \quad k_{eq} \tag{27}$$

Now using these expressions for velocities in the mass balance equation (equation 19) yields the governing equation

$$\frac{\partial h}{\partial t} + \frac{\partial}{\partial x}\left(k_{eq}\frac{\partial h}{\partial x}H\right) + \frac{\partial}{\partial y}\left(k_{eq}\frac{\partial h}{\partial y}H\right) = Q_\rho \tag{28}$$

which is similar to a flow equation employed to solve 2-dimensional unconfined flow or unsaturated flow using Richards equation. The equation is therefore easy to implement in an existing groundwater flow model.

Chézy-coefficient

Another formula relating water depth to flow velocity is the Chézy-formula which in addition to the Manning-formula is often being used in open channel flow calculations. Both involve empirically determined roughness parameters, the Chézy-coefficient C and the Manning-coefficient n. For open channel flow they are related with

$$C = R^{\frac{1}{6}} * n^{-1}$$

where R is the hydraulic radius $R = A/P$ where A is the wetted cross-sectional area and P is the wetted perimeter. Overland flow resembles a wide channel with a channel width b much bigger than the water depth H ($b >> H$). For that case the hydraulic radius tends toward H so that the 'conductivity equivalent' K_{eq} in equation 25 can also be expressed in terms of C using

$$n = H^{\frac{1}{6}} C^{-1}$$

Analytical solutions

As overland flow resembles a wide channel with a channel width much bigger than the water depth we can use an analytical solution derived from 1-dimensional free surface channel flow. According to Rijn (1986) there is an analytical solution to the steady state flow equation for the special case of flow over a horizontal bed given by

$$x_1 = x_0 + \frac{C^2}{g}(H_1 - H_0) - \frac{C^2}{4q^2}(H_1^4 - H_0^4) \tag{29}$$

where x_0 is the location where the boundary condition $H = H_0$ is known and x_1 is the location where the water depth H is equal to H_1.

Boundary conditions

A minimum specific energy or specific head is required to maintain a given flow in a given shape of cross section. The water depth at the minimum specific energy is called critical depth H_c. If the water depth is bigger than the critical depth we have a subcritical flow regime. According to Jain (2001) or Rijn (1986) the critical depth for rectangular channels can be written as

$$H_c = \sqrt[3]{\frac{q^2}{g}} \tag{30}$$

Using that equation we can therefore define a dynamic boundary condition at an outflow point under the assumption of a subcritical flow regime.

The flow upstream from control structures such as weirs, spillways and sluice gates is also subcritical. A unique relation between the elevation of the water surface at a particular section and the discharge, similar to that between discharge and critical depth, exists for these structures (see Jain (2001) for details). This relation can also serve as a boundary condition in channel flow computations.

Due to local irregularities in the land surface elevation a minimum water depth is required before overland flow is initiated. Hence a minimum water depth, which reflects local storage, can be specified.

2.4 Channel flow

Channel flow comprises flow of water in rivers, canals, sewers and drains. It controls surface runoff from rainfall over land, river stage during floods and the behavior of irrigation networks and therefore constitutes an important part of the hydrological cycle. This section contains a description of the mathematical model of channel flow.

Mathematical model

To describe river flow the shallow water equations (see equations 19, 20 and 21) are used in a one-dimensional form. For channel flow the equations are derived by averaging the Navier-Stokes equations over the river cross-section (see Rijn (1986), Vreugdenhil (1994) or Jain (2001) for details). The one-dimensional shallow water equations can now be written in terms of cross sectional area A and volumetric discharge Q as primary variables

$$\frac{\partial A}{\partial t} + \frac{\partial Q}{\partial s} = 0 \tag{31}$$

$$\frac{\partial}{\partial t}\left(\frac{Q}{A}\right) + \frac{\partial}{\partial s}\left(\frac{Q^2}{2A^2} + gh(s,A)\right) = g(S_0 - S_f) \tag{32}$$

or in terms of water depth h

$$\frac{\partial}{\partial t}A(s,h) + \frac{\partial}{\partial s}[A(s,h)u] = 0 \tag{33}$$

$$A(s,h) = a(s)h + b(s)h^2 \tag{34}$$

and velocity v, respectively

$$a\frac{\partial h}{\partial t} + b\frac{\partial h^2}{\partial t} + \frac{\partial}{\partial s}(au\,h + bu\,h^2) = 0 \tag{35}$$

$$(a + 2bh)\frac{\partial h}{\partial t} + \frac{\partial}{\partial s}(au\,h + bu\,h^2) = 0 \tag{36}$$

$$\frac{\partial u}{\partial t} + \frac{\partial}{\partial s}\left(\frac{u^2}{2} + gh\right) = g(S_0 - S_f) \tag{37}$$

$$\frac{\partial u}{\partial t} + u\frac{\partial u}{\partial s} + g\frac{\partial h}{\partial s} = g(S_0 - S_f) \tag{38}$$

Note that the velocity can be regarded as a scalar function along the river line. We use the $h-v$ formulation to be consistent with the subsurface flow equations. For steady state flow the equations can be further simplified, i.e. time derivatives are zero and discharge is assumed to be constant so that

$$\frac{\partial}{\partial s}\left(\frac{u^2}{2} + gh\right) = g(S_0 - S_f) \tag{39}$$

The velocity is then simply a function of water depth.

$$u = \frac{Q}{A(h)} \tag{40}$$

Substituting this relationship into equation 39 an expression for the water depth can be obtained, which is non-linear with respect to h.

$$\frac{d}{ds}\left(\frac{Q^2}{2A^2(s,h)} + gh\right) = gS_0 - gS_f(s,h) \tag{41}$$

Details of the river flow model can be found in Liedl (2004).

3 Numerical methods

The governing equations describing the different non-linear subsurface and surface water processes described in the previous section cannot be solved as they stand. Especially for problems with complex geometry or changing boundary conditions, exact solutions usually do not exist, and approximate solutions must be obtained. For such problems the use of numerical methods is advantageous. Fig. 3 gives an overview on a variety of different approximation methods.

To obtain a numerical approach of the surface- and subsurface processes given in a hydrosystem a combination of finite element method and finite difference method is applied. The equations describing the porous medium processes groundwater flow and transport as well as overland flow (equations 1, 3 and 28) are solved using the finite element method. The equation describing channel flow (equation 41) is solved using the finite difference method. Both method are described in the next sections.

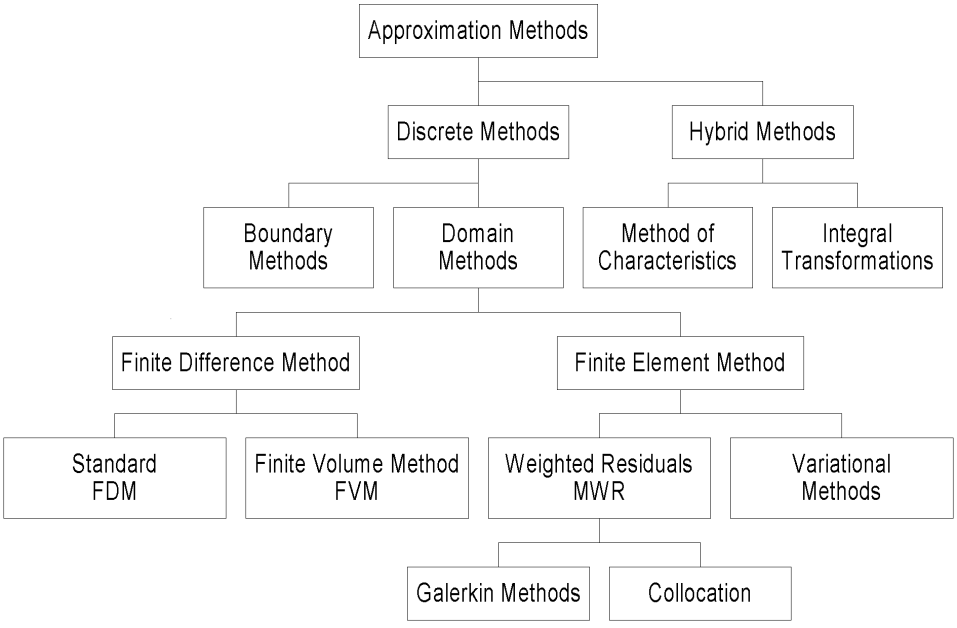

Figure 3: Overview of approximation methods

3.1 Finite element method

Different numerical procedures have been proposed to solve the shallow water equations. The method used by Xanthopoulos and Koutitas (1976) is based on a integrated finite difference scheme, Garcia and Kahawita (1989) Zang and Cundy (1989) Feng and Molz (1997), Fiedler and Ramirez (2000), methods are based on the MacCormack finite difference scheme, Galand and Hervouet (1991) use finite elements, Giammarco et al. (1996) and Hydrosphere (2004) use a control volume finite elements scheme and Zhao et al. (1994) the finite volume method.

3.1.1 Method of weighted residuals

The equations describing the processes are transformed to an equivalent integral formulation based on the method of weighted residuals (MWR). In the MWR, an approximate solution to the problem is defined. Let's assume that the unknown function within the whole domain can be represented by a trial solution $\hat{u}$

$$u \approx \hat{u}(x) = \sum_{i=1}^{m} \phi_i(x) C_i$$

where $\phi_i(x)$ are interpolation functions, C_i are unknown parameters, m is the number of grid points. If an approximate solution $\hat{u}$ is substituted into the original differential equation $L(u) = 0$ the differential equation is no longer satisfied exactly and there is a residual R due to the approximation.

$$R(t,x) = L(u) - L(\hat{u}) \neq 0$$

We now force the weighted average of the residuals for each node in the finite element mesh to equal zero

$$\int_{\Omega} \omega_i R(t,x) d\Omega = \int_{\Omega} \omega_i L(\hat{u}) d\Omega = 0$$

where ω_i are weighting functions. This provides us with an integral formulation of the governing equations. As an example we take the governing flow equation (equation 1) as an example

$$\int_{\Omega} \omega_i \left[S_0^p \frac{\partial \hat{p}}{\partial t} + \nabla \cdot \left(-\frac{\mathbf{k}}{\mu} \cdot (\nabla \hat{p} - \rho \mathbf{g}) \right) \right] d\Omega \quad = \quad \int_{\Omega} \omega_i Q_\rho d\Omega$$

The unknown function is approximated by a trial solution. Note that in the following we use Einsteins summation convention for repeating indices.

$$\hat{p}(t, x_\alpha) = \sum_{j=1}^{m} \phi_j(x_\alpha)\, p_j(t) \equiv \phi_j(x_\alpha)\, p_j(t)$$

According to the Galerkin method we use identical weighting $\omega_i(x)$ and interpolation functions $\phi_i(x)$ leading to

$$\int_\Omega \phi_i \left[S_0^p \phi_j \frac{dp_j}{dt} - \frac{\partial}{\partial x_\alpha} \left(\frac{k_{\alpha\beta}}{\mu} (\frac{\partial \phi_j}{\partial x_\beta} p_j + \rho g \frac{\partial \phi_j}{\partial x_\beta} z_j) \right) \right] d\Omega \;\; = \;\; \int_\Omega \phi_i Q_\rho d\Omega$$

Partial integration $\phi \nabla A = \nabla(\phi A) - A \nabla \phi$ and the Gauss-Ostrogradskian integral theorem are used to reduce the order of the derivatives (see Appendix 9.2 for details)

$$\int_\Omega \left[\phi_i S_0^p \phi_j \frac{dp_j}{dt} + \frac{\partial \phi_i}{\partial x_\alpha} \left(\frac{k_{\alpha\beta}}{\mu} (\frac{\partial \phi_j}{\partial x_\beta} p_j + \rho g \frac{\partial \phi_j}{\partial x_\beta} z_j) \right) \right] d\Omega = - \int_{\partial\Omega} \phi_i q_n^F dS + \int_\Omega \phi_i Q_\rho d\Omega$$

with the outward flux vector

$$q_n^F = - \frac{k_{\alpha\beta}}{\mu} (\frac{\partial \hat{p}}{\partial x_\beta} + \rho g \frac{\partial z}{\partial x_\beta}) n_\alpha$$

We rearrange the above equation to put the unknowns terms only to the left hand side.

$$\int_\Omega \phi_i \left[S_0^p \phi_j \frac{dp_j}{dt} + \frac{\partial \phi_j}{\partial x_\alpha} \frac{k_{\alpha\beta}}{\mu} \frac{\partial \phi_j}{\partial x_\beta} p_j \right] d\Omega = - \int_\Omega \phi_i \frac{\partial \phi_j}{\partial x_\alpha} \frac{k_{\alpha\beta}}{\mu} \rho g \frac{\partial \phi_j}{\partial x_\beta} z_j d\Omega - \int_{\partial\Omega} \phi_i q_n^F dS + \int_\Omega \phi_i Q_\rho d\Omega$$

The above equation forms a global system of equations where the number of equations corresponds to the number of grid points.

$$\boxed{C_{ij}^F \frac{dp_j}{dt} + K_{ij}^F p_j = r_i^F} \qquad i,j = 1,..,np \tag{42}$$

with

$$\begin{aligned} C_{ij}^F &= \int_\Omega \phi_i S_0^p \phi_j \, d\Omega \\ K_{ij}^F &= \int_\Omega \frac{\partial \phi_i}{\partial x_\alpha} \frac{k_{\alpha\beta}}{\mu} \frac{\partial \phi_j}{\partial x_\beta} \, d\Omega \\ r_i^F &= -\rho g K_{ij}^F z_i - \int_{\partial\Omega} \phi_i q_n^F dS + \int_\Omega \phi_i Q_\rho d\Omega \end{aligned}$$

where C_{ij}^F is the fluid capacitance matrix, K_{ij}^F is the fluid advection matrix and r_i^F is the right hand side (RHS) vector for fluid flow. Likewise, starting from the

differential form of the governing equation for mass transport written in terms of mass fractions ω the method of weighted residuals leads to a system of algebraic equations given below

$$\boxed{C_{ij}^T \frac{d\rho\omega_j}{dt} + (B_{ij}^T + D_{ij}^T)\rho\omega_j = r_i^T} \tag{43}$$

with

$$\begin{aligned} C_{ij}^T &= \int_\Omega \phi_i n \phi_j \, d\Omega \\ B_{ij}^T &= \int_\Omega \phi_i \frac{\partial(q_\alpha \phi_j)}{\partial x_\alpha} \, d\Omega \\ D_{ij}^T &= \int_\Omega \frac{\partial \phi_i}{\partial x_\alpha}(nD_{\alpha\beta})\frac{\partial \phi_j}{\partial x_\beta} \, d\Omega \\ r_i^T &= \int_{\partial\Omega} \phi_i q_n^T dS + \int_\Omega \phi_i (nRd\frac{A}{V}C_s) d\Omega \end{aligned}$$

where C_{ij}^T is the tracer capacitance matrix, B_{ij}^T is the tracer advection matrix, D_{ij}^T is the tracer diffusion matrix, r_i^T is RHS vector for tracer transport and q_n^T is the tracer flux vector

$$q_n^T = nD_{\alpha\beta}\frac{\partial \rho\omega_j}{\partial x_\beta} n_\alpha$$

Starting with the governing equation for overland flow the MWR yields

$$\boxed{C_{ij}^O \frac{dp_j}{dt} + K_{ij}^O p_j = r_i^O} \qquad i,j = 1,..,np \tag{44}$$

with

$$\begin{aligned} C_{ij}^O &= \int_\Omega \phi_i \phi_j \, d\Omega \\ K_{ij}^O &= \int_\Omega \frac{\partial \phi_i}{\partial x_\alpha} \frac{H^{5/3}}{n^2} \frac{1}{Ss^{1/4}} \frac{\partial \phi_j}{\partial x_\beta} \, d\Omega \\ r_i^O &= -\int_{\partial\Omega} \phi_i q_n^O dS + \int_\Omega \phi_i Q_\rho d\Omega \end{aligned}$$

where C_{ij}^O is the overland flow capacitance matrix, K_{ij}^O is the overland flow advection matrix and r_i^O is the right hand side (RHS) vector for overland flow.

3.1.2 Domain decomposition

Decomposition of the computation domain into finite elements means that the global matrices can be composed by their element contributions. The interpolation functions ϕ now correspond to individual elements and shape functions N are used for interpolation at the element level. Now the element matrices for fluid flow can be written down

$$C_{ij}^{eF} = \int_{\Omega^e} N_i S_0^p N_j \, d\Omega^e \tag{45}$$

$$K_{ij}^{eF} = \int_{\Omega^e} \frac{\partial N_i}{\partial x_\alpha} \frac{k_{\alpha\beta}}{\mu} \frac{\partial N_j}{\partial x_\beta} \, d\Omega^e \tag{46}$$

$$r_i^{eF} = -\rho g K_{ij}^{eF} z_i - \int_{\partial\Omega^e} N_i q_n^F dS^e + \int_{\Omega^e} N_i Q_\rho d\Omega^e \tag{47}$$

The element matrices for tracer transport are

$$C_{ij}^{eT} = \int_{\Omega^e} \phi_i n \phi_j \, d\Omega^e \tag{48}$$

$$B_{ij}^{eT} = \int_{\Omega^e} \phi_i \frac{\partial (q_\alpha \phi_j)}{\partial x_\alpha} \, d\Omega^e \tag{49}$$

$$D_{ij}^{eT} = \int_{\Omega^e} \frac{\partial \phi_i}{\partial x_\alpha} (n D_{\alpha\beta}) \frac{\partial \phi_j}{\partial x_\beta} \, d\Omega^e \tag{50}$$

$$r_i^{eT} = \int_{\partial\Omega^e} \phi_i q_n^T dS^e + \int_{\Omega} \phi_i (nRd \frac{A}{V} C_s) d\Omega^e \tag{51}$$

The element matrices for overland flow are accordingly

$$C_{ij}^{eO} = \int_{\Omega^e} N_i N_j \, d\Omega^e \tag{52}$$

$$K_{ij}^{eO} = \int_{\Omega^e} \frac{\partial N_i}{\partial x_\alpha} \frac{H^{5/3}}{n^2} \frac{1}{S s^{1/4}} \frac{\partial N_j}{\partial x_\beta} \, d\Omega^e \tag{53}$$

$$r_i^{eO} = -\int_{\partial\Omega^e} N_i q_n^O dS^e + \int_{\Omega^e} N_i Q_\rho d\Omega^e \tag{54}$$

3.1.3 Evaluation of element matrices

The standard procedure for integration of element matric expressions is the Gauss quadrature. The procedure is explained in general and applied to evaluate the overland flow advection matrix in this section. The same method is applied to the evaluation of element matrices of the prism elements described in section 3.3.2.

Gauss quadrature

In this method a numerical approximation to the integral over an interval is obtained by computing the weighted sum of values of the function for specific points on the interval. The equation for Gauss quadrature is

$$\int_{-1}^{1} f(r)dr = \sum_{i=1}^{N_r} W_i(r_i) f(r_i)$$

where $W_i(r_i)$ is the weight assigned to the value of the function f at the Gauss point $r = r_i$ and N_r is the number of Gauss points on the interval. The derivatives of the interpolation functions are given in terms of global coordinates (x,y,z), but we can use a coordinate transformation of the form

$$x = f(r) \quad , \quad y = f(s) \quad , \quad z = f(t)$$

to rewrite the interpolation functions and their derivatives in terms of the local coordinates(r,s,t). We need the Jacobian matrix of the coordinate transformation $[J_{3D}]$ and its determinant $det[J_{3D}]$.

For the overland flow advection matrix K_{ij}^O the numerical approximation can now be written as

$$\begin{aligned} K_{ij}^O &= \int_\Omega \frac{\partial N_i}{\partial x_\alpha} \frac{H^{5/3}}{n^2} \frac{1}{Ss^{1/4}} \frac{\partial N_j}{\partial x_\beta} \, d\Omega \\ &= \int_{-1}^{1}\int_{-1}^{1} \frac{\partial N_i}{\partial x_\alpha} [J_{2D}^{-1}]^T \frac{H^{5/3}}{n^2} \frac{1}{Ss^{1/4}} \frac{\partial N_j}{\partial x_\beta} [J_{2D}^{-1}] \, det[J_{2D}] \, drds \\ &= \sum_{i=1}^{N_r}\sum_{j=1}^{N_s} W_i(r_i) W_j(s_j) \frac{\partial N_i}{\partial x_\alpha} [J_{2D}^{-1}]^T \frac{H(r_i,s_j)^{5/3}}{n^2} \frac{1}{Ss(r_i,s_j)^{1/4}} \frac{\partial N_j}{\partial x_\beta} [J_{2D}^{-1}] \, det[J_{2D}] \end{aligned}$$

Friction slope $Ss(r_i, s_j)$ and water depth $H(r_i, s_j)$ are approximated for each Gauss point by the expressions

$$Ss(r_i,s_j) = \frac{1}{n^4} \left(\sum_{i=1}^{N_e} \frac{\partial N_i}{\partial x} \quad h_i \right)^2 + \frac{1}{n^4} \left(\sum_{i=1}^{N_e} \frac{\partial N_j}{\partial y} \quad h_i \right)^2$$

and

$$H(r_i,s_j) = N_i H_i$$

where N_e is the number of element nodes. During the testing procedure this approximation of H produced non physical oscillations in the solution so that an upstream weighting was introduced to evaluate H. This lead to a smooth solution as described in section 5.4.

Handling nonlinearity

The graph in Fig. 4 displays values of the conductivity equivalent k_{eq} for different water depth and different Manning coefficients. An increase of the water depth of one order of magnitude leads to an increase of the conductivity equivalent of almost two orders of magnitude. Hence, we have a highly nonlinear process that calls for an automatic time stepping scheme (Jaber and Mohtar (2003)) and a Newton-Raphson iteration in order to reduce computation time. However, as a starting point we use a simple Picard iteration using fixed time steps. Both method are described in section 3.5

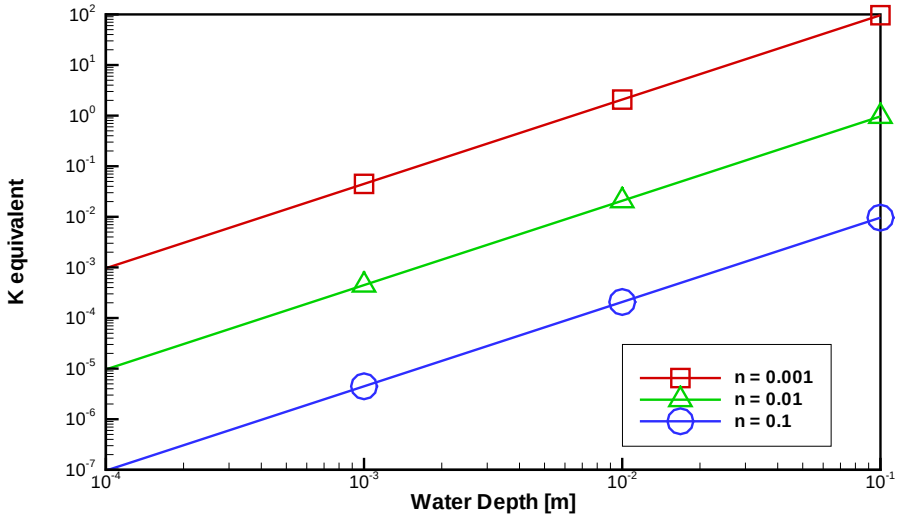

Figure 4: Values for the conductivity equivalent k_{eq} for different water depth and different Manning coefficients.

There are two different options to deal with the critical depth boundary condition. In the first option the depth is updated in every nonlinear iteration. In the second scheme, implemented to stabilize the system, the boundary condition is updated, only after a convergence criterium has been met. In both schemes the head of the previous nonlinear iteration is used to calculate the flux following the critical depth equation 30 , which is than assigned as sink terms.

3.2 Finite element library

The finite element library consists of linear elements, triangles, quadrilaterals, tetrahedrons, hexahedra, and triangular prisms. All elements can be used in combination within one mesh as shown in Fig. 5. In this way linear elements

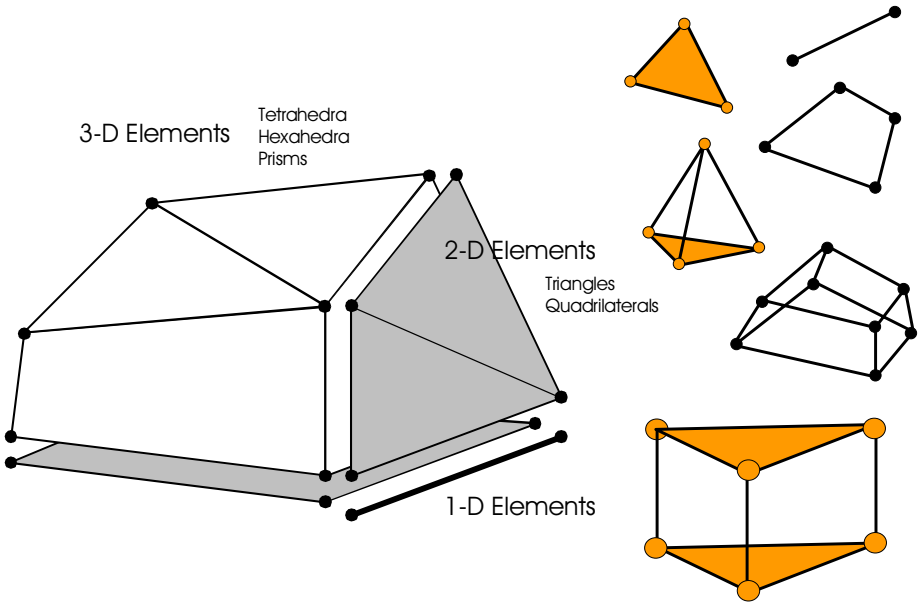

Figure 5: Finite element library and combination of different elements

can be used to model channel flow or the unsaturated zone, triangles for overland flow, triangular prisms for saturated groundwater flow and quadrilaterals for fracture flow.

3.3 Triangular prismatic elements

When selecting an appropriate element type out of the finite element family (see Fig. 5) the geometry of the problem domain, the required accuracy and the complexity of the element matrix computation must be taken into consideration.

Modelling regional three-dimensional groundwater problems involves the representation of geological systems, i.e. very often layered systems, with varying thicknesses of different layers with irregular horizontal boundaries. Those systems can best be modelled using triangular prismatic (or pentahedral) elements: Layers of these elements represent geological formations so that system boundaries can be easily displayed and checked in vertical cross sections. Irregular horizontal boundaries can easily be formed using triangular shapes without the need of refining the grid in order to approximate the boundary as would be the case with hexahedral elements. Rather than using a large number of hexahedral elements it is more computationally efficient to use triangular prismatic elements. The required accuracy of the calculation can be met by using the appropriate horizontal mesh density. If vertical processes need to be modelled accurately a

prism layer can be further subdivided into more layers, i.e. the vertical resolution can be improved easily.

If we assume that bottom and top of the triangular prismatic elements are horizontal their element matric expressions (equations 45 to 51) can be integrated analytically. Hence, the numerical integration is not necessary so that the computational effort is significantly reduced in comparison to hexahedral elements. If, for example, three Gauss points for the horizontal coordinate direction and two for the vertical component are used for the numerical approximation of the element matrix of a triangular prismatic element the expressions have to be evaluated 6 times. Clearly the reduction of computational effort in the formulation of element characteristics is especially an advantage if it comes to large scale groundwater models or if nonlinearities as unconfined flow or density dependent flow have to be considered. Both nonlinearities may play a role in the study described by Beinhorn et al. (2004), see list of publications, section 9.8.

As a first step the routines for numerical integration of element matrix expressions have been implemented thus providing a basis for checking element matrices calculated analytically at a later stage. The work done with respect to the numerical integration is documented in Beinhorn and Kolditz (2003a), see list of publications, section 9.8. In a second step the analytical integration has been implemented. The technique in principle has been used as early as 1984 by Huyakorn and Thomas (1984) there referred to as 'influence coefficient' technique. Influence coefficient matrices were presented for linear rectangular elements. At a later stage Huyakorn et al. (1986) presented coefficient matrices for linear rectangular prism elements and linear triangular prism elements for fluid flow. In Beinhorn and Kolditz (2003b) (see list of publications in the appendix, section 9.8) the matrice expressions are derived in detail for fluid flow as well as tracer transport.

As a first step the routines for numerical integration of element matrix expressions have been implemented thus providing a basis for checking element matrices calculated analytically at a later stage. The work done with respect to the numerical integration is documented in the following section. Section 3.3.3 deals with the analytical integration of the element matric expressions.

3.3.1 Element geometry

The geometry of a triangle based prismatic element in three-dimensional space is displayed in Fig. 6.

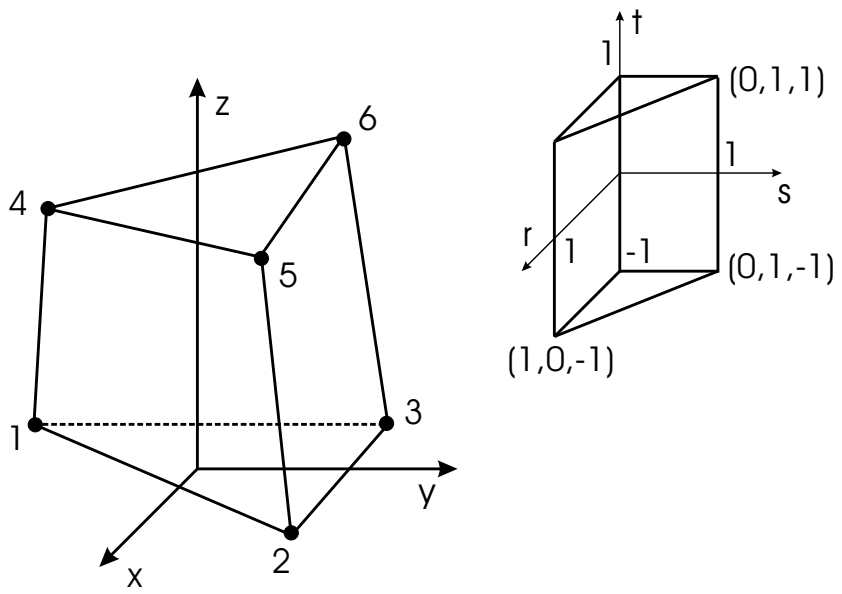

Figure 6: Triangular prismatic element, global and local coordinates, Kolditz (2002)

3.3.2 Element matrices, numerical approximation

Shape functions The shape functions for three-dimensional prisms based on triangles are given by (see Diersch (2001b))

$$
\begin{aligned}
N_1 &= \frac{1}{2}(1-r-s)(1+t) & N_4 &= \frac{1}{2}(1-r-s)(1-t) \\
N_2 &= \frac{1}{2}r(1+t) & N_5 &= \frac{1}{2}r(1-t) \\
N_3 &= \frac{1}{2}s(1+t) & N_6 &= \frac{1}{2}s(1-t)
\end{aligned}
$$

Derivatives of shape functions are

$$
\begin{aligned}
\nabla \mathbf{N} &= \begin{Bmatrix}
\frac{\partial N_1}{\partial r} & \frac{\partial N_2}{\partial r} & \frac{\partial N_3}{\partial r} & \frac{\partial N_4}{\partial r} & \frac{\partial N_5}{\partial r} & \frac{\partial N_6}{\partial r} \\
\frac{\partial N_1}{\partial s} & \frac{\partial N_2}{\partial s} & \frac{\partial N_3}{\partial s} & \frac{\partial N_4}{\partial s} & \frac{\partial N_5}{\partial s} & \frac{\partial N_6}{\partial s} \\
\frac{\partial N_1}{\partial t} & \frac{\partial N_2}{\partial t} & \frac{\partial N_3}{\partial t} & \frac{\partial N_4}{\partial t} & \frac{\partial N_5}{\partial t} & \frac{\partial N_6}{\partial t}
\end{Bmatrix} \\
&= \frac{1}{2}\begin{bmatrix}
-(1+t) & (1+t) & 0 & -(1-t) & (1-t) & 0 \\
-(1+t) & 0 & (1+t) & -(1-t) & 0 & (1-t) \\
(1-r-s) & r & s & -(1-r-s) & -r & s
\end{bmatrix}
\end{aligned}
$$

Gauss quadrature When the element matrices of a prismatic elements have to be evaluated we are faced with an integration with respect to a volume. The

standard procedure is to use the method of Gauss quadrature. In this method a numerical approximation to the integral over an interval is obtained by computing the weighted sum of values of the function for specific points on the interval. The equation for Gauss quadrature is

$$\int_{-1}^{1} f(r)dr = \sum_{i=1}^{N_r} W_i(r_i) f(r_i)$$

where $W_i(r_i)$ is the weight assigned to the value of the function f at the Gauss point $r = r_i$ and N_r is the number of Gauss points on the interval. In three dimensions the equation for Gauss quadrature is

$$\int_{-1}^{1}\int_{-1}^{1}\int_{-1}^{1} f(r,s,t)drdsdt = \sum_{i=1}^{N_r}\sum_{j=1}^{N_s}\sum_{k=1}^{N_t} W_i(r_i)W_j(s_j)W_k(t_k) f(r_i,s_j,t_k)$$

Locations of Gauss points and values of weights were chosen as given in Ratke et al. (1996)

	GP1	GP2	GP3	GP4	GP5	GP6	GP7	GP8
r	$1/3$	$3/5$	$1/5$	$1/5$	$1/3$	$3/5$	$1/5$	$1/5$
s	$1/3$	$1/5$	$3/5$	$1/5$	$1/3$	$1/5$	$3/5$	$1/5$
t	$\sqrt{1/3}$	$\sqrt{1/3}$	$\sqrt{1/3}$	$\sqrt{1/3}$	$-\sqrt{1/3}$	$-\sqrt{1/3}$	$-\sqrt{1/3}$	$-\sqrt{1/3}$
W_iW_j	$-9/32$	$25/96$	$25/96$	$25/96$	$-9/32$	$25/96$	$25/96$	$25/96$
W_k	1	1	1	1	1	1	1	1

Coordinate transformation The derivatives of the interpolation functions are given in terms of global coordinates (x,y,z), but we can use a coordinate transformation of the form

$$x = f(r) \quad , \quad y = f(s) \quad , \quad z = f(t)$$

to rewrite the interpolation functions and their derivatives in terms of the local coordinates(r,s,t). We need the Jacobian matrix of the coordinate transformation $[J_{3D}]$ and its determinant $det[J_{3D}]$.

Fluid capacitance matrix The capacitance matrix is a matrix of the type C-type integral: $\int \mathbf{N} f(u_i) \mathbf{N} d\Omega$. Using coordinate transformation and Gauss quadrature as outlined above one obtains

$$\begin{aligned} C_{ij} &= \int_{\Omega} N_i S_0 N_j \, d\Omega = S_0 \int_{-1}^{1}\int_{-1}^{1}\int_{-1}^{1} N_i N_j \, det[J_{3D}] \, drdsdt \\ &= S_0 \sum_{i=1}^{N_r}\sum_{j=1}^{N_s}\sum_{k=1}^{N_t} W_i(r_i)W_j(s_j)W_k(t_k) N_i N_j \, det[J_{3D}] \end{aligned}$$

Tracer capacitance matrix The tracer capacitance matrix is a matrix of the type C-type integral: $\int \mathbf{N} f(u_i) \mathbf{N} d\Omega$. Using coordinate transformation and Gauss quadrature as outlined above one obtains

$$\begin{aligned} C_{ij} &= \int_\Omega N_i N_j \, d\Omega = \int_{-1}^{1}\int_{-1}^{1}\int_{-1}^{1} N_i N_j \, det[J_{3D}] \, dr ds dt \\ &= \sum_{i=1}^{N_r}\sum_{j=1}^{N_s}\sum_{k=1}^{N_t} W_i(r_i) W_j(s_j) W_k(t_k) N_i N_j \, det[J_{3D}] \end{aligned}$$

Fluid conductance matrix The conductivity matrix is a matrix of the K-type integral: $\int \nabla \mathbf{N} f(u_i) \nabla \mathbf{N} d\Omega$. Using coordinate transformation and Gauss quadrature as outlined above one obtains

$$\begin{aligned} K_{ij} &= \int_\Omega \frac{\partial N_i}{\partial x_\alpha} \left(\frac{k_{\mathsf{rel}} k_{\alpha\beta}}{\mu} \right) \frac{\partial N_j}{\partial x_\beta} \, d\Omega \\ &= \int_{-1}^{1}\int_{-1}^{1}\int_{-1}^{1} \frac{\partial N_i}{\partial x_\alpha} [J_{3D}^{-1}]^T \left(\frac{k_{\mathsf{rel}} k_{\alpha\beta}}{\mu} \right) \frac{\partial N_j}{\partial x_\beta} [J_{3D}^{-1}] \, det[J_{3D}] \, dr ds dt \\ &= \sum_{i=1}^{N_r}\sum_{j=1}^{N_s}\sum_{k=1}^{N_t} W_i(r_i) W_j(s_j) W_k(t_k) \frac{\partial N_i}{\partial x_\alpha} [J_{3D}^{-1}]^T \left(\frac{k_{\mathsf{rel}} k_{\alpha\beta}}{\mu} \right) \frac{\partial N_j}{\partial x_\beta} [J_{3D}^{-1}] \, det[J_{3D}] \end{aligned}$$

Tracer diffusion/dispersion matrix The tracer diffusion/dispersion matrix is a matrix of the K-type integral: $\int \nabla \mathbf{N} f(u_i) \nabla \mathbf{N} d\Omega$. Using coordinate transformation and Gauss quadrature as outlined above one obtains

$$\begin{aligned} D_{ij} &= \int_\Omega \frac{\partial N_i}{\partial x_\alpha} \left(D_{\alpha\beta} \right) \frac{\partial N_j}{\partial x_\beta} \, d\Omega \\ &= \int_{-1}^{1}\int_{-1}^{1}\int_{-1}^{1} \frac{\partial N_i}{\partial x_\alpha} [J_{3D}^{-1}]^T \left(D_{\alpha\beta} \right) \frac{\partial N_j}{\partial x_\beta} [J_{3D}^{-1}] \, det[J_{3D}] \, dr ds dt \\ &= \sum_{i=1}^{N_r}\sum_{j=1}^{N_s}\sum_{k=1}^{N_t} W_i(r_i) W_j(s_j) W_k(t_k) \frac{\partial N_i}{\partial x_\alpha} [J_{3D}^{-1}]^T \left(D_{\alpha\beta} \right) \frac{\partial N_j}{\partial x_\beta} [J_{3D}^{-1}] \, det[J_{3D}] \end{aligned}$$

Tracer advection matrix The advection matrix is a matrix of the B-type integral: $\int \mathbf{N} f(u_i) \nabla \mathbf{N} d\Omega$ written as

$$\begin{aligned} B_{ij}^{eT} &= \int_\Omega N_i v_\alpha \frac{\partial N_j}{\partial x_\alpha} \, d\Omega = \int_{-1}^{1}\int_{-1}^{1}\int_{-1}^{1} N_i v_\alpha \frac{\partial N_j}{\partial x_\alpha} [J_{3D}^{-1}] \, det[J_{3D}] \, dr ds dt \\ &= \sum_{i=1}^{N_r}\sum_{j=1}^{N_s}\sum_{k=1}^{N_t} W_i(r_i) W_j(s_j) W_k(t_k) N_i v_\alpha \frac{\partial N_j}{\partial x_\alpha} [J_{3D}^{-1}] \, det[J_{3D}] \end{aligned}$$

Gravity forces Gravity forces are written as a matrix of g-type integral: $\int \nabla \mathbf{N} f(u_i) d\Omega$ which can be written as

$$\mathbf{g} \;=\; K \times (z)$$

3.3.3 Element matrices, analytical approximation

Shape functions The shape functions for three-dimensional prisms based on triangles can be derived by taking the product of the shape functions for triangles N^{Δ} with that of line elements N^t as outlined in Kolditz (2002)

$$\begin{aligned} N_1 = N_1^{\Delta} N_1^t \quad , \quad N_2 = N_2^{\Delta} N_1^t \quad , \quad N_3 = N_3^{\Delta} N_1^t \\ N_4 = N_1^{\Delta} N_2^t \quad , \quad N_5 = N_2^{\Delta} N_2^t \quad , \quad N_6 = N_3^{\Delta} N_2^t \end{aligned}$$

where the shape functions for linear elements are as follows in local coordinates

$$N_1^t(t) = \frac{1-t}{2} \quad , \quad N_2^t(t) = \frac{1+t}{2}$$

Triangles are isoparametric elements so that their shape functions can be given in physical coordinates

$$\begin{aligned} N_1^{\Delta}(x,y) &= \frac{1}{2A}\left[(x_2 y_3 - x_3 y_2) + (y_2 - y_3)x + (x_3 - x_2)y\right] \\ N_2^{\Delta}(x,y) &= \frac{1}{2A}\left[(x_3 y_1 - x_1 y_3) + (y_3 - y_1)x + (x_1 - x_3)y\right] \\ N_3^{\Delta}(x,y) &= \frac{1}{2A}\left[(x_1 y_2 - x_2 y_1) + (y_1 - y_2)x + (x_2 - x_1)y\right] \end{aligned}$$

Integration When the element matrices of a prismatic elements have to be evaluated we are faced with an integration with respect to a volume. The calculations are performed following the procedure given below

The volume integral of the product of the two functions f_1 and f_2 is separated into an area integral and a line integral

$$\int_{\Omega} f_1(N_1^{\Delta}, N_2^{\Delta}, N_3^{\Delta}) f_2(N_z) dV = \int_{\Omega} f_1 f_2 dA\, dz = \int_{\Delta} f_1 dA \times \int_z f_2 dz \quad (55)$$

The right hand side integral can be solved trivially after a coordinate transformation according to

$$\int_z f_2 dz = \int_{-1}^{1} f_2\, det[J_{3D}^z] \qquad and \qquad \int_z \frac{\partial f_2}{\partial z} = \int_{-1}^{1} [J_{3D}^z]^{-1} f_2\, det[J_{3D}^z] \quad (56)$$

has been performed. The Jacobian $[J^z_{3D}]$ for the transition from global to local coordinates or vice versa is defined as

$$\frac{\partial N^t}{\partial t} = \frac{\partial N^t}{\partial z}\frac{\partial z}{\partial t} = \frac{\partial N^t}{\partial z}[J^z_{3D}] \qquad or \qquad \frac{\partial N^t}{\partial z} = \frac{\partial N^t}{\partial t}\frac{\partial t}{\partial z} = \frac{\partial N^t}{\partial t}[J^z_{3D}]^{-1}$$

where dz represents the thickness of the element. The element thickness is approximated using the edge length $|z_i|$ in combination with a weighting factor given by local area coordinates so that $[J^z_{3D}]^{-1}$ can be written as

$$[J^z_{3D}]^{-1} = \frac{dt}{dz} = \frac{2}{\Delta z} = \frac{2A}{A_1|z_{14}| + A_2|z_{25}| + A_3|z_{36}|} = \frac{2}{N_1|z_{14}| + N_2|z_{25}| + N_3|z_{36}|}$$

Written in matrix form:

$$\left\{ \begin{array}{c} N_1 \\ N_2 \\ N_3 \end{array} \right\} = \frac{1}{2A} \left[\begin{array}{ccc} x_2y_3 - x_3y_2 & y_2 - y_3 & x_3 - x_2 \\ x_3y_1 - x_1y_3 & y_3 - y_1 & x_1 - x_3 \\ x_1y_2 - x_2y_1 & y_1 - y_2 & x_2 - x_1 \end{array} \right] \left\{ \begin{array}{c} 1 \\ x \\ y \end{array} \right\} \tag{57}$$

Fig. 7 shows sketches of the plots of these functions as illustration. The derivatives of the shape functions are

$$\frac{\partial \mathbf{N}}{\partial x} = \left\{ \begin{array}{l} \frac{\partial N_1}{\partial x} = \frac{y_2 - y_3}{2A} \\ \frac{\partial N_2}{\partial x} = \frac{y_3 - y_1}{2A} \\ \frac{\partial N_3}{\partial x} = \frac{y_1 - y_2}{2A} \end{array} \right\} \qquad \frac{\partial \mathbf{N}}{\partial y} = \left\{ \begin{array}{l} \frac{\partial N_1}{\partial y} = \frac{x_3 - x_2}{2A} \\ \frac{\partial N_2}{\partial y} = \frac{x_1 - x_3}{2A} \\ \frac{\partial N_3}{\partial y} = \frac{x_2 - x_1}{2A} \end{array} \right\} \tag{58}$$

The determinant of the Jacobian $\det[J^z_{3D}]$ is given by

$$det[J^z_{3D}] = \frac{N_1|z_{14}| + N_2|z_{25}| + N_3|z_{36}|}{2} = [J^z_{3D}]$$

The integration with respect to the triangle area of the left hand side integral of equation 55 can be done using a formula given in Zienkiewicz and Taylor (2000)

$$\int_\Delta N_1^a N_2^b N_3^c dA = \frac{a!b!c!}{(a+b+c+2)!} 2A \tag{59}$$

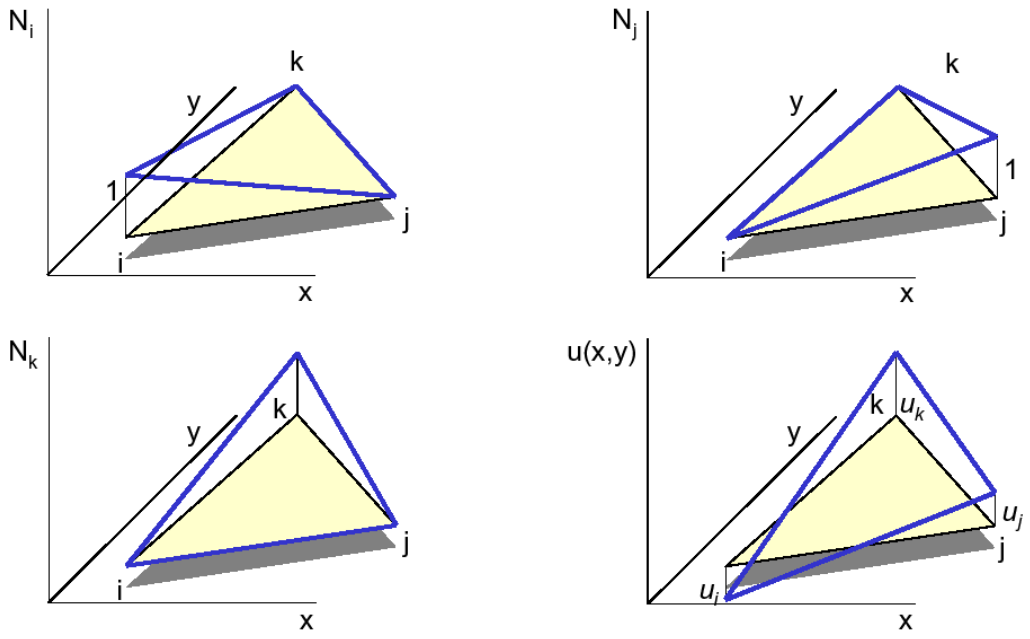

Figure 7: Graphical representation of triangle shape functions

Fluid capacitance matrix The capacitance matrix is a matrix of the type C-type integral: $\int \mathbf{N} f(u_i) \mathbf{N} d\Omega$. Using equations 55 and 56 one obtains

$$\begin{aligned} C_{ij} &= \int_\Omega N_i S_0 N_j \, d\Omega \\ &= S_0 \int_V N_i^\Delta N_j^\Delta N_i^t N_j^t \, dV = S_0 \; det[J_{3D}^z] \underbrace{\int_\Delta N_i^\Delta N_j^\Delta dA}_{\mathbf{C}^\Delta} \times \underbrace{\int_{-1}^{1} N_i^t N_j^t dt}_{\mathbf{C}^t} \end{aligned}$$

with $\mathbf{C}^t$ the linear component and $\mathbf{C}^\Delta$ the triangle component of the capacitance matrix. The linear component can be integrated trivially

$$\mathbf{C}^t = \frac{1}{3} \begin{bmatrix} 2 & 2 & 2 & 1 & 1 & 1 \\ 2 & 2 & 2 & 1 & 1 & 1 \\ 2 & 2 & 2 & 1 & 1 & 1 \\ 1 & 1 & 1 & 2 & 2 & 2 \\ 1 & 1 & 1 & 2 & 2 & 2 \\ 1 & 1 & 1 & 2 & 2 & 2 \end{bmatrix} \tag{60}$$

The triangle component is given by an 6x6 matrix expressed as

$$\mathbf{C}^\Delta = \int_\Delta \begin{bmatrix} \mathbf{c}^\Delta & \mathbf{c}^\Delta \\ \mathbf{c}^\Delta & \mathbf{c}^\Delta \end{bmatrix} dA \tag{61}$$

where the 3x3 components c^{Δ} are given by

$$c_{ij}^{\Delta} = \int_{\Delta} N_i^{\Delta} N_j^{\Delta}$$

Using equation 59 the integration over the triangular region yields

$$\mathbf{c}^{\Delta} = \begin{bmatrix} 2 & 1 & 1 \\ 1 & 2 & 1 \\ 1 & 1 & 2 \end{bmatrix} \frac{1}{12} A$$

Hence, the element capacitance matrix for a prismatic element can be written as

$$\mathbf{C} = S_0 \quad det[J_{3D}^z] \quad \mathbf{C}^{\Delta} \times \mathbf{C}^t$$

Tracer capacitance matrix The tracer capacitance matrix is a matrix of the type C-type integral: $\int \mathbf{N} f(u_i) \mathbf{N} d\Omega$. Using equations 55 and 56 one obtains

$$\begin{aligned} C_{ij} &= \int_{\Omega} N_i \, N_j \, d\Omega \\ &= \int_V N_i^{\Delta} N_j^{\Delta} N_i^t N_j^t \, dV = det[J_{3D}^z] \underbrace{\int_{\Delta} N_i^{\Delta} N_j^{\Delta} dA}_{\mathbf{C}^{\Delta}} \times \underbrace{\int_{-1}^{1} N_i^t N_j^t dt}_{\mathbf{C}^t} \end{aligned}$$

with $\mathbf{C}^t$ the linear component and $\mathbf{C}^{\Delta}$ the triangle component of the capacitance matrix as derived above (equations 60 and 61).

Fluid conductance matrix The conductivity matrix is a matrix of the K-type integral: $\int \nabla \mathbf{N} f(u_i) \nabla \mathbf{N} d\Omega$ written as

$$K_{ij} = \int_{\Omega} \frac{\partial N_i}{\partial x_{\alpha}} \left(\frac{k_{\mathsf{rel}} k_{\alpha\beta}}{\mu} \right) \frac{\partial N_j}{\partial x_{\beta}} \, d\Omega$$

With only the main diagonal of the permeability tensor $\neq 0$ the expression reduces to

$$\begin{aligned} K_{ij} = \left(\frac{k_{\mathsf{rel}} k_{xx}}{\mu} \right) \underbrace{\int_{\Omega} \frac{\partial N_i}{\partial x} \frac{\partial N_j}{\partial x} \, d\Omega}_{K_{ij}^{xx}} + \left(\frac{k_{\mathsf{rel}} k_{yy}}{\mu} \right) \underbrace{\int_{\Omega} \frac{\partial N_i}{\partial y} \frac{\partial N_j}{\partial y} \, d\Omega}_{K_{ij}^{yy}} \\ + \left(\frac{k_{\mathsf{rel}} k_{zz}}{\mu} \right) \underbrace{\int_{\Omega} \frac{\partial N_i}{\partial z} \frac{\partial N_j}{\partial z} \, d\Omega}_{K_{ij}^{zz}} \end{aligned}$$

The components K_{ij}^{xx}, K_{ij}^{yy} and K_{ij}^{zz} are again evaluated using equations 55 and 56. One obtains

$$K_{ij}^{xx} = \int_\Omega \frac{\partial N_i}{\partial x}\frac{\partial N_j}{\partial x}\,d\Omega = det[J_{3D}^z]\,A\,\underbrace{\frac{\partial N_i^\Delta}{\partial x}\frac{\partial N_j^\Delta}{\partial x}}_{\mathbf{K}^{\Delta x}} \times \underbrace{\int_{-1}^{1} N_i^t N_j^t\,dt}_{\mathbf{C}^t} \quad (62)$$

$$K_{ij}^{yy} = \int_\Omega \frac{\partial N_i}{\partial y}\frac{\partial N_j}{\partial y}\,d\Omega = det[J_{3D}^z]\,A\,\underbrace{\frac{\partial N_i^\Delta}{\partial y}\frac{\partial N_j^\Delta}{\partial y}}_{\mathbf{K}^{\Delta y}} \times \underbrace{\int_{-1}^{1} N_i^t N_j^t\,dt}_{\mathbf{C}^t} \quad (63)$$

$$K_{ij}^{zz} = \int_\Omega \frac{\partial N_i}{\partial z}\frac{\partial N_j}{\partial z}\,d\Omega = [J_{3D}^z]^{-1}\underbrace{\int_\Delta N_i^\Delta N_j^\Delta\,dA}_{\mathbf{C}^\Delta} \times \int_{-1}^{1}\frac{\partial N_i^t}{\partial t}\frac{\partial N_j^t}{\partial t}\,dt \quad (64)$$

with $\mathbf{C}^t$ the linear component of the capacitance matrix and $\mathbf{C}^\Delta$ the triangle component of the capacitance matrix as already given in equations 60 and 61. The left hand side integral of equations 62 and 63 can be written as

$$\mathbf{K}^{\Delta x} = \begin{bmatrix} \mathbf{k}^{\Delta x} & \mathbf{k}^{\Delta x} \\ \mathbf{k}^{\Delta x} & \mathbf{k}^{\Delta x} \end{bmatrix} \quad , \quad \mathbf{K}^{\Delta y} = \begin{bmatrix} \mathbf{k}^{\Delta y} & \mathbf{k}^{\Delta y} \\ \mathbf{k}^{\Delta y} & \mathbf{k}^{\Delta y} \end{bmatrix}$$

Substituting the derivatives of the shape functions the expressions $\mathbf{k}^{\Delta x}$ and $\mathbf{k}^{\Delta y}$ yield the 3x3 matrices

$$\mathbf{k}^{\Delta x} = \frac{1}{4A^2}\begin{bmatrix} (y_2-y_3)(y_2-y_3) & (y_2-y_3)(y_3-y_1) & (y_2-y_3)(y_1-y_2) \\ (y_3-y_1)(y_2-y_3) & (y_3-y_1)(y_3-y_1) & (y_3-y_1)(y_1-y_2) \\ (y_1-y_2)(y_2-y_3) & (y_1-y_2)(y_3-y_1) & (y_1-y_2)(y_1-y_2) \end{bmatrix}$$

$$\mathbf{k}^{\Delta y} = \frac{1}{4A^2}\begin{bmatrix} (x_3-x_2)(x_3-x_2) & (x_3-x_2)(x_1-x_3) & (x_3-x_2)(x_2-x_1) \\ (x_1-x_3)(x_3-x_2) & (x_1-x_3)(x_1-x_3) & (x_1-x_3)(x_2-x_1) \\ (x_2-x_1)(x_3-x_2) & (x_2-x_1)(x_1-x_3) & (x_2-x_1)(x_2-x_1) \end{bmatrix}$$

Now only the right hand side integral of equation 64 needs to be written down and there is a complete expression for the conductance matrix.

$$\int_{-1}^{1}\frac{\partial N_i^t}{\partial t}\frac{\partial N_j^t}{\partial t}\,dt = \frac{1}{2}\begin{bmatrix} 1 & 1 & 1 & -1 & -1 & -1 \\ 1 & 1 & 1 & -1 & -1 & -1 \\ 1 & 1 & 1 & -1 & -1 & -1 \\ -1 & -1 & -1 & 1 & 1 & 1 \\ -1 & -1 & -1 & 1 & 1 & 1 \\ -1 & -1 & -1 & 1 & 1 & 1 \end{bmatrix}$$

Tracer diffusion/dispersion matrix The tracer diffusion/dispersion matrix is a matrix of the K-type integral: $\int \nabla \mathbf{N} f(u_i) \nabla \mathbf{N} d\Omega$ written as

$$D_{ij} = \int_\Omega \frac{\partial N_i}{\partial x_\alpha} (D_{\alpha\beta}) \frac{\partial N_j}{\partial x_\beta} d\Omega$$

$$\begin{aligned} D_{ij} = {} & D_{xx} \underbrace{\int_\Omega \frac{\partial N_i}{\partial x}\frac{\partial N_j}{\partial x} d\Omega}_{D_{ij}^{xx}} + D_{xy} \underbrace{\int_\Omega \frac{\partial N_i}{\partial x}\frac{\partial N_j}{\partial y} d\Omega}_{D_{ij}^{xy}} + D_{xz} \underbrace{\int_\Omega \frac{\partial N_i}{\partial x}\frac{\partial N_j}{\partial z} d\Omega}_{D_{ij}^{xz}} \\ & + D_{yx} \underbrace{\int_\Omega \frac{\partial N_i}{\partial y}\frac{\partial N_j}{\partial x} d\Omega}_{D_{ij}^{yx}} + D_{yy} \underbrace{\int_\Omega \frac{\partial N_i}{\partial y}\frac{\partial N_j}{\partial y} d\Omega}_{D_{ij}^{yy}} + D_{yz} \underbrace{\int_\Omega \frac{\partial N_i}{\partial y}\frac{\partial N_j}{\partial z} d\Omega}_{D_{ij}^{yz}} \\ & + D_{zx} \underbrace{\int_\Omega \frac{\partial N_i}{\partial z}\frac{\partial N_j}{\partial x} d\Omega}_{D_{ij}^{zx}} + D_{zy} \underbrace{\int_\Omega \frac{\partial N_i}{\partial z}\frac{\partial N_j}{\partial y} d\Omega}_{D_{ij}^{zy}} + D_{zz} \underbrace{\int_\Omega \frac{\partial N_i}{\partial z}\frac{\partial N_j}{\partial z} d\Omega}_{D_{ij}^{zz}} \end{aligned}$$

The 9 components are again evaluated using equations 55 and 56. One obtains

$$\begin{aligned} D_{ij}^{xx} &= det[J_{3D}^z]\, A\, \underbrace{\frac{\partial N_i^\Delta}{\partial x}\frac{\partial N_j^\Delta}{\partial x}}_{\mathbf{K}^{\Delta x}} \times \underbrace{\int_{-1}^{1} N_i^t N_j^t\, dt}_{\mathbf{C}^t} = K_{ij}^{xx} \\ D_{ij}^{xy} &= det[J_{3D}^z]\, A\, \underbrace{\frac{\partial N_i^\Delta}{\partial x}\frac{\partial N_j^\Delta}{\partial y}}_{\mathbf{D}^{\Delta xy}} \times \underbrace{\int_{-1}^{1} N_i^t N_j^t\, dt}_{\mathbf{C}^t} \\ D_{ij}^{xz} &= \underbrace{\int_\Delta \frac{\partial N_i^\Delta}{\partial x} N_j^\Delta dA}_{\mathbf{D}^{\Delta xx}} \times \int_{-1}^{1} N_i^t \frac{\partial N_j^t}{\partial t}\, dt \\ D_{ij}^{yx} &= det[J_{3D}^z]\, A\, \underbrace{\frac{\partial N_i^\Delta}{\partial y}\frac{\partial N_j^\Delta}{\partial x}}_{\mathbf{D}^{\Delta yx}} \times \underbrace{\int_{-1}^{1} N_i^t N_j^t\, dt}_{\mathbf{C}^t} \\ D_{ij}^{yy} &= det[J_{3D}^z]\, A\, \underbrace{\frac{\partial N_i^\Delta}{\partial y}\frac{\partial N_j^\Delta}{\partial y}}_{\mathbf{K}^{\Delta y}} \times \underbrace{\int_{-1}^{1} N_i^t N_j^t\, dt}_{\mathbf{C}^t} = K_{ij}^{yy} \\ D_{ij}^{yz} &= \underbrace{\int_\Delta \frac{\partial N_i^\Delta}{\partial y} N_j^\Delta dA}_{\mathbf{D}^{\Delta yz}} \times \int_{-1}^{1} N_i^t \frac{\partial N_j^t}{\partial t}\, dt \\ D_{ij}^{zx} &= \underbrace{\int_\Delta N_i^\Delta \frac{\partial N_j^\Delta}{\partial x} dA}_{\mathbf{D}^{\Delta zx}} \times \int_{-1}^{1} \frac{\partial N_i^t}{\partial t} N_j^t\, dt \end{aligned}$$

$$D_{ij}^{zy} = \underbrace{\int_{\Delta} N_i^{\Delta} \frac{\partial N_j^{\Delta}}{\partial y} dA}_{\mathbf{D}^{\Delta zy}} \times \int_{-1}^{1} \frac{\partial N_i^t}{\partial t} N_j^t \, dt$$

$$D_{ij}^{zz} = [J_{3D}^z]^{-1} \underbrace{\int_{\Delta} N_i^{\Delta} N_j^{\Delta} dA}_{\mathbf{C}^{\Delta}} \times \int_{-1}^{1} \frac{\partial N_i^t}{\partial t} \frac{\partial N_j^t}{\partial t} \, dt = K_{ij}^{zz}$$

Now only the remaining integrals $\int_{-1}^{1} N_i^t \frac{\partial N_j^t}{\partial t} \, dt$ and $\int_{-1}^{1} \frac{\partial N_i^t}{\partial t} N_j^t \, dt$ have to be written down and there is a complete expression for the diffusion/ dispersion matrix.

$$\int_{-1}^{1} N_i^t \frac{\partial N_j^t}{\partial t} \, dt = \frac{1}{2} \begin{bmatrix} 1 & 1 & 1 & -1 & -1 & -1 \\ 1 & 1 & 1 & -1 & -1 & -1 \\ 1 & 1 & 1 & -1 & -1 & -1 \\ 1 & 1 & 1 & -1 & -1 & -1 \\ 1 & 1 & 1 & -1 & -1 & -1 \\ 1 & 1 & 1 & -1 & -1 & -1 \end{bmatrix} \tag{65}$$

$$\int_{-1}^{1} \frac{\partial N_i^t}{\partial t} N_j^t \, dt = \frac{1}{2} \begin{bmatrix} 1 & 1 & 1 & 1 & 1 & 1 \\ 1 & 1 & 1 & 1 & 1 & 1 \\ 1 & 1 & 1 & 1 & 1 & 1 \\ -1 & -1 & -1 & -1 & -1 & -1 \\ -1 & -1 & -1 & -1 & -1 & -1 \\ -1 & -1 & -1 & -1 & -1 & -1 \end{bmatrix} \tag{66}$$

Tracer advection matrix The advection matrix is a matrix of the A-type integral: $\int \mathbf{N} f(u_i) \nabla \mathbf{N} d\Omega$ written as

$$B_{ij} = \int_{\Omega} N_i v_{\alpha} \frac{\partial N_j}{\partial x_{\alpha}} \, d\Omega$$

With velocities given in the principal directions the expression reduces to

$$B_{ij} = v_{xx} \underbrace{\int_{\Omega} (N_i^{\Delta} N_i^t) \frac{\partial}{\partial x} (N_j^{\Delta} N_j^t) \, d\Omega}_{B_{ij}^{xx}} + v_{yy} \underbrace{\int_{\Omega} (N_i^{\Delta} N_i^t) \frac{\partial}{\partial y} (N_j^{\Delta} N_j^t) \, d\Omega}_{B_{ij}^{yy}}$$
$$+ v_{zz} \underbrace{\int_{\Omega} (N_i^{\Delta} N_i^t) \frac{\partial}{\partial z} (N_j^{\Delta} N_j^t) \, d\Omega}_{B_{ij}^{zz}}$$

The components B_{ij}^{xx}, B_{ij}^{yy} and B_{ij}^{zz} are again evaluated using equations 55 and 56. One obtains

$$B_{ij}^{xx} = det[J_{3D}^z] \underbrace{\int_{\Delta} N_i^{\Delta} \frac{\partial N_j^{\Delta}}{\partial x} \, dA}_{\mathbf{B}^{\Delta x}} \times \underbrace{\int_{-1}^{1} N_i^t N_j^t \, dt}_{\mathbf{C}^t} \tag{67}$$

$$B_{ij}^{yy} = det[J_{3D}^z] \underbrace{\int_\Delta N_i^\Delta \frac{\partial N_j^\Delta}{\partial y}\, dA}_{\mathbf{B}^{\Delta y}} \times \underbrace{\int_{-1}^{1} N_i^t N_j^t\, dt}_{\mathbf{C}^t} \quad (68)$$

$$B_{ij}^{zz} = \underbrace{\int_\Delta N_i^\Delta N_j^\Delta\, dA}_{\mathbf{C}^\Delta} \times \int_{-1}^{1} N_i^t \frac{\partial N_j^t}{\partial t}\, dt \quad (69)$$

with $\mathbf{C}^t$ the linear component of the capacitance matrix and $\mathbf{C}^\Delta$ the triangle component of the capacitance matrix as already given in equations 60 and 61. The left hand side integral of equations 67 and 68 can be written as

$$\mathbf{B}^{\Delta x} = \begin{bmatrix} \mathbf{b}^{\Delta x} & \mathbf{b}^{\Delta x} \\ \mathbf{b}^{\Delta x} & \mathbf{b}^{\Delta x} \end{bmatrix} \quad , \quad \mathbf{B}^{\Delta y} = \begin{bmatrix} \mathbf{b}^{\Delta y} & \mathbf{b}^{\Delta y} \\ \mathbf{b}^{\Delta y} & \mathbf{b}^{\Delta y} \end{bmatrix}$$

Integration of expressions $\mathbf{b}^{\Delta x}$ and $\mathbf{b}^{\Delta y}$ over the triangle area using formula 59 yields the 3x3 matrices

$$\begin{aligned} \mathbf{b}^{\Delta x} &= \frac{\partial N_j^\Delta}{\partial x} \int_\Delta N_i^\Delta\, dA \\ &= \begin{bmatrix} (y_2 - y_3) \\ (y_3 - y_1) \\ (y_1 - y_2) \end{bmatrix} \begin{bmatrix} 1 \\ 1 \\ 1 \end{bmatrix}^T \frac{1}{6} A \end{aligned}$$

$$\begin{aligned} \mathbf{b}^{\Delta y} &= \frac{\partial N_j^\Delta}{\partial y} \int_\Delta N_i^\Delta\, dA \\ &= \begin{bmatrix} (x_3 - x_2) \\ (x_1 - x_3) \\ (x_2 - x_1) \end{bmatrix} \begin{bmatrix} 1 \\ 1 \\ 1 \end{bmatrix}^T \frac{1}{6} A \end{aligned}$$

Now using equation 65 for the right hand side integral of equation 69 there is a complete expression for the tracer advection matrix.

Gravity forces Gravity forces are written as a matrix of g-type integral: $\int \nabla \mathbf{N} f(u_i) d\Omega$ which can be written as

$$\mathbf{g} = K \times (z)$$

3.4 Finite difference approach for channel flow

According to Jain (2001) the finite difference scheme for the governing equation (equation 41) using forward differences can be written as

$$\left(\frac{Q^2}{2A^2}+gh\right)_{i+1}-\left(\frac{Q^2}{2A^2}+gh\right)_{i}-g\left(S_{0,i}-\frac{S_{f,i}+S_{f,i+1}}{2}\right)(s_{i+1}-s_i) = f(h_i)=0 \tag{70}$$

The non-linearity is resolved by a Newton-Raphson method (see section 3.5.2)

$$h_i^*=h_i-\frac{f(h_i)}{f'(h_i)} \tag{71}$$

where h_i^* and h_i denote the result from the current and the previous iterative step, respectively. Finally the Newton-Raphson scheme yields the following equation for the determination of the water level.

$$h_i^*=h_i-\frac{\frac{Q^2}{2A_{i+1}^2}+gh_{i+1}-\frac{Q^2}{2A_i^2}-gh_i-g(S_{0,i}-\frac{S_{f,i}+S_{f,i+1}}{2})(s_{i+1}-s_i)}{\frac{Q^2}{A_i^3}(\frac{\partial A}{\partial h})_i-g+gS_{f,i}\left[\frac{\beta}{P_i}(\frac{\partial P}{\partial h})_i-\frac{1+\beta}{A_i}(\frac{\partial A}{\partial h})_i\right](s_{i+1}-s_i)} \tag{72}$$

where P denotes the wetted perimeter and β =2/3 or =1/2, if Manning's or Chézy's friction formula is used. Other forward difference schemes are shortly presented in the appendix in section 9.7.

3.5 Solving non-linear processes

In this section we present a description of selected iterative methods that are commonly applied to solve non-linear problems.

- Picard method (fixpoint iteration)
- Newton methods

All methods call for an initial guess of the solution to start with but each algorithm uses a different scheme to produce a new (and hopefully closer) estimate to the exact solution. The general idea is to construct a sequence of linear sub-problems which can be solved with an ordinary linear solver.

3.5.1 Picard

The general algorithm of the Picard method can be described as follows. We consider a non-linear equation written in the form

$$\mathbf{A}(\mathbf{x})\,\mathbf{x} - \mathbf{b}(\mathbf{x}) = 0 \tag{73}$$

We start the iteration by assuming an initial guess $\mathbf{x}_0$ and we use this to evaluate the system matrix $\mathbf{A}(\mathbf{x}_0)$ as well as the right-hand-side vector $\mathbf{b}(\mathbf{x}_0)$. Thus this equation becomes linear and it can be solved for the next set of $\mathbf{x}$ values.

$$\begin{aligned} \mathbf{A}(\mathbf{x}_{k-1})\,\mathbf{x}_k - \mathbf{b}(\mathbf{x}_{k-1}) &= 0 \\ \mathbf{x}_k &= \mathbf{A}^{-1}(\mathbf{x}_{k-1})\,\mathbf{b}(\mathbf{x}_{k-1}) \end{aligned} \tag{74}$$

Repeating this procedure we obtain a sequence of successive solutions for $\mathbf{x}_k$. During each iteration loop the system matrix and the right-hand-side vector must be updated with the previous solution. The iteration is performed until satisfactory convergence is achieved. A typical criterion is e.g.

$$\varepsilon \geq \frac{\parallel \mathbf{x}_k - \mathbf{x}_{k-1} \parallel}{\parallel \mathbf{x}_k \parallel} \tag{75}$$

where ε is a user-defined tolerance criterion. For the simple case of a non-linear equation $\mathbf{x} = \mathbf{b}(\mathbf{x})$ (i.e. $\mathbf{A} = \mathbf{I}$), the iteration procedure is graphically illustrated in Fig. 8. To achieve convergence of the scheme it has to be guaranteed that the iteration error

$$e_k = \parallel \mathbf{x}_k - \mathbf{x} \parallel < C \parallel \mathbf{x}_{k-1} - \mathbf{x} \parallel^p = e_{k-1} \tag{76}$$

or, alternatively, the distance between successive solutions will reduce

$$\parallel \mathbf{x}_{k+1} - \mathbf{x}_k \parallel < \parallel \mathbf{x}_k - \mathbf{x}_{k-1} \parallel^p \tag{77}$$

where p denotes the convergence order of the iteration scheme. It can be shown that the iteration error of the Picard method decreases linearly with the error at the previous iteration step. Therefore, the Picard method is a first-order convergence scheme.

The Picard method is implemented in GeoSys/RockFlow to solve non-linear equations for unsaturated flow, unconfined flow, density dependent flow, fracture flow and overland flow.

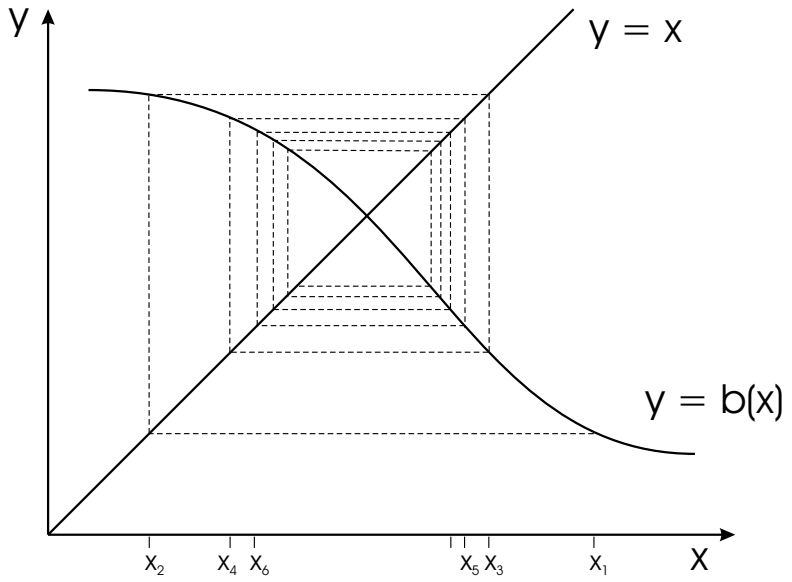

Figure 8: Illustration of the Picard iteration method, Kolditz (2002)

3.5.2 Newton-Raphson method

In order to improve the convergence order of non-linear iteration methods, i.e. derive higher-order schemes, the Newton-Raphson method can be employed. To describe this approach, we consider once again a non-linear equation.

$$\mathbf{R}(\mathbf{x}) = \mathbf{A}(\mathbf{x})\,\mathbf{x} - \mathbf{b}(\mathbf{x}) = 0 \tag{78}$$

Assuming that the residuum $\mathbf{R}(\mathbf{x})$ is a continuous function, we can develop a Taylor series expansion about any known approximate solution $\mathbf{x}_k$. Second- and higher-order terms are truncated in the following

$$\mathbf{R}_{k+1} = \mathbf{R}_k + \left[\frac{\partial \mathbf{R}}{\partial \mathbf{x}}\right]_k \Delta\mathbf{x}_{k+1} + 0\,(\Delta\mathbf{x}_{k+1}^2) \tag{79}$$

The term $\partial\mathbf{R}/\partial\mathbf{x}$ represents tangential slopes of $\mathbf{R}$ with respect to the solution vector and it is denoted as the Jacobian matrix $\mathbf{J}$. As a first approximation we can assume $\mathbf{R}_{k+1} = 0$. Then the solution increment can be immediately calculated from the remaining terms in equation (79).

$$\Delta\mathbf{x}_{k+1} = -\mathbf{J}_k^{-1}\,\mathbf{R}_k \tag{80}$$

where we have to cope with the inverse of the Jacobian. The iterative approximation of the solution vector can be computed now from the increment.

$$\mathbf{x}_{k+1} = \mathbf{x}_k + \Delta\mathbf{x}_{k+1} \tag{81}$$

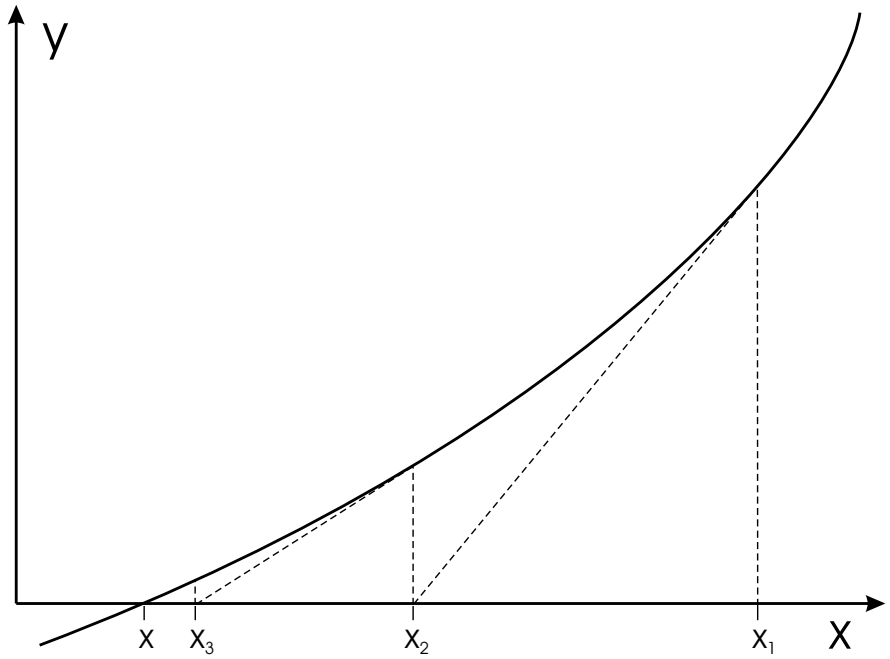

Figure 9: Illustration of the Newton-Raphson iteration method, Kolditz (2002)

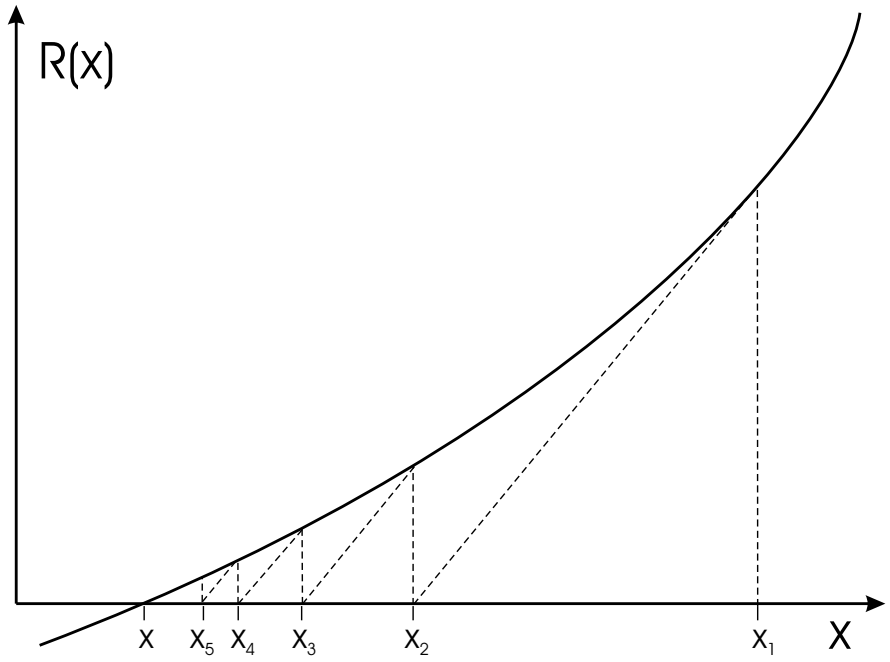

Figure 10: Illustration of the modified Newton-Raphson iteration method, Kolditz (2002)

Once an initial guess is provided, successive solutions of $\mathbf{x}_{k+1}$ can be determined using equations (80) and (81) (Fig. 9). The Jacobian has to re-evaluated and

inversed at every iteration step, which is a very time-consuming procedure in fact. At the expense of slower convergence, the initial Jacobian $\mathbf{J}_0$ may be kept and used in the subsequent iterations. Alternatively, the Jacobian can be updated in certain iteration intervals. This procedure is denoted as modified or 'initial slope' Newton method (Fig. 10).

The convergence velocity of the Newton-Raphson method is second-order. It is characterized by the expression.

$$\| \mathbf{x}_{k+1} - \mathbf{x} \| \leq C \| \mathbf{x}_k - \mathbf{x} \|^2 \tag{82}$$

Overland flow

In order to apply the Newton-Raphson method to the overland flow equation (equation 28) the expression is written in the finite element notation

$$\begin{aligned} \int_{\Omega^e} \underbrace{N_i N_j \, d\Omega^e}_{C_{ij}} \frac{dh_j}{dt} + \int_{\Omega^e} \underbrace{\frac{\partial N_i}{\partial x_\alpha} k_{eq} H \frac{\partial N_j}{\partial x_\beta} \, d\Omega^e}_{K_{ij}} h_j \\ = - \int_{\partial\Omega^e} \underbrace{N_i q_n^O dS^e + \int_{\Omega^e} N_i Q_\rho d\Omega^e}_{r_i} \end{aligned} \tag{83}$$

where C_{ij} is the overland flow capacitance matrix, K_{ij} is the overland flow advection matrix and r is the right hand side (RHS) vector for overland flow. The residuum $\mathbf{R}$ is given by

$$R_i = C_{ij} \frac{h_j + h_j^0}{\Delta t} + K_{im} h_m - r_i \tag{84}$$

where h_j^0 is the converged solution of the previous timestep. The tangential slope of $\mathbf{R}$ is given by

$$\mathbf{J} = \frac{d\mathbf{R}}{d\mathbf{h}} := \frac{\partial R_i}{\partial h_j} = \frac{C_{ij}}{\Delta t} + K_{ij} + \frac{\partial K_{im}}{\partial h_j} h_m \tag{85}$$

$$\frac{\partial K_{ij}}{\partial h_j} h_j = \int_{\Omega^e} \frac{\partial N_i}{\partial x_\alpha} \frac{\partial N_j}{\partial x_\beta} \frac{d(K_{eq} H)}{dh} N_j \, d\Omega^e h_j \tag{86}$$

$$\begin{aligned} \frac{d(K_{eq}H)}{dh} &= K_{eq} + H \frac{dK_{eq}}{dh} \\ &= K_{eq} + H \frac{d}{dh} \left[\frac{H^{2/3}}{n^2} \frac{1}{Ss^{1/4}} \right] \\ &= K_{eq} + H \left[\frac{2}{3n^2} H^{-1/3} \frac{1}{Ss^{1/4}} - \frac{H^{2/3}}{n^2} \frac{1}{4} Ss^{-5/4} \frac{dSs}{dh} \right] \\ &= K_{eq} \frac{2}{3n^2} H^{2/3} \frac{1}{Ss^{1/4}} + \frac{H^{5/3}}{n^2} - \frac{1}{4} Ss^{-5/4} \frac{dSs}{dh} \end{aligned} \tag{87}$$

and $\frac{dSs}{dh}$ is evaluated numerically. The new solution vector can now be calculated

$$h_{k+1} = h_k + \Delta h_{k+1} = h_k - \mathbf{J}_k^{-1}\mathbf{R}_k \tag{88}$$

4 Object-oriented approach to process modelling

Object-oriented programming (OOP) methods are becoming more and more important in scientific computing in order to develop software in teams, and to be able to extend the code continuously for new applications (Masters et al. (1997)). The earliest use of OOP was connected with graphical applications and data visualization. These developments were instigated by natural analogs such as geometric objects, i.e. circles, triangles, spheres etc., treated as graphic objects. Another trigger for OOP was the requirement of graphical user interfaces (GUI) in order to handle more and more complex software. Utilization of OOP in numerical analysis started in the 1990s (Mackie (1992); Scholz (1992); Zimmermann et al. (1992)). OOP was also successfully introduced in several branches of computational mechanics, e.g. stress analysis (Dubois-Pelerin and Zimmermann (1993)), structural analysis (Pidaparti and Hudli (1996)), shell structures (Ohtsubo et al. (1993)), inelastic strain analysis (Mentrey and Zimmermann (1993)), contact problems (Feng (1995)), fluid dynamics (Peskin and Hardin (1996), Kolditz (2002)), heat transfer and solidification (Cross et al. (1998)).

In the context of geosystem modelling, we use OOP to face a large variety of problems in environmental fluid mechanics. These include single or multi phase phase flow in porous and fractured media, transport of solutes or heat in porous and fractured media and deformation processes in geotechnical systems. Furthermore, chemical reactions have to be calculated when dealing with contaminated aquifers.

The purpose of this section is to present an object-oriented design for the implementation of the finite element method for groundwater resource studies. The papers Beinhorn and Kolditz (2004a) and Beinhorn and Kolditz (2004b) (see list of publications, section 9.8) deal also with that issue.

Basic modules of GeoSys (Kolditz et al. (2003)) are the GeoLib, MshLib, and FEMLib, which can be connected via a Graphical User Interface (GUI). The modules are described below

4.1 GeoLib

Geometric objects of the GeoLib are points, polylines, surfaces, volumes which form domains. All these geometric entities are implemented as C++ classes: `CGLPoint`, `CGLPolyline`, `CGLSurface`, `CGLVolume`, `CGLDomain`. Instances of these objects can alternatively be stored in vectors and lists for convenience and specific purposes. As an example Fig. 11 shows geometric information of the hydrogeological system further described in section 6.1 within the framework of the GUI. A detailed description of the implementation of GeoObjects is given in Kalbacher et al. (2003b).

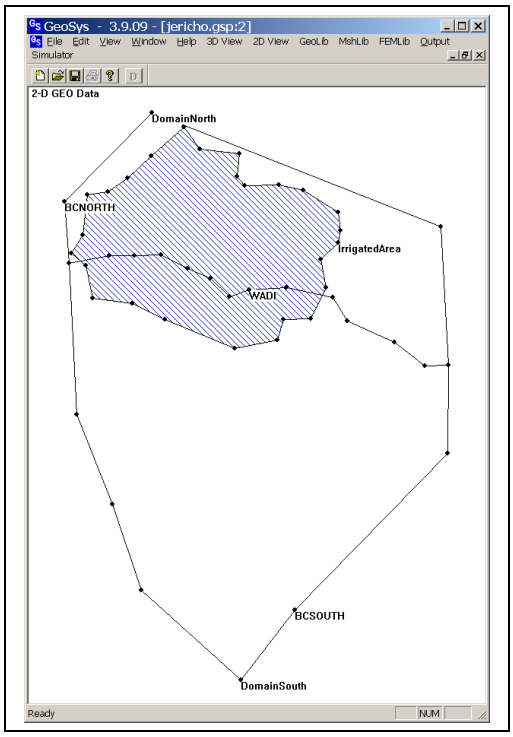

Figure 11: GeoLib containing points, polylines and surfaces

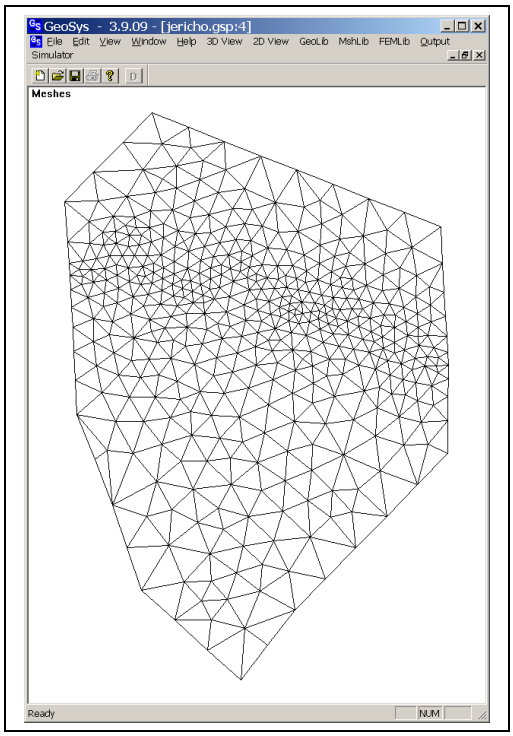

Figure 12: MshLib containing nodes and elements

4.2 MshLib

Geometric information forms the basis for mesh generation. For the meshing of complex geosystems such as fractured and karstified aquifers very flexible mesh generators are necessary. Currently, following build-in mesh generators can be used: PrisGen (Kalbacher et al. (2003a)), TetMesh (Manabe et al. (2003)) as well as open and commercial systems such as gmsh (2004) and gOcad (2004). Fig. 12 shows the topological information resulting from the geometric data given in the GeoLib in Fig. 11.

The resulting mesh geometry can be manipulated using mesh operations like the mapping operation. Here a surface object (SFCObj) is being used to relate mesh data to a surface data file such as top or bottom of a hydrostratigraphical unit. An additional operation of the MshLib is vertical mesh refinement. All these operations of the MshLib are controlled via an GUI as displayed in Fig. 14.

4.3 FEMLib

The FEMLib contains independent units necessary to set up and solve the finite element problem (see Table 2). As a result of the numerical approximation method described in section 3, two sets of algebraic equations were derived

Table 2: RF/RM objects

Acronym	Subject	Examples
GEO	geometric objects	points, polylines, surfaces, volumes
ELE	elements	different finite element types
IC	initial conditions	$u_i(t = 0, x)$
BC	boundary conditions	$u_i(t, x = b)$
ST	source terms	$\nabla u_i(t, x = b)$
MAT	materials	fluid, solid, porous medium properties
NUM	numerics	parameter of numerical method
TIM	time	parameter of time discretization
KER	kernel	finite element matrices
EQS	equation system	system matrix, solution vector, RHS vector

(equations 43 and 42). The general form of these equation is

$$\mathbf{A}_i(t, \mathbf{x}, \mathbf{u}_i, \mathbf{u}_j)\, \mathbf{u}_i = \mathbf{b}_i(t, \mathbf{x}, \mathbf{u}_i, \mathbf{u}_j)$$

where i, j denote different processes, with $\mathbf{A}_i$ system matrix of process i, t time, $\mathbf{x}$ coordinates, $\mathbf{u}_i$ solution vector (primary variable) of process i, $\mathbf{b}_i$ RHS vector of process i. Dependence of process i on process j means coupling, and dependence of system matrix on solution itself means non-linearity. Now the required data structure and algorithms can be generalized for every process to be modelled:

1. Initialize equation system and solution vector.
2. Calculate element matrices.
3. Assemble equation system.
4. Incorporate boundary conditions and source terms.
5. Solve equation system.
6. Calculate secondary variables.
7. Store results for next iteration / step.

This approach allows to treat different processes in an object oriented way. Processes are implemented as objects (PCS) organized in a class `CRFProcess` containing all information and data required. Data structures as well as the grid and time stepping are common for all processes, whereas the parameters, initial conditions boundary conditions and the type of equations and thus also the solving techniques used may vary from process to process. Fig. 13 gives a graphical illustration of the PCS relationships to other objects. Information from these objects is required to create and solve a process. The most important methods of the `CRFProcess` class are:

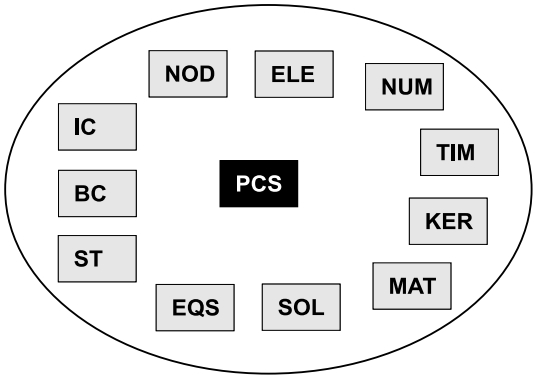

Figure 13: Relationships of processes

```
1 - void CRFProcess:: PCSCreateProcesses(void)
2 - void CRFProcess:: PCSConfigProcess(int pcs_type)
3 - void CRFProcess:: PCSExecuteProcess(EQUATION_SYSTEM *pcs_eqs)
```

With the first step the data structures of PCS are created: This is basically the equation system (EQS) and pointers to the basic objects given in Table 2. Depending on the type of process (e.g. flow or tracer transport) the PCS object is configured in the second function. In this step virtual PCS functions are overwritten, i.e. a specific function to calculate element matrices is selected. The processes created are inserted into a list, which is the last step of the pre-processing part. In the processing part (the third function), PCS instances are executed with the general steps described above but with specified properties and methods.

For nonlinear or coupled problems we have to consider process interactions: In the case of density dependent flow the solution vector for fluid flow $\mathbf{p}$ yields the data for the element resultant advective flux $\mathbf{q}$, which is than needed to calculate the transport process. The transport process in return delivers mass fractions ω (or concentrations) which again have an influence on the flow process. A process must therefore be able to use solution vectors or resultants of other processes. Hence data access functions to nodes (NOD) and elements (ELE) were implemented into the `CRFProcess` class via node and element lists.

As a result we have a very flexible computation scheme concerning the number of processes and a flexible way to define interaction between processes. An arbitrary number of processes can be generated, configured and solved so that complex systems including flow, transport and deformation processes can be modelled (Kolditz and Bauer (2004)).

Fig. 14 is showing the graphical user interface of GeoSys/RockFlow with the relationships between the two objects MshLib and GeoLib: A mesh object can be manipulated using mesh operations like the mapping operation. Here a surface object (SFCObj) is being used to relate mesh data to a surface data such as top or bottom of a hydrostratigraphical unit. An additional operation of the MshLib

is vertical mesh refinement. All these operations of the MshLib are controlled via the graphical user interface.

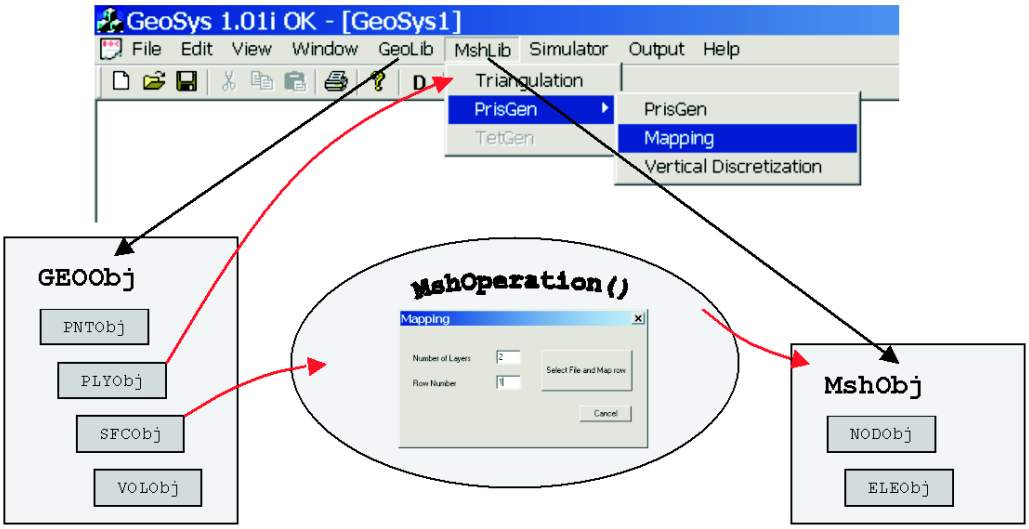

Figure 14: Graphical User Interface displaying relationships between GeoLib and MshLib

5 Code verification

Model verification concerns the new components included into the GeoSys/RockFlow software. Tested were the new element type of triangular prismatic elements for fluid flow, unconfined flow and density dependent flow and also the new overland flow component. Where possible the results were compared to analytical solutions or results calculated using other element types. Results of the overland flow process were crosschecked with results from the model Hydrosphere (2004) or solutions given in literature.

5.1 Linear groundwater flow and transport

In the first example groundwater flow through a horizontal bar of 100 m length, 1 m height and 1 m width is considered. A hydrostatic pressure distribution is assigned on the right hand side, a total flux of 1.157E-06 m^3/s is fixed entering the domain on the left hand side boundary. The conductivity K is 1.00e-12 m^2. The resulting pressure distribution meets the result given by Darcy's law. Geometry, boundary conditions and the result are displayed in Fig. 15.

In example 2 horizontal groundwater flow is considered. Water is entering the domain through the hydrostatic pressure distribution assigned on the front right hand side and leaving the domain through the hydrostatic pressure distribution assigned on the front left hand side. The resulting pressure distribution meets the expected results and corresponds to the results given from the example sm2dtri. Geometry, boundary conditions and the result are displayed in Fig. 16.

Vertical groundwater flow through a bar of 2 m height, 1 m width and 1 m depth consisting of 4 elements is considered in example 3. The conductivity K is 1.00e-12 m^2. A constant pressure condition is applied at the four nodes at the top. A total flux of 1.157e-06 m^3/s is fixed to enter the domain from below. Care must be taken to assign the right fluxes considering the number of elements shared by a node in order to create a homogeneous flow field. Model geometry and boundary conditions are displayed in Fig. 17. The resulting pressure distribution meets the result given by Darcy's law and can be seen in Fig. 18.

The first transport example concerns conservative tracer transport through a uniform flow field imposed by assigning appropriate constant head boundary condition. A constant concentration is set to 100 at the inflow side. The resulting concentration distribution of the tracer plume is shown in Fig. 19 and has been tested against an analytical solution. This example has also been tested for flow along all other coordinate directions and at different angles to the main axis. This is important to test all 9 components of the tracer diffusion/dispersion matrix given in equation **??**. In order to check all components of the transport equations more efficiently for future software versions the following test example has been designed:

In the example shown in Fig. 20 a uniform flow field diagonally through a cube of 20 m edge length is imposed by assigning appropriate constant heads at the surfaces. A constant concentration is set to 100 at the right hand side back corner. The resulting concentration distribution is shown by the isosurfaces in Fig. 20. As expected a symmetrical plume is pointing diagonally towards the front bottom left hand side corner.

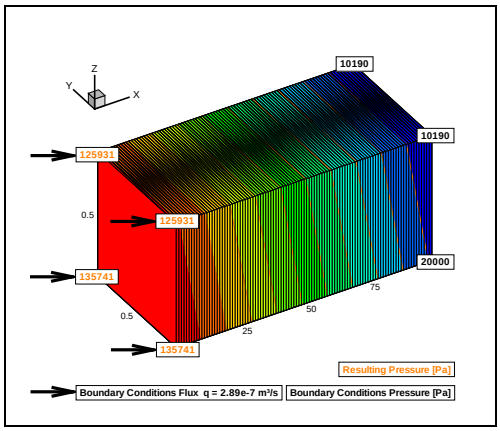

Figure 15: Groundwater flow example 1: Geometry, boundary conditions and resulting pressure distribution

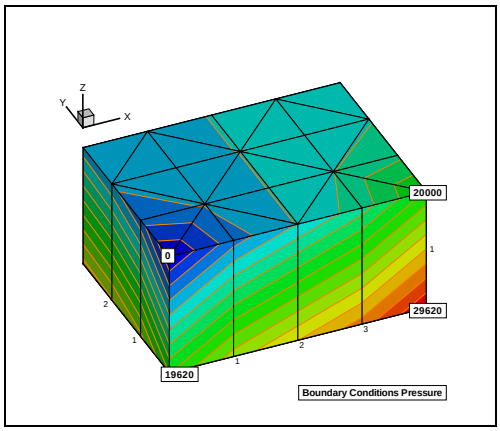

Figure 16: Groundwater flow example 2: Geometry, boundary conditions and resulting pressure distribution

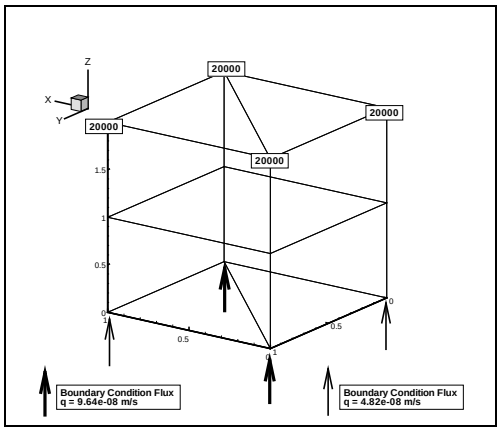

Figure 17: Groundwater flow example 3: Geometry and boundary conditions

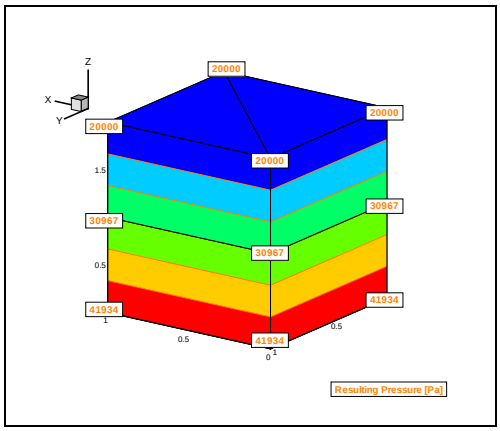

Figure 18: Groundwater flow example 3: Resulting pressure distribution

5.2 Non-linear groundwater flow

The Henry problem shown in Fig. 23 describes the advance of a saltwater front in a confined aquifer which was initially saturated with fresh water. The boundary conditions for flow are impermeable boundaries along the top and bottom,

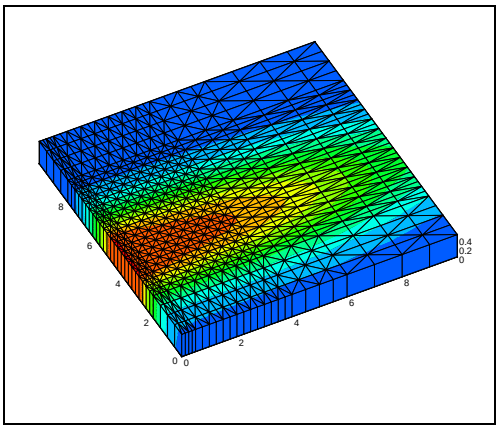

Figure 19: Tracer transport, flow along the x-axis

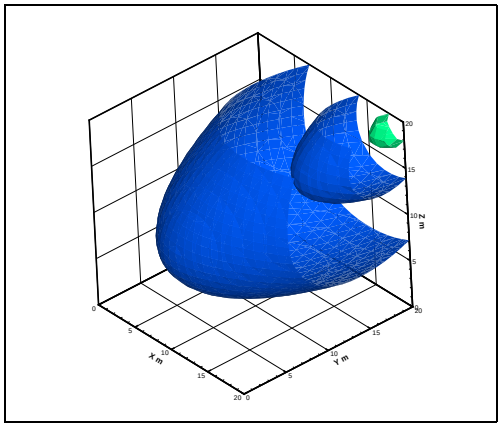

Figure 20: Tracer transport in a three-dimensional flow field

hydrostatic pressure along the sea side and a constant flux form the left hands side. At the left hand side the concentration is zero, at the sea side a normalized concentration of sea water is imposed. Detailed information on simulation parameters are given in Kolditz et al. (1998). The flow patterns associated with the standard Henry problem are largely dictated by the boundary forcing and not necessarily a result of density-dependent effects (Simpson and Clement (2004) and Simpson and Clement (2003)). However it is often used as a benchmark for variable density flow and transport and in this study serves to show that the non-linear iteration works in principle. The resulting concentration distribution shown in Fig. 23 is in good agreement with work quoted in Kolditz et al. (1998).

The following example was designed to test the new moving mesh approach to unconfined groundwater flow in an two-dimensional test case displayed in Fig. 21: An earth dam separates two water reservoirs at different piezometric heads. In addition to the phreatic surface there is a seepage face across which water may leave the domain at atmospheric pressure. The seepage face is represented by a conditional fixed pressure boundary condition. The condition is only applied if flux is negative, i.e. out of the domain. The length of the seepage face is a priori not known but is determined during the iterative process. The original mesh in Fig. 21 is light grey in color. After the simulation the head distribution is represented by the 'deformed' mesh in black. The red line shows the result of the analytical solution according to the Dupuit approximation of horizontal groundwater flow.

The next examples concerns the new process unconfined flow for the new element types. Flow through a unconfined aquifer of 100 m length, 1 and 2 m width is taking place. A hydrostatic pressure distribution is assigned on the right- and left hand side, a recharge flux of 1.0e-08 m/s is applied to the upper model boundary. The conductivity K is 1.00e-12 m^2. The resulting pressure distribution meets the result given by the analytical solution of the problem. Geometry, boundary conditions and the result are displayed in Fig. 22.

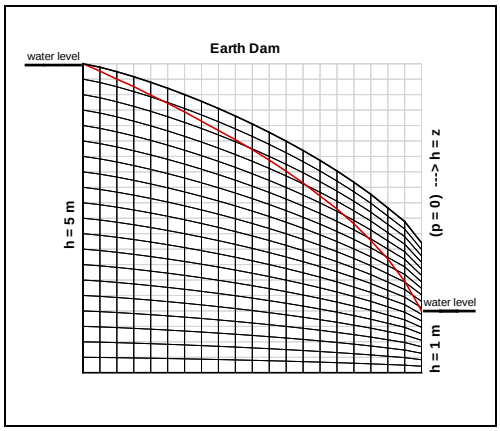

Figure 21: Unconfined flow example earth dam: Boundary conditions and resulting head distribution, initial mesh in grey, resulting mesh in black

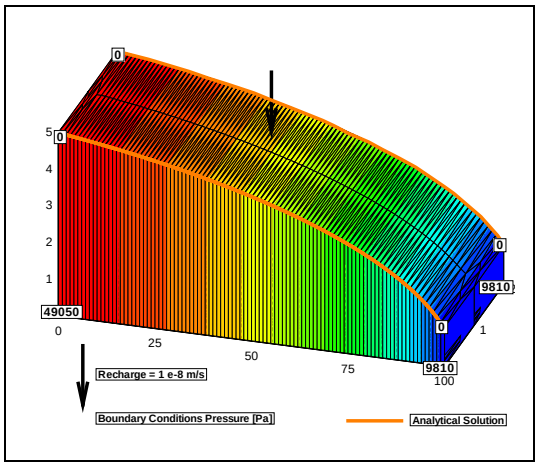

Figure 22: Unconfined flow example using triangular prisms: Boundary conditions and resulting head distribution and mesh geometry

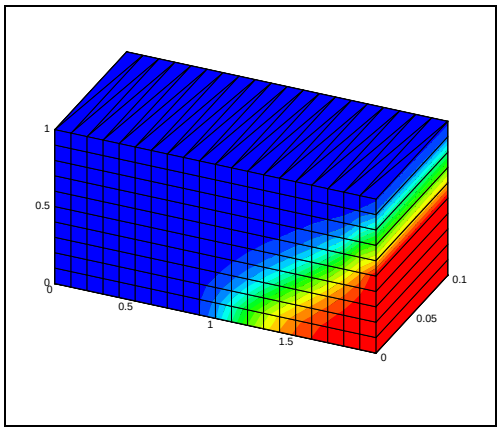

Figure 23: Density dependent flow, Henry problem

5.3 Performance

The performance of the analytical method for the element matrix evaluation was tested using the diffusion/dispersion example shown in Fig. 20. The mesh contains 160.000 elements. The numerical evaluation of all element matrix expressions takes 44 seconds. Using the new analytical method the CPU time reduces to 9 seconds. Hence required computation time is reduced by a factor 0.2. Considering the total CPU time including the solution of the global equation system (equations 42 and 43) the reduction factor can increase to 0.6.

5.4 Overland flow

The first example concerns steady state overland flow for the special case of a horizontal surface. Geometry, boundary conditions and the resulting water surface curves are given in Fig. 24. There is a fixed head boundary condition downstream and a constant flux of $1.0e{-}3m^3/s$ upstream. The Chézy-coefficient C is set to 10. According to Rijn (1986) there is an analytical solution to the steady state flow equation for the special case of flow over a horizontal bed given in equation 29. Results of another numerical solution realized in Excel and the analytical solutions are also plotted in Fig. 24 and show a good fit.

Geometry and boundary conditions of the overland flow example illustrated in Fig. 25 are the same as given in the previous example. Only now the channel or overland flow domain has a slope of 4 cm on length of 100 m. Results of the new modelling code are plotted along with the numerical solution realized in Excel in Fig. 25 and show a good fit.

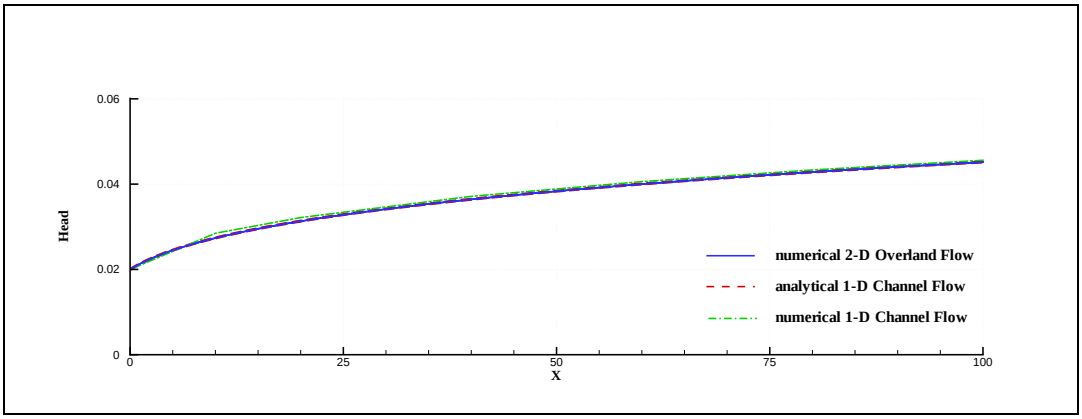

Figure 24: Overland flow example, steady state with horizontal channel bed

The next example is a simplified version of the 'level V-catchment' example given in Giammarco et al. (1996) and concerns a transient flow problem: We have a domain of 800 x 100 m with a slope of 0.05 and a manning coefficient of 0.015. Recharge of an intensity of $3e-6m/s$ is applied to the whole region for an interval of 90 minutes. Total simulation time is 180 minutes. A critical depth boundary condition is assigned at the downstream nodes where x = 800 m. In this example we used an initial water level of 0.0 m. The resulting water depth calculated with GeoSys is plotted in Fig. 26. The graphs in Fig. 27 displays resulting hydrographs for the models GeoSys and Hydrosphere. Small differences are a result of a minimum depth condition, at which water starts to move. In hydrosphere that value is fixed and cannot be specified by the user.

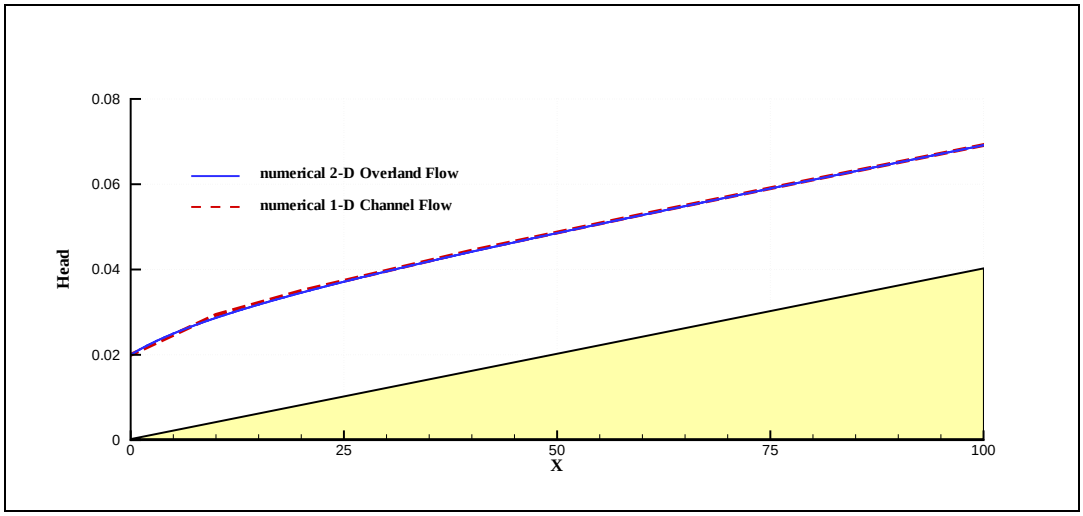

Figure 25: Overland flow example, steady state with a sloping channel bed

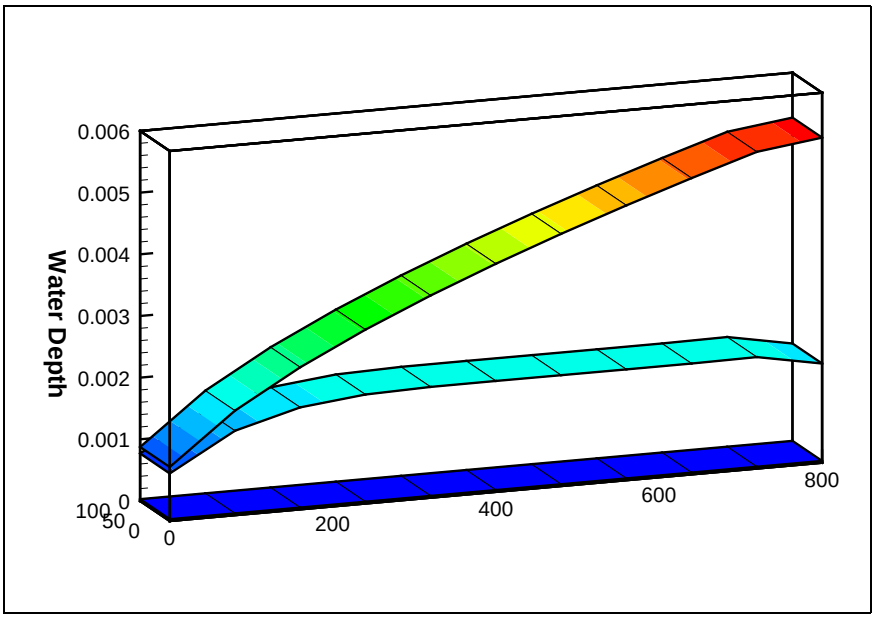

Figure 26: Water surface elevations at different times, GeoSys

6 Applications

6.1 Groundwater flow and transport model of the Jericho area

6.1.1 Introduction

The shallow aquifer concerned here consists of alluvial deposits, clay silts, conglomerate, chalk, marl and gypsum layers of the Lisan formation. Due to the

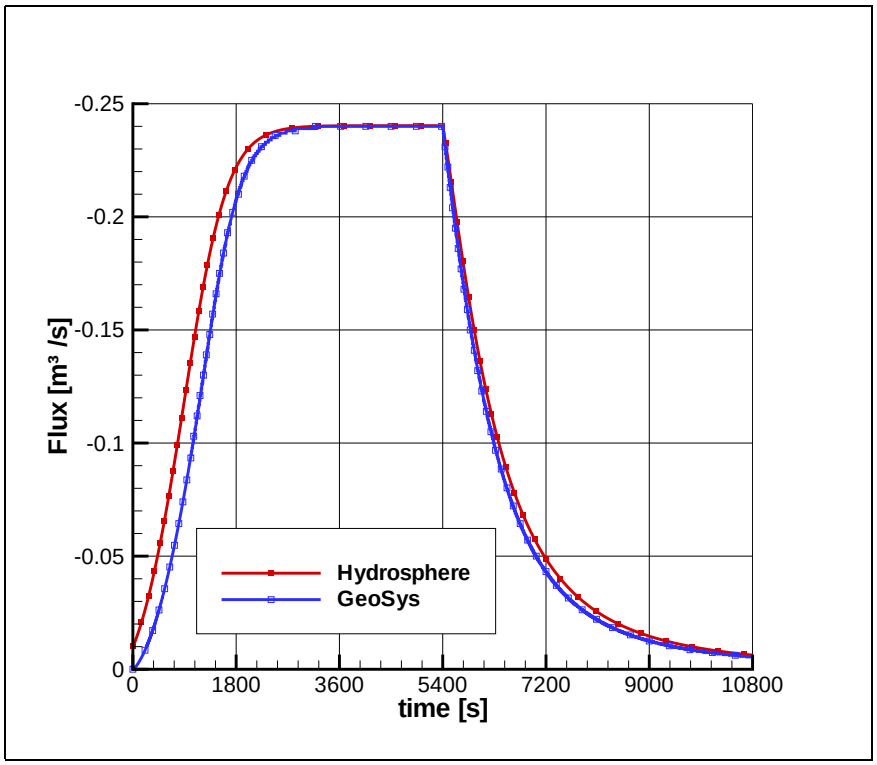

Figure 27: Hydrographs with calculated with GeoSys and Hydrosphere

high water demand in the area of Jericho and consequently high groundwater abstraction rates as well as irrigation back-flow, groundwater quality in the aquifer has deteriorated considerably. Detailed investigations performed by Marie and Vengosh (2001) using geochemical data suggest that high chloride contents, particular in the eastern part of the aquifer, are derived from several sources. They include:

- upconing of deep brines
- leaching of salts within the aquifer
- anthropogenic contamination of agriculture return flow and waste water infiltration

Another possible source of salinity is residual waters resulting from formerly higher Dead Sea water levels: 15,000 years ago the water level reached with about 230 m above the present Dead Sea level its maximum. The Lisan sea, a precursor of the present sea, covered large areas of the Jordan Valley up to an elevation of 180 m below sea level at that time (Begin et al. (1974)). The model domain is located within that elevation range and as a result the underlying rocks and sediments were saturated with saltwater.

A hydrogeological model of the area has been developed based on data available from project partners. A numerical model was used to improve and verify the hydrogeological model. The work done does not deal with the evaluation of possible sources of salinity. The aim was to put some constrains on boundary conditions and hydraulic properties of the aquifer and thus gain an understanding of the hydrogeology of the area.

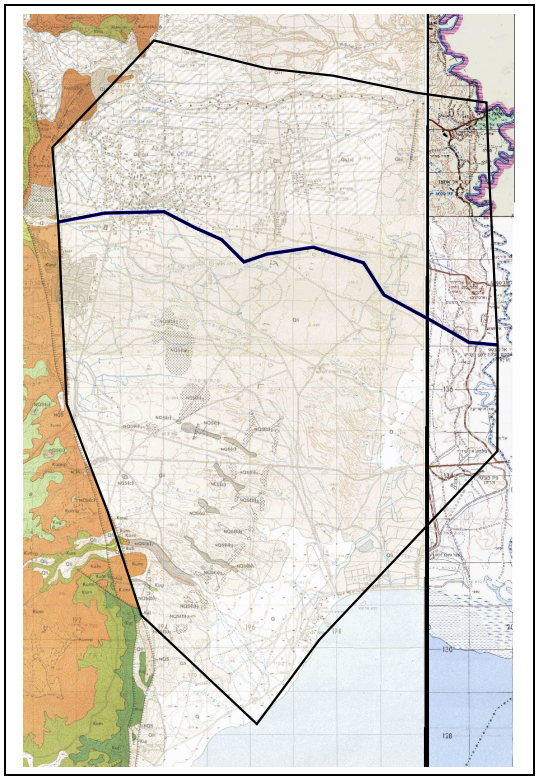

Figure 28: Model domain and geological and topological map in ArcGIS

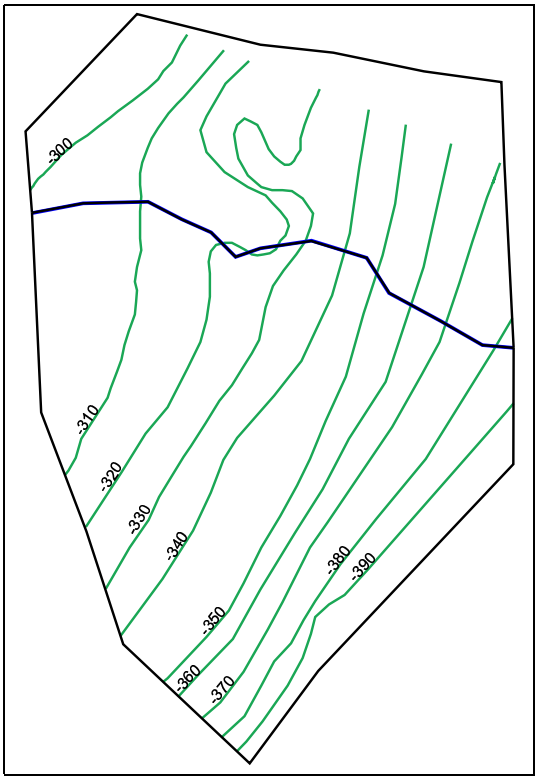

Figure 29: Model domain and groundwater contour map from 1982

6.1.2 Data availability and data handling

Hard copies of topological and geological maps and satellite images were available. Relevant information is also taken from a groundwater resources report: Golani (1972). Additional information was added by personal communication during project meetings. Altogether the following data set is available for the modelling study:

- Topological and geological maps: 1:50.000
- Satellite images
- Groundwater abstraction rates from wells of the shallow Plio/Pleistocene aquifer for the years $1961/63, 1968, 1969/70$

- Yearly spring discharge volumes of the Jericho springs Sultan, Duyuk, Nueima, Shosha and Uja
- Groundwater contour lines for the year 1982
- Chloride concentration contour maps for the years: $1961/63, 1968, 1969/70$
- Pumping test map

Topological and geological maps and satellite images were scanned, georeferenced and than placed in an ArcGIS project. Contour maps were digitized and than also placed in an ArcGIS project. Tables of groundwater extractions and spring discharges were stored and organized using Excel and than partly displayed as ArcGIS point themes.

6.1.3 Model geometry and model boundaries

The model domain is defined using geological and topographical maps and groundwater level information. Based on that information displayed as ArcGIS themes (see for example Fig. 28 and Fig. 29) the following model boundaries where chosen:

- SW, main rift fault, Upper- and Lower Cenomanian are adjacent to the Plio-Pleistocene aquifer
- NW, minor fault, Upper- and Lower Cenomanian are adjacent to Plio-Pleistocene aquifer
- N, boundary flow line
- E, Jordan river area
- SE, Dead Sea, Jordan river area

6.1.4 Model concept

Standard procedures of model calibration can not be adapted here as reliable measurements of groundwater heads remain elusive. As an alternative it is envisaged to use time series of chloride concentration maps for the model calibration. Concentration contour maps are available from Golani (1972) for the years: 1961/63, 1968 and 1969/70. The information available is displayed in Fig. 30 and 31.

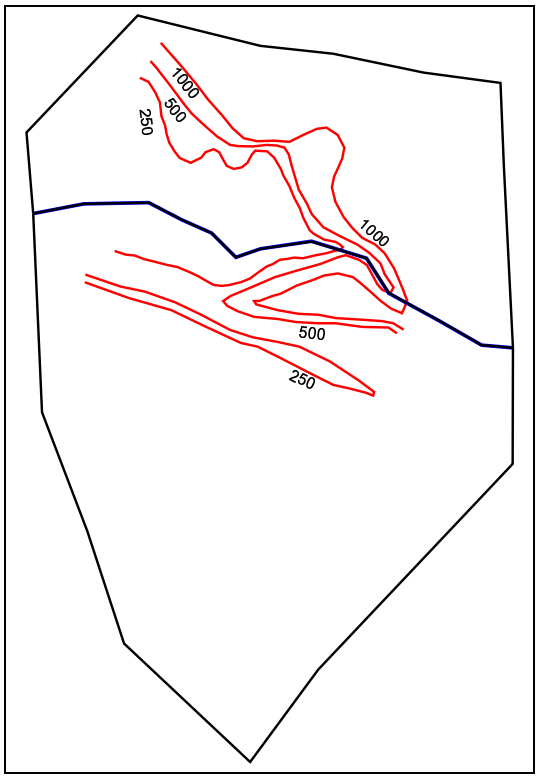

Figure 30: Concentration contours from 1961 in ArcGIS

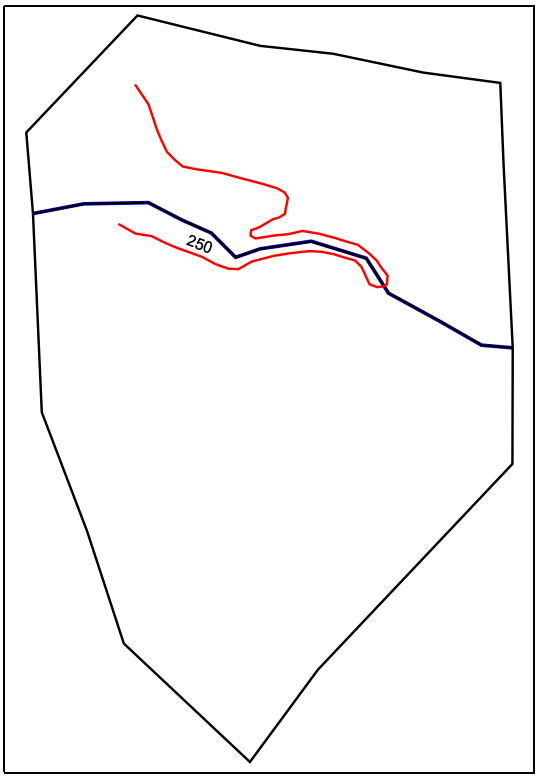

Figure 31: Concentration contours from 1970 in ArcGIS

6.1.5 Water balance

Recharge

The main recharge in the area is taking place through irrigation measures as well as through flooding of the wadis during the wet month in winter. Irrigated land covers an area of ca. 28 km^2. Water for the irrigation is taken from the springs Sultan, Duyuk and Nueima which are located outside the modelled area. Spring discharge volume are given in Table 3. Only 2/3 of the irrigated area served from the Duyuk spring are located in the modelled area. Hence only 2/3 of that spring discharge contribute to the recharge estimation. The total yearly averaged spring discharge and therefore water used for irrigation is 12 MCM. An estimate of 10 to 15 % of that water contribute to recharge by canal leakage and irrigation backflow leaving 1.2 to 1.8 MCM per year for recharge. The irrigated area is determined using a recent satellite image of the area studied (see Fig. 32). Recharge through flooding of the wadis is estimated to reach the order of 2 MCM per year. Recharge due to rain is negligible but additional water enters the domain at its NE-boundary. The irrigated areas and the location of the wadi are displayed in Fig. 33.

Table 3: Yearly discharge volumes of the Jericho springs

year	Sultan [1000 m^3/a]	Duyuk [1000 m^3/a]	Nueima [1000 m^3/a]
79/80	4753	5460	2403
79/81	5536	5672	2555
79/82	5674	5065	2974
79/83	5910	4955	3136
79/84	5833	4885	3136
79/85	5628	4864	3124
79/86	5465	4673	2920
79/87	5569	5115	2645
79/88	5915	4954	2867
79/89	5873	5051	2939
79/90	5837	5079	3047
79/91	5720	4802	2950
79/92	5856	5219	2959
79/93	5980	4819	3141
79/94	5957	4755	3194
79/95	5965	4768	2972
79/96	5939	4477	3123
79/97	5660	4460	2891
79/98	5870	4430	2960
79/99	5463	3954	2950
79/00	5349	4094	2718
total mean	5702	4836	2934
area factor	1	0.66	1
total mean in area	5702	3192	2934

Groundwater abstraction

Groundwater abstraction is taking place at ca. 80 wells in the Jericho area. Total abstraction rates for the years 1961/63, 1969/70 and 1968 amount to 2.7, 1.3 and 1.6 10e6 m^3/a. The last value corresponds to a yearly abstraction of ca. 5 MCM. Well locations are displayed in Fig. 33.

6.1.6 Hydraulic properties

From a map containing well test data the values given in Table 4 could be extracted. However the data given does not allow for a detailed resolution of different conductivity zones and the average value of 3.4 m/d is not assumed to be representative for a regional conductivity value. The first layer of a thickness of 20 m is allocated a permeability of 1 m/d in the West and 0.5 m/d in the East as seen in Fig. 34 in accordance to the distribution of coarse deposits in the West and finer material in the East. The second layer of a thickness of 10 m is assigned a value of 0.5 m/d.

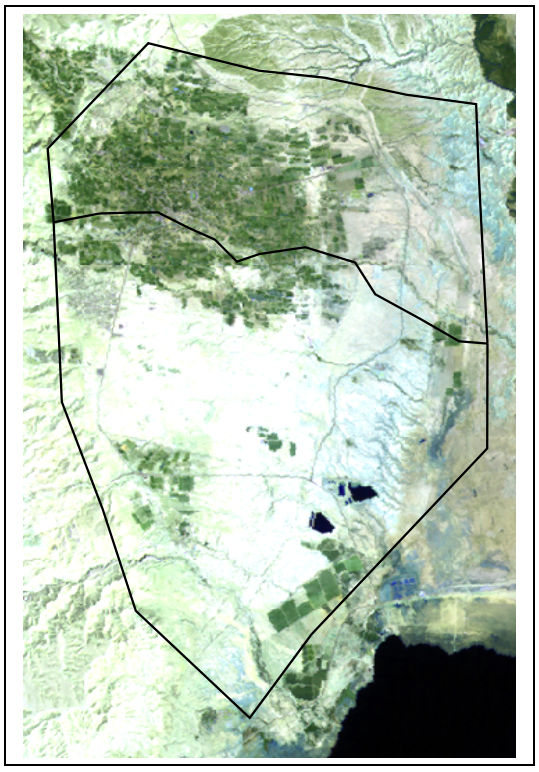

Figure 32: Satellite image for the determination of irrigated areas

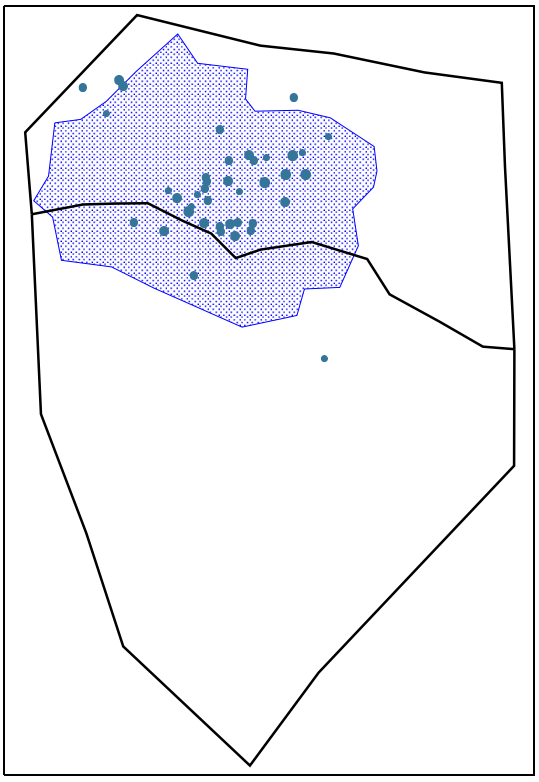

Figure 33: Wadi and well locations and irrigated areas in ArcGIS

6.1.7 Model discretization, boundary conditions and source/sink terms

The model domain was discretized using triangular prismatic elements for reasons given in Beinhorn and Kolditz (2003a,b). 6 layers of 525 elements each form the total domain. The edge length reaches from 500 m at the model boundaries to 200 in the vicinity of the wadi. The following boundary conditions were assigned to the model domain:

- SE, main rift fault: no flow boundary condition
- NW, minor fault: constant head boundary condition

Table 4: Transmissivities T, saturated thicknesses Ds and hydraulic conductivities K extracted from a pumping test map

					T	Ds	K
WELLID	WELLNAME	CoordX	CoordY	Top Elevation	m^2/day	m	m/d
13819803	19-13/12	198.98	138.31	-350.00	230	90	2.56
13919503	19-13/50	195.81	139.38	-290.00	160	45	3.56
13919601	19-13/15	196.15	139.50	-292.44	25	30	0.83
14019509	19-14/17	195.92	140.31	-290.00	180	20	9.00
14019603	19-14/71	196.87	140.09	-302.00	120	125	0.96
14219701	19-14/81	197.06	142.31	-302.07	430	???	

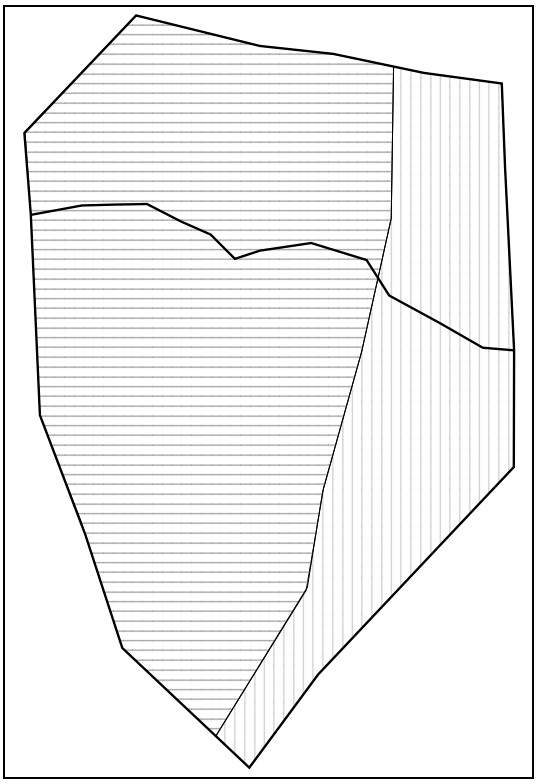

Figure 34: Material groups in the first layer displayed as ArcGIS themes

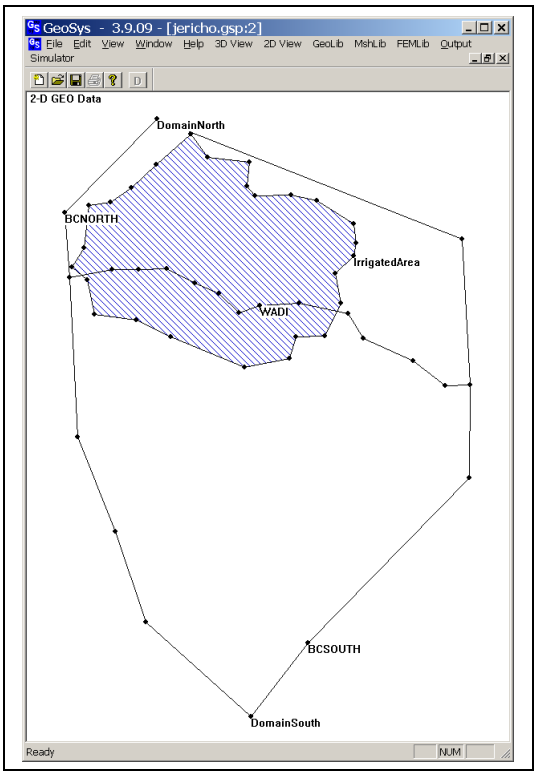

Figure 35: Elements of the GeoLib displayed in the GeoSys GUI

- NE, boundary flow line: no flow boundary condition
- E, Jordan river area: constant head boundary condition
- SE, Dead Sea, Jordan river area: constant head boundary condition

The medium abstraction rates of the years 1961/63, 1969/70 and 1968 were assigned to nodes close to active well locations. Along the polyline of the Wadi a source term with 2MCM over the total Wadi length is defined.

6.1.8 Modelling software

The numerical model used for the simulations is the FE Simulater GeoSys/RockFlow (Kolditz et al. (2003)) which is programmed in C and C++ according to object oriented software concepts (Beinhorn and Kolditz (2004a) and Kolditz and Bauer (2003)). The numerical approach is based on the Galerkin finite element method using governing equations given above. Time derivatives are evaluated by a finite difference scheme. The iterative coupling between the discretized flow and transport equations is realized by a Picard iteration scheme, i.e. actual densities of a new iteration step are calculated from the field variables of the previous iteration step. The code has been tested against benchmarks given in (Kolditz et al. (1998)).

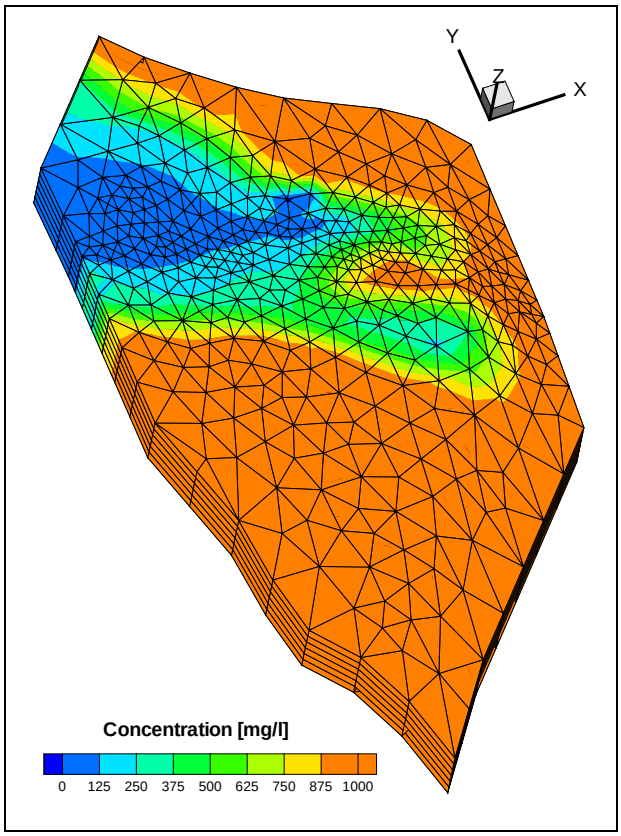

Figure 36: Resulting concentration distribution after 8 years of pumping

Basic modules of GeoSys/ RockFlow are the GeoLib, MshLib, and FEMLib, which can be connected via a Graphical User Interface (GUI). The modules are described below in the context of this application example.

GeoLib

Geometric objects of the GeoLib are points, polylines, surfaces, volumes which form domains. All these geometric entities are implemented as C++ classes: `CGLPoint`, `CGLPolyline`, `CGLSurface`, `CGLVolume`, `CGLDomain`. Instances of these objects can alternatively be stored in vectors and lists for convenience and specific purposes. A detailed description of the implementation of GeoObjects is given in Kalbacher et al. (2003b). As an example Fig. 35 shows geometric information of the hydrogeological system described in previous chapters within the framework of the GUI. The recharge area seen in the GeoSys GUI (Fig. 35) stems from the shape file displayed in Fig. 33. The surface object can now be used to define source/sink terms or boundary conditions. The same is valid for the polylines WADI, BCSOUTH and BCNORTH.

MshLib

The geometric information seen in Fig. 35 also forms the basis for mesh generation. Currently, the following build-in mesh generators can be used: PrisGen (Kalbacher et al. (2003a)), TetMesh (Manabe et al. (2003)) as well as open and commercial systems such as gmsh (2004) and gOcad (2004).

The resulting mesh geometry can be manipulated using mesh operations like the mapping operation. Here a surface object (SFCObj) is being used to relate mesh data to a surface data file such as top or bottom of a hydrostratigraphical unit. An additional operation of the MshLib is vertical mesh refinement. All these operations of the MshLib are controlled via an GUI.

FEMLib

The FEMLib contains independent units necessary to set up and solve the finite element problem. As a result of the numerical approximation method described, two sets of algebraic equations were derived. The general form of these equation is

$$\mathbf{A}_i(t, \mathbf{x}, \mathbf{u}_i, \mathbf{u}_j)\, \mathbf{u}_i = \mathbf{b}_i(t, \mathbf{x}, \mathbf{u}_i, \mathbf{u}_j)$$

where i, j denote different processes, with $\mathbf{A}_i$ system matrix of process i, t time, $\mathbf{x}$ coordinates, $\mathbf{u}_i$ solution vector (primary variable) of process i, $\mathbf{b}_i$ RHS vector of process i. Dependence of process i on process j means coupling, and dependence of system matrix on solution itself means non-linearity.

6.1.9 Results and conclusions

Using the concentration distribution from 1961/63 as initial condition the model was run for the time interval of 8 years using boundary conditions and source/sink terms as described in section 6.1.7. Fig. 36 is showing the resulting concentration distribution after 8 years of pumping. The pattern displayed resembles the measured pattern given in Fig. 31. Hence the numerical model could be used to verify the hydrogeological model to some extent.

6.2 3-D numerical evaluation of density effects on tracer tests

In this section we present numerical simulations that were carried out to assess the importance of density dependent flow on tracer plume development. The model scenario considered in the study is characterized by a short term tracer injection phase into a fully penetrating well and a natural hydraulic gradient. The scenario is thought to be typical for tracer tests conducted in the field. Using a reference case as starting point, different model parameters were changed in order to determine their importance to density effects. Tracer injections of 0.36 kg per m saturated aquifer thickness do not cause significant density effects assuming hydraulic gradients of at least 0.1 percent. Higher tracer input masses, as used for geoelectrical investigations, may lead to buoyancy induced flow in the early phase of a tracer test which in turn impacts further plume development. This also holds true for shallow aquifers. Results of simulations with different tracer injection rates and durations imply that the tracer input scenario has a negligible effect on density flow. Employing model cases with different realizations of a log conductivity random field, it could be shown that small variations of hydraulic conductivity in the vicinity of the tracer injection well have a major control on tracer distribution and may mask effects of buoyancy induced flow.

6.2.1 Introduction

A common approach to characterize aquifers is the use of tracer tests. A non reactive fluid is injected into the ground through a well at a known rate and concentration. The developing plume is then assessed by direct or indirect methods. Direct methods are concentration measurements from water samples taken from down-gradient wells and multilevel piezometers. Indirect methods involve the measurement of changes in electrical conductivity using electrical methods (eg. White (1988), Bevc and Morrison (1991), Morris (1996), Slater et al. (2000), Kemna et al. (2002), Hoffmann and Dietrich (2004)).

The anions (Br^-, Cl^-, F^-) are commonly used as tracers in both cases because of their low material and analytical costs. Tracer concentrations used reach from 0.05 to 20 g/l when using direct methods (Istok and Humphrey (1995)). In the case of electrical methods, a high contrast in electrical conductivity between the tracer plume and the ambient groundwater is required. Concentrations used are much higher and range from 10 to 60 g/l (see Table 5). Clearly the tracer-solution has a higher density than the ambient groundwater. The density variations impact groundwater flow and therefore tracer plume development.

Considerable research on variable-density flow in porous media has been done during the last 30 years. A comprehensive review of the subject and the related issue of benchmarking is given in Diersch and Kolditz (2002) and in the textbooks Nield and Bejan (1999) or Holzbecher (1998) . Oswald and Kinzelbach (2004) designed the most recent three-dimensional physical benchmark experiment to

Table 5: Tracer concentration and masses for electrical investigation methods from literature

Reference	Tracer	Conc. [g/l]	Mass [kg]	Aquifer thickness [kg]	Mass per thickness [kg/m]
Kemna et al. (2002)	Br^-	12	23	10	2.3
Morris (1996)	Cl^-	20	10	6	1.6
Hoffmann and Dietrich (2004)	Cl^-	60	18-36	5	3.6-7.2
White (1988)	Cl^-	20	44	20	2.2
Bevc and Morrison (1991)	Cl^-	35	1460	40	61
Slater et al. (2000)	Cl^-	40	11	3	3.6

test numerical variable-density flow models and Weatherill et al. (2004) suggest several further test cases. Other examples used as benchmarks to test numerical models are given in Diersch (2002). The subject of variable-density flow in heterogeneous porous media is addressed in Simmons et al. (2001).

Experimental investigations performed to assess the importance of density contrasts on plume development were conducted by different authors: Paschke and Hoopes (1984), Schincariol and Schwartz (1990), Oostrom et al. (1992), Istok and Humphrey (1995), Jalbert et al. (2000) and Wood et al. (2004). The experiments prove density effects even at small density differences. For example the flow container experiments of Schincariol and Schwartz (1990) have shown that tracer concentration of 1 g/l NaCl can produce gravitational instability at realistic groundwater velocities.

Real world scenarios where density effects are thought to have an influence on mass migration include contaminant plumes under landfill sites (Kimmel and Braids (1980), MacFarlane et al. (1983)) and a large scale tracer test conducted at Cape Cod (LeBlanc et al. (1991)). Both scenarios have been investigated with numerical methods: The study by Zhang et al. (1998) is related to that particular tracer test at Cape Cod and Dorgarten and Tsang (1990) could demonstrate a strong influence of density effects on movement of liquid waste in a deep sloping aquifer. Koch and Zang (1992) provided a numerical study of the effects of variable density on contaminant plume migration in general. The plumes considered in their study are generated from impoundments. Time scales considered range from 3 to 15 years.

In contrast to scenarios examined by Koch and Zang (1992) and the experimental investigations mentioned above, tracer tests considered here are characterized by a short term input phase. As concentrations decrease rapidly in that case, buoyancy induced flow due to density differences is expected to take place only near the source term. The objective of this study is to numerically evaluate density effects on tracer plume development during a typical tracer test scenario.

6.2.2 Numerical model

The numerical model used for the simulations is the FE Simulater GeoSys/ RockFlow (Kolditz et al. (2003)) which is programmed in C and C++ according to object oriented software concepts (Kolditz and Bauer (2004)). The numerical approach is based on the Galerkin finite element method using the governing equations given above. Time derivatives are evaluated by a finite difference scheme. The iterative coupling between the discretized flow and transport equations is realized by a Picard iteration scheme, i.e. actual densities of a new iteration step are calculated from the field variables of the previous iteration step. Details of the numerical procedure are given in Diersch and Kolditz (2002). The code has been tested against the classical seawater intrusion problem of Henry, the free convection problem by Elder and the salt dome problem (Kolditz et al. (1998)).

6.2.3 Model dimensionality

Two-dimensional simulations involve the assumption of an infinitely extending source width. This assumption does not hold true to a given tracer input into a well. Fluid flow and dispersion acting in the y-direction during the injection phase is expected to reduce concentrations and should therefore be considered in the modelling study. Zhang et al. (1998) studied the issue of dimensionality by comparing modelling results of three dimensional models using different source width. They could show that despite the increased dilution due to the additional dispersion, the rate of downward movement increased as the width of the source in the y-direction decreased. This effect is attributed to the upward resistance of the ambient water to plume sinking. The resistance on a narrower plume is smaller than the resistance on a wider plume. In order to take these effects into account, all modelling results are based on three-dimensional models.

6.2.4 Theoretical considerations

Assuming constant concentration for a tracer plume the trajectories of the plume center point can be estimated using Darcys law (equation 2) determining a x- and z-component of the flow trajectory (q_x, q_z). The slope of the trajectories is a measure of the density effects and in this simplified case depends on density contrast between the density of the fluid and the density of water $\rho - \rho^w$ controlling q_z, on the head gradient ∇h controlling q_x and on the anisotropy K_x/K_z controlling the ratio q_x/q_z.

If a slug of tracer fluid is instantaneously injected over the full thickness of a two-dimensional flow field, the concentration at point (x, y), at time t after injection is

$$C(x,y,t) = \frac{C_0 A}{4\pi t(\alpha_L \alpha_T)^{1/2}} exp\left[-\frac{(x-(x_0-v_x t))^2}{4\alpha_L t} - \frac{(y-y_0)^2}{4\alpha_T t}\right] \quad (89)$$

where C_0 is the concentration of the tracer at t_0 and A is the area covered (Fetter (1992)). For the scenario described below concentrations at the center of the plume are reduced by a factor 10 after 6 days already. Density dependent flow is therefore expected to take place predominantly in the first few days after tracer input. If however the tracer injection phase lasts longer, the density flow phase is prolonged as well. These considerations lead to parameters to be varied in the numerical study: tracer injection rate, duration of tracer injection, aquifer geometry and aquifer properties. Effects of parameter variations are assessed by comparing resulting concentration distributions with those from the reference case described below.

6.2.5 Model setup, reference case

The model domain of 50x20x10 m is discretized with a mesh containing 25,000 hexahedral elements. The grid size ranges from 0,3 m in the vicinity of the well to 2 m at the model boundaries. A uniform flow field is induced by a gradient of 0.1 percent defined by fixed constant head boundary conditions at both faces of the model during the complete simulation time. The injection well is positioned at a distance of 5 m from the left hand side boundary at the center of the y-extension. It is screened over the full thickness of the aquifer. A tracer mass of 3.6 kg is introduced at equal parts over the screened length of the well for one hour. An injection of a tracer solution is not considered. Related to the aquifer thickness, the value of 0.36 kg per m saturated aquifer thickness is less than the tracer masses quoted from literature summarized in Table 5. Due to the freshwater inflow at the left hand side boundary, the concentration there is kept at zero. At all other faces we defined Neumann conditions with respect to the mass transport problem so that tracer may leave the domain at the right hand side constant head boundary by dispersive and advective fluxes. Model geometry, discretization and boundary conditions are displayed in Fig. 37. Hydraulic conductivity of the aquifer is set to $K_x = K_y = K_z = 10^{-3}$ m/s, the porosity to $n = 0.1$. The resulting tracer velocity is $v = 0.864$ m/d. Longitudinal and transversal dispersitvities α_L and α_T are 1 m and 0.1 m respectively. The effective diffusion coefficient D_e is set to 10^{-10} m^2/s. Tracer plume development has been calculated for the first 40 days upon tracer input.

Underlying assumptions of the numerical model are: 1. A circulating pump moves water around in the well during the input phase so that no density stratification is taking place during the input phase. 2. The tracer is not actually injected at high pressure as would be the case in a packed well system, but enters the system by a relative low head gradient, so that only the tracer mass needs be considered.

Modelling results of the reference case t6 are displayed in a three-dimensional mode for demonstration purposes (Fig. 38). The figure shows the 0.025 g/l concentration isosurfaces at times t = 1 h, 17 d and 40 d and concentration contours of a section along the xz-plane at the center of the tracer plume (y =

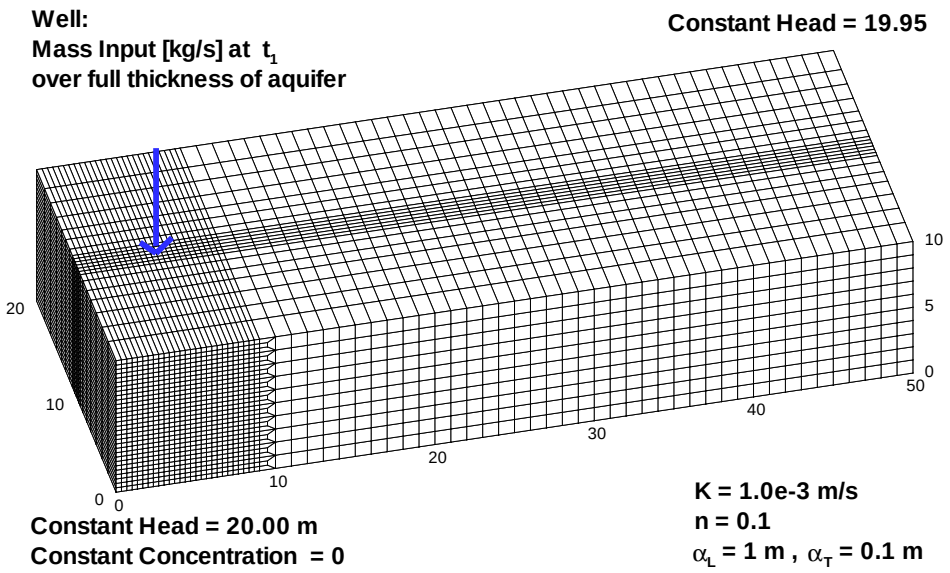

Figure 37: Model dimensions, discretization and boundary conditions

10 and t = 17 d). The plume is clearly showing the tendency to creep along the bottom of the aquifer. The same results were obtained using a vertical grid resolution of 0.1 m in the vicinity of the well so that the chosen grid size was considered sufficiently fine.

6.2.6 Model variations and results

Now using the reference case as a starting point different model parameters were changed in order to assess their importance to density effects. Model cases considered in this study are shown in Table 6 along with a summary of parameters changed. The model cases are organized in 4 different groups according to the parameter that is being varied. A detailed description of model cases and their results is given in the following section.

Visualization of the three-dimensional model results in two-dimensional plots makes the comparison of the different data sets easier. Results of each of the

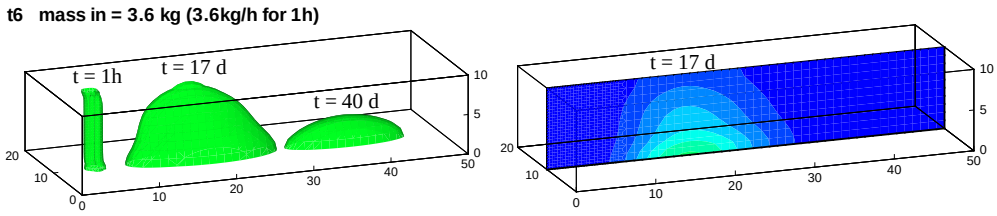

Figure 38: Results of the reference case t6: a: Concentration isosurfaces with 0.025 g/l at t = 1h ,17d and 40d; b: Concentration contours at xz-plane at t = 17d

Table 6: Summary of model cases and description of parameter variations

Group Name	Parameter varied	Case Name	Description of parameter variation
group 1	Tracer input rate	t8	mass in = 3.6 kg (3.6 kg/h for 1h)
		t6	mass in = 36 kg (36 kg/h for 1h)
		t7	mass in = 72 kg (72 kg/h for 1h)
		t4	mass in = 180 kg (180 kg/h for 1h)
group 2	Tracer input rate and duration	t6vt	mass in = 36 kg (3.6 kg/h for 10h)
		t6vt2	mass in = 36 kg (0.72 kg/h for 50h)
group 3	Geometry, Properties	t6va	anisotropy $K_x/K_z = 5$
		t6vg	half hydraulic gradient $\nabla h = 0.05$
		t6vz	half aquifer thickness z = 5 m
		t6vl1	low K layer with K = 1e-4 m/s
group 4	Heterogeneous K Field	s1a	realization1
		s1b	realization2
		s1c	realization3

model cases are shown as concentration contours of a cross section along the xz-plane at the center of the tracer plume (y = 10). Displayed is the plume development at the near source and far source region.

6.2.7 Model cases group 1 (Tracer injection rate)

In the first group of model cases the mass of the tracer input is varied by changing the rate of tracer injection whereas the duration of tracer injection is 1 hour for those 4 model cases. Tracer input rates are 0.36, 3.6, 7.2 and 18 kg/h. The objective of these variations is to assess the degree to which buoyancy induced flow has an impact on concentration distributions.

Fig. 39 shows the results of the first set of model variations in the order of increasing tracer injection rates. Maximum concentrations shown for model case t8 have decreased to of 0.011 g/l after 9 days upon tracer input. The cross sections show almost vertical contour lines at early and late times, i.e. there is little variation of concentration along the z-axis. Density effects are negligible during the complete simulation time. Changes in concentration along the z-axis become more pronounced for the following three cases. For model case t6 concentrations at the bottom are with ca. 0.16 g/l four times as high as concentrations at top after 9 days upon tracer input. The relationship of these values further increases from 6.6 for case t7 to 9 for t4, and stays almost constant during further plume development. Hence the figures reveal an approximately proportional increase of concentration variations along the z-axis with increasing tracer masses and confirm that density flow takes place predominantly in the early phase of plume development. The movement of the plume centroid shown in Fig. 40 also confirms the importance of the early phase of plume development. In order to estimate the vertical displacement as a function of the tracer mass introduced maximum displacements are plotted versus tracer mass in Fig. 41. The resulting curve shows an exponential behavior: For lower tracer masses the

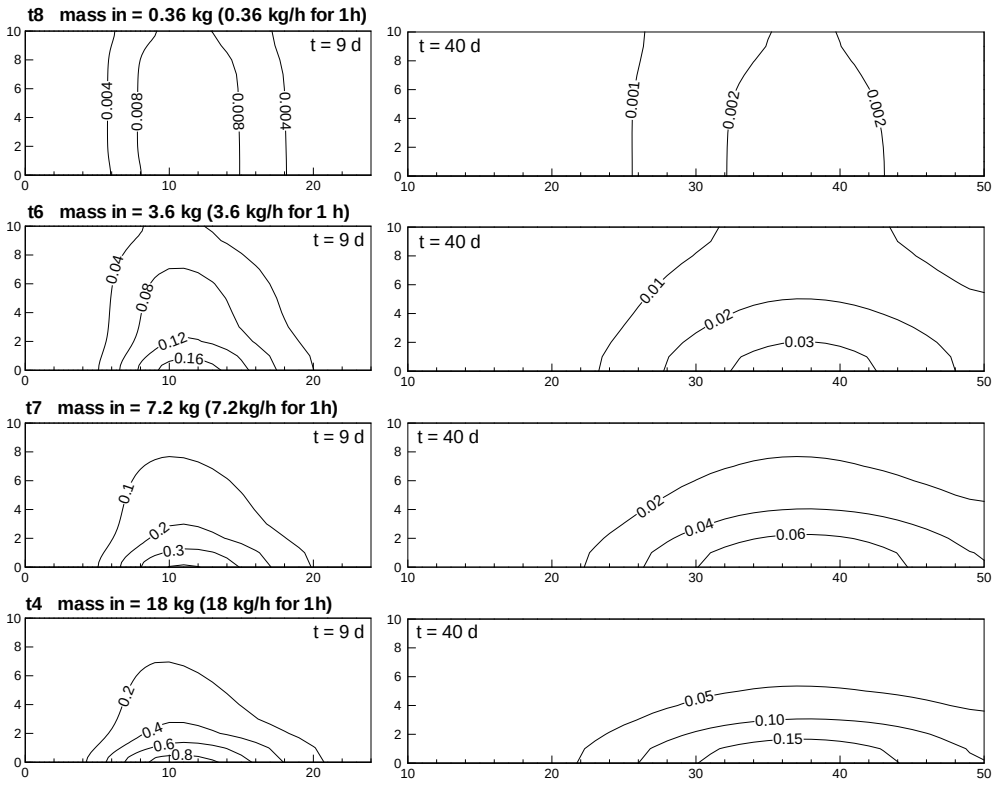

Figure 39: Concentration contours for increasing source masses (group 1), concentrations in g/l

curve shows a steep increase of downward movement with increasing masses. For higher masses the curve flattens out and tends asymptotically towards a maximum value. The flattening out is attributed to the aquifer bottom which clearly puts a constrain on the vertical displacement of the tracer plume.

6.2.8 Model cases group 2 (Tracer injection duration)

It is current practice to use highly concentrated tracers for a short tracer injection interval when the tracer plume is assessed with geoelectrical methods. As density effects take place especially in the early phase of tracer injection, the question of an improved tracer injection scheme arises: Is it possible to minimize density effects and still provide high concentration contrasts needed for a geoelectrical investigation? The model cases of group 2 are designed to address that question. Parameters changed are tracer injection rates and duration of tracer input. Results of 2 different model cases are presented in Fig. 42. For model case t6vt the duration of tracer input is 10 hours at an input rate of 0.36 kg/h. The mass input of 3.6 kg corresponds to the mass input of reference case t6. Results are therefore compared to those given for model case t6. The different input rates produce similar concentration distributions, i.e. we see the same density effects compared to the more rapid mass input of case t6. A similar example is

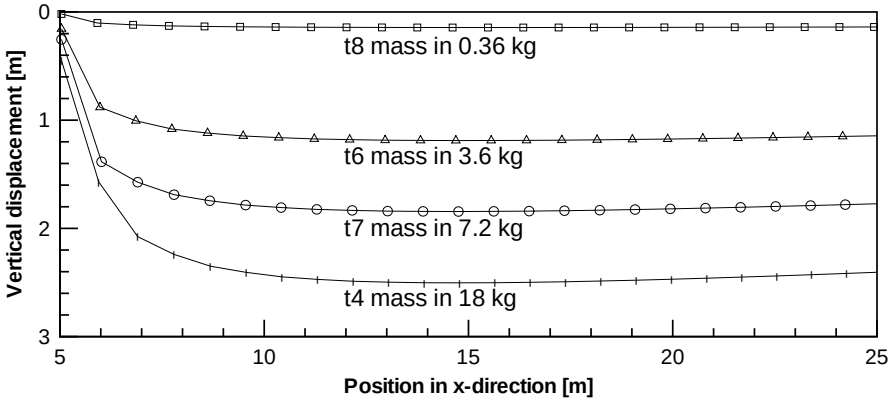

Figure 40: Movement of center of tracer mass (Model cases group 1)

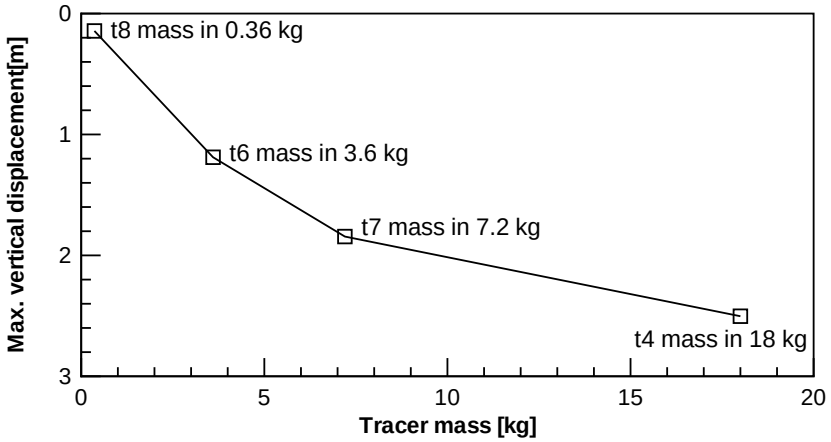

Figure 41: Maximum vertical displacement versus tracer mass (Model cases group 1)

shown to verify that result. Duration of tracer input is set to 50 hours at an input rate of 0.072 kg/h in model case t6vt2. Total mass input is again 3.6 kg corresponding to case t6. Again we see a almost identical shape of the contour lines compared to case t6. Only the maximum concentrations at the bottom of the plume has decreased slightly i.e. a negligibly small advantage is gained with respect to minimizing density effects.

6.2.9 Model cases group 3 (Geometry, properties and boundary conditions)

In a third set of calculations different parameters are varied. Variations concern aquifer properties, boundary conditions and aquifer geometry. The objective of these variations is to assess in how far certain scenarios enhance or hinder buoyancy-induced flow. The model cases chosen are described below along with

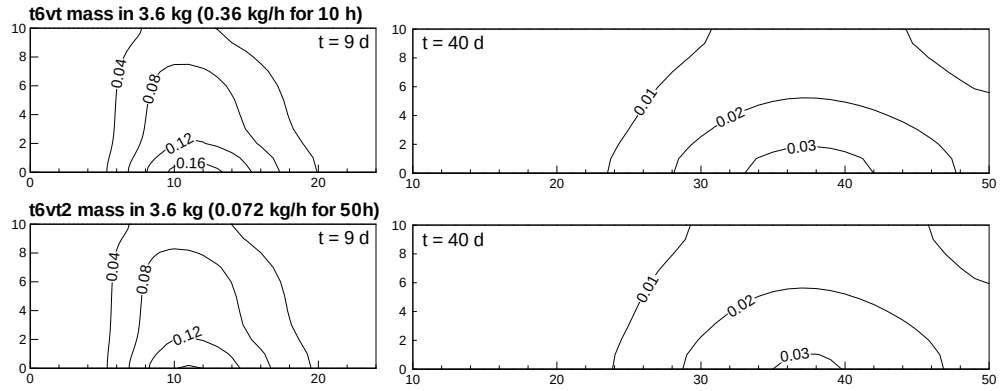

Figure 42: Concentration contours for different tracer input schemes (group 2), concentrations in g/l

a description of observed modelling results. Concentration contours and movements of center of mass are displayed in Fig. 43 and Fig. 44 respectively.

t6va The vertical conductivity K_z is changed to 2 x 10^{-4} m/s leading to an anisotropy ratio K_x / $K_z = 5$. As expected anisotropy reduces the density effects as the contour lines of case t6va5 are steeper compared to case t6. Also the center of mass shows a maximum vertical displacement of only ca. 0.3 m as compared to the displacement of ca. 1.20 m in the reference case.

t6vg The head gradient is reduced from 0.1 percent to 0.05 percent. Resulting concentration contours are similar to those of the reference case t6, only slightly flatter. The impact of reducing the head gradient is more obvious when comparing positions of center of mass for both cases.

t6vz Aquifer thickness is reduced from 10 m to 5 m. In order to produce comparable results with respect to the reference case t6, the tracer injection rate is reduced to 1.8 kg/h. Compared to t6 these variations lead to similar concentrations at top and bottom of the aquifer. Considering the reduced aquifer thickness the gradient of changes in concentration along the vertical axis has increased. The effect is due to the earlier resistance for vertical tracer movement, as compared to thicker aquifers. Examining the movement of the mass center the influence of the aquifer bottom becomes more obvious as the maximum displacement in the case of the reduced aquifer thickness is smaller than for the reference case.

A striking feature that is not readily made by visual examination of concentration contours is that after a short phase of downward movement, the gravity center is moving upwards again. Among possible reasons for that are diffusive and dispersive fluxes but also advection with a vertical component that is caused by the development of local convection phenomena,

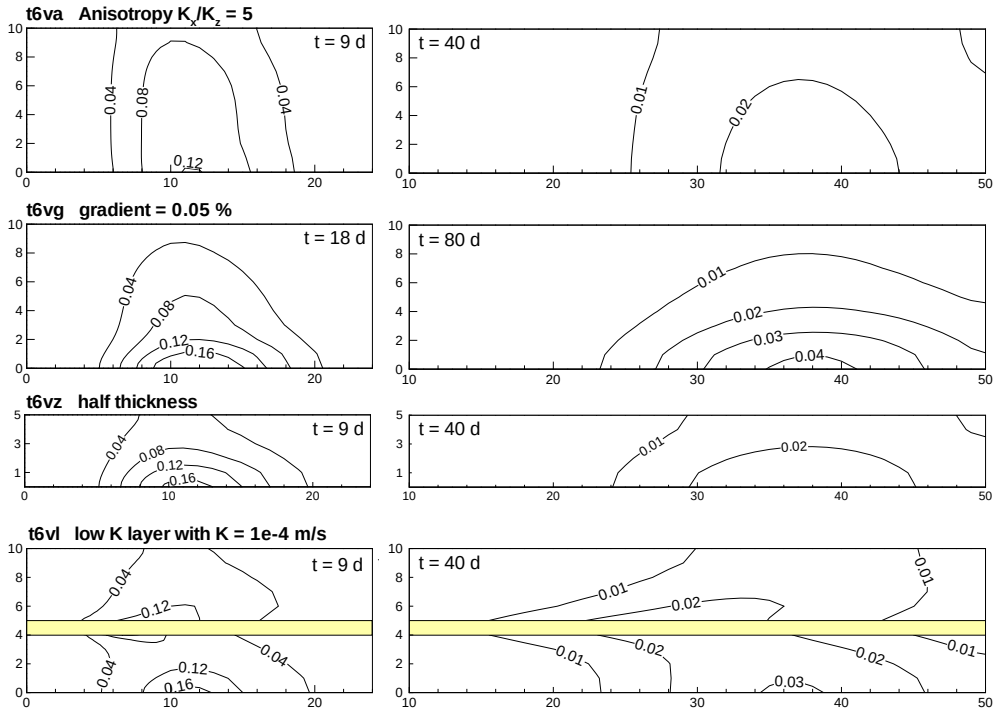

Figure 43: Concentration contours for different geometries and properties (group 3), concentrations in g/l

i.e. downward movement of water at the plume center must cause upward movement in other regions due to the law of mass conservation.

t6vl A layer with a reduced conductivity of $K_x = K_y = K_z = 10^{-4}$ m/s is introduced at an elevation of 4 to 5 meters. The concentration contour plot in Fig. 43 reveals the development of a two layer system with two asymmetric tracer plumes. Each layer shows increased changes in concentration along the vertical axis, similar to the case with reduced thickness. As tracer transport velocities are smaller in the inserted extra layer, concentration contours show some distortion towards the injection well in the vicinity of that layer. This is leading to an inversion of concentration gradients along the z-axis in front of the plume center in the upper aquifer and behind the plume center in the lower aquifer, i.e. the effects we would expect from buoyancy induced flow are masked at these locations. Total concentrations in the upper part aquifer have increased as seen in the upward shift of the 0.02 g/l concentration contour for 1 m compared to the reference case. Accordingly, concentrations in the lower part have decreased. Hence, the low conductivity layer hinders mass to sink from the upper part to the lower aquifer and reduces density effects.

These features also show in the movement of gravity centers: The maximum vertical displacement of the complete tracer plume (see line t6vl1 in Fig. 44) is reduced from ca. 1.20 m in the case without an intermediate

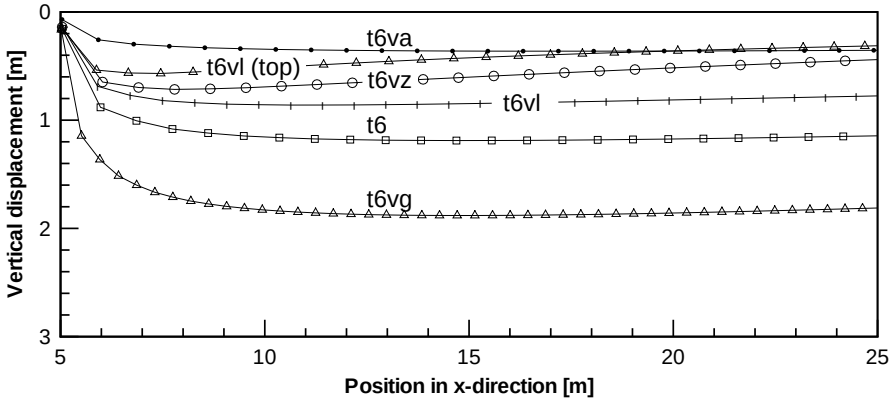

Figure 44: Movement of center of tracer mass (Model cases group 3)

layer to ca. 0.90 m for the case t6. Looking at the tracer plume centroids of the top 5 meters of the aquifer separately shown in line t6vl1(top) in the same figure, we see a similar development as seen in the case of reduced aquifer thickness. Only the maximum vertical displacement is smaller. Interestingly, again we see a slow upward movement of the center of mass.

6.2.10 Model cases group 4 (Heterogeneous conductivity fields)

The presence of heterogeneities in hydraulic conductivity creates variations in flow velocities. In order to assess if the effects of density induced flow are masked by these variations three model cases in which the conductivity distribution is regarded as heterogeneous random field are presented.

We chose a lognormal conductivity distribution $y = ln(K)$, a variance of σ_y^2 = 0.5 and a median conductivity of 10^{-3} m/s. This corresponds to a mildly heterogeneous aquifer with conductivities ranging from 5 x 10^{-4} m/s to 4 x 10^{-3} m/s. Spatial variation is represented by an exponential semivariogram with an integral scale of 3.3 m in the x- and y-direction and 0.6 m in the z-direction in order to mimic horizontal stratification. For small variances ($\sigma_y^2 < 1$) effective conductivities K^{eff} can be calculated after a formula given in Dagan (1989). Effective conductivity are $K_x^{eff} = K_y^{eff}$ = 1.2 x 10^{-3} m/s for the x and y-direction and K_z^{eff} = 8.2 x 10^{-4} m/s for the z-direction. Hence we have a system that compares well with the homogeneous medium given in reference case t6.

The conductivity fields were generated with Gstat, a program for geostatistical modelling, prediction and simulation described in Pebesma and Wesseling (1998). Three different three-dimensional conductivity distributions for the parameter set given above are used for the flow and transport simulations. Exemplary two-dimensional sections of the conductivity fields are displayed in Fig. 45. Note the lenses of low permeability (dark color) in the vicinity of the injection well marked with the bold line at x = 5 m. In order to generate large density effects a tracer

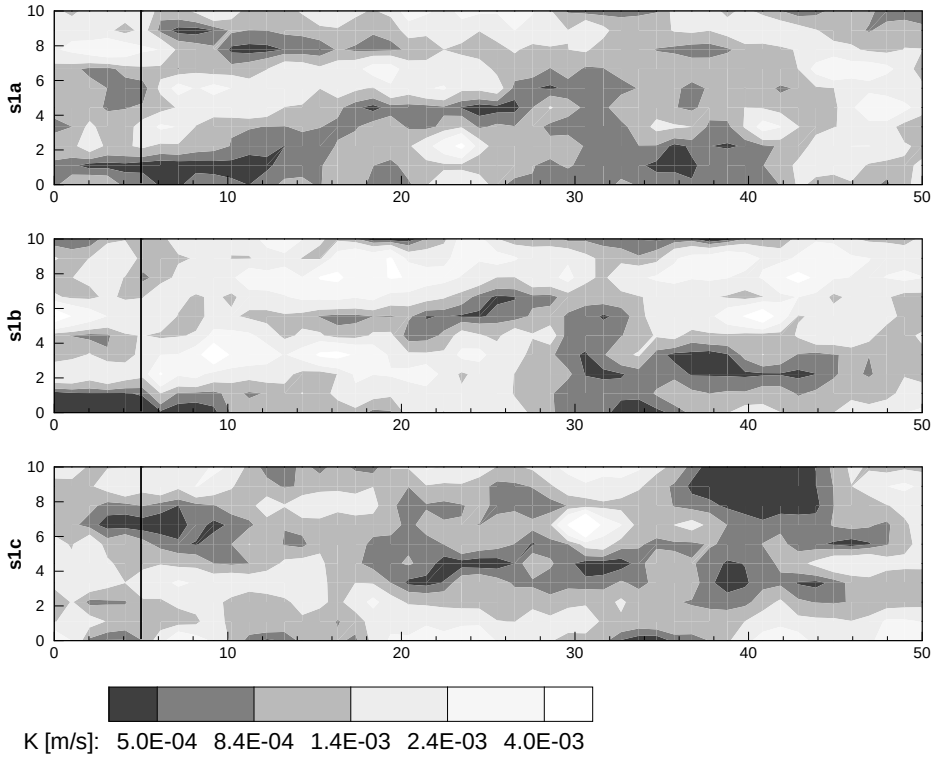

Figure 45: Two-dimensional sections of three log conductivity random fields

mass input of 18 kg is chosen. Hence the results are compared to those in model case t4. All other model parameters are the same as those given in reference case t6. Again concentration contours of a section along the xz-plane at the center of the tracer plume are shown (Fig. 46).

Concentration contours calculated with conductivity distributions s1a and s1b show higher concentrations at the bottom than at top of the aquifer. This is valid for the near source as well as the far source region. However, in the case of s1c higher concentrations are observed in the upper part in the near source region and to a lesser extent in the far source region. Obviously the low conductivity area in the upper part of the aquifer in the vicinity of the well (Fig. 45) is the reason for the observed concentration distribution. Tracer mass is introduced into low conductivity areas during the injection phase. During the following natural gradient conditions velocity of tracer transport decreases and tracer mass is released with a time lapse into higher conductivity areas. In the first two cases, low conductivity areas are located in the lower part of the aquifer so that a retarded tracer transport leads to higher concentrations at later times in the lower part.

Movements of centers of mass are shown for the model variations with heterogeneous conductivity fields as well as for the case with a homogeneous conductivity field in Fig. 47. In general all curves show a steep downward movement and reach a vertical displacement of at least 3 m. The biggest vertical displacement

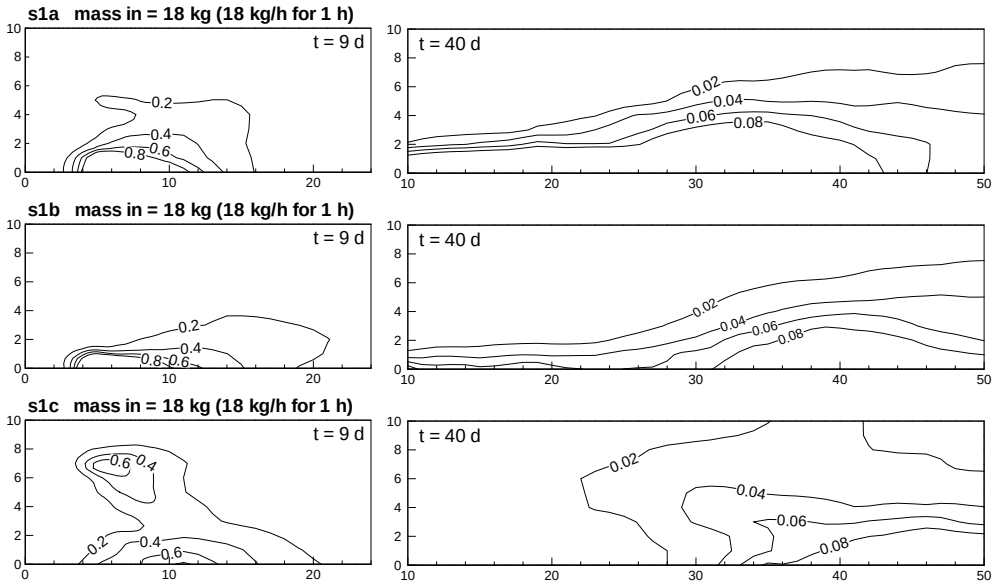

Figure 46: Concentration contours for different conductivity distributions (group 4), concentrations in g/l

is seen for the homogeneous conductivity field and the other pathlines plot only slightly above the reference case.

From both the concentration contours and the first moment analysis, it can be concluded that variations in flow velocities due to heterogeneities may account for variations in the local concentration distribution but do not mask effects of density dependent flow.

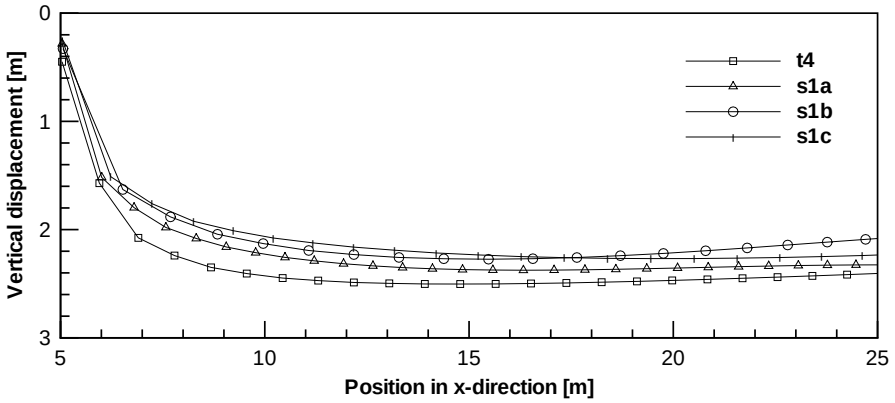

Figure 47: Movement of center of tracer mass (Model cases group 4)

7 Summary and conclusions

Numerical simulations were carried out to assess the importance of density dependent flow on tracer plume development. The model scenario is characterized by a short term tracer injection phase into a fully penetrating well and a natural hydraulic gradient. The scenario is thought to be typical for tracer tests conducted in the field. Modelling results were interpreted using concentration contours and a first moment analysis. The results of the study are summarized below:

1. In the scenario considered tracer injections of 0.036 kg per m saturated aquifer thickness did not cause significant density effects in a flow field with a hydraulic gradient of at least 0.1 percent. Results of model cases using higher tracer injection masses did show that buoyancy induced flow takes place in the early phase of the tracer test, which in turn impacts further plume development. In these cases the concentration distributions were significantly altered by density effects at early and late times. This also holds true for shallow aquifers.

2. For a realistic tracer test scenario and an injection of 1.8 kg per m saturated aquifer thickness the center of tracer mass may sink for more than 2.5 m. Where the aquifer bottom does not put constrains on the downward movement of the mass center the vertical displacement appears to increase approximately proportional to the tracer mass introduced. For the given scenario however, the aquifer bottom hinders downward movement and the relationship of the vertical displacement and mass can best be described with an exponential function.

3. Simulations using different tracer injection rates and durations have shown that the tracer input scenario has a negligible effect on density induced flow.

4. A thin intermediate layer with reduced conductivity of an order of magnitude reduces vertical mass exchange between two layers. Within each layer density dependent flow takes place and produces similar concentration distributions as in the case of a shallow aquifer. These density effects are partly masked at local scale due to reduction of horizontal flow velocities.

5. Employing model cases with different realizations of a log conductivity random field, it could be shown that small variations of hydraulic conductivity in the vicinity of the tracer injection well have a major control on the local concentration distribution but do not mask effects of buoyancy induced flow.

Based on the limited number of model runs performed and shown in this paper the following general conclusions can be drawn from the results:

For systems with relatively high hydraulic gradients of at least 0.1 percent, density effects do not have an significant effect on the tracer plume development for low tracer injection masses due to the rapid dilution of the tracer solution in combination with high horizontal flow velocities. In cases were higher tracer masses are introduced, care must be taken to account for density effects despite high hydraulic gradients. Even in shallow aquifers where plume sinking is naturally limited, the concentration distribution is altered significantly by density differences. This is also the case in heterogeneous aquifers. The threshold of tracer masses at which density dependent flow may show significant effects for a given hydraulic gradient of 0.1 percent is estimated to be approximately 0.03 g/l per m saturated aquifer thickness. A prolonged tracer input duration does not reduce density effects significantly. Hence the increased logistical workload necessary for a long tracer input is not justified.

As a wide range of parameters influence density driven flow and there are an endless number of combinations it is beyond the scope of this paper to derive further general guidelines. Additional numerical modelling in combination with laboratory or field experiments could help to define critical parameter combinations for which density dependent flow significantly alters expected concentration distributions. Particularly interesting would be to further examine effects of different aquifer geometries and thicknesses in order to establish when convection phenomena can cause a redistribution of mass as seen in the case of a shallow aquifer examined here. In the meanwhile, if in doubt, a modelling study can help to decide if density effects need to be considered when interpreting a particular tracer test.

7.1 Groundwater flow and transport model of the Zarqa Ma'in-Jiza area, Central Jordan

7.1.1 Introduction

In this section a model for coupled groundwater and river flow is presented which is developed based on object-oriented programming concepts. The groundwater model is fully three-dimensional and accounts for confined as well as unconfined flow. Additionally density effects resulting from salinity and heat variations can be taken into consideration. The river model is based on averaged one-dimensional shallow water equation. The coupling between the two hydraulic systems can be treated in two different ways. First, in the framework of finite element technology, the groundwater body (represented by three-dimensional prismatic elements for aquifers/aquitards and two-dimensional quad elements for faults) and the river stream (represented by one-dimensional line elements) are coupled directly, i.e. having common mesh nodes. Second, groundwater and river systems can be coupled in the framework of the multi-continuum concept, i.e. each hydraulic system is represented by an individual continuum, which are coupled via transfer functions. The second approach has advantages concerning numerical stability, but transfer functions must be given for water exchange between both compartments, which are difficult to obtain experimentally. Here the direct coupling concept is presented. The groundwater-river model is based on data from the Jordan Valley area. The focus of this application example is the technical background for coupled hydrosystem modelling, such as data import, consistent geometric modelling, meshing of heterogeneous systems, object-orientation for coupled processes and user interfaces.

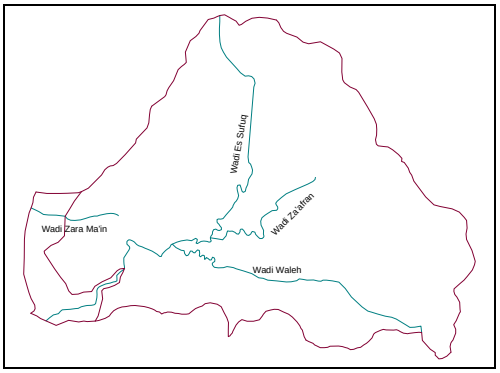

Figure 48: Main wadis in the Zarqa Ma'in-Jiza area

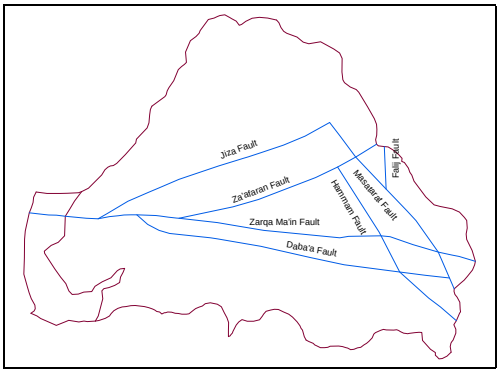

Figure 49: Main faults in the Zarqa Ma'in-Jiza area

The governing equations and the numerical approach are presented in sections 2 and 3 respectively.

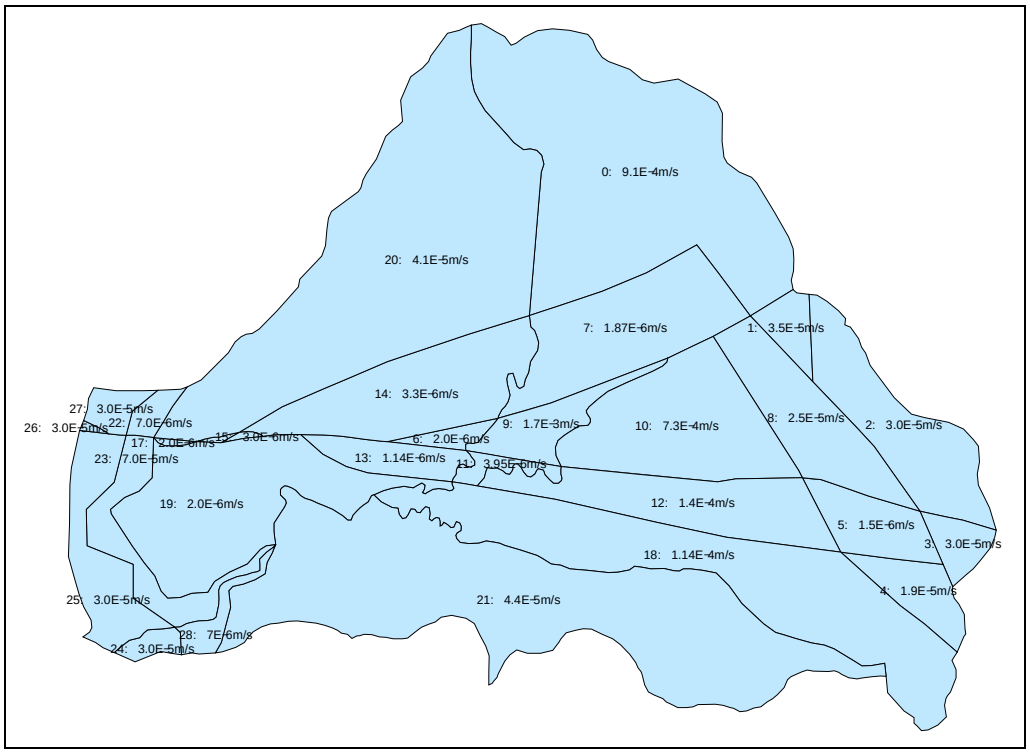

Figure 50: Hydraulic conductivities in the Zarqa Ma'in-Jiza area

7.1.2 Data base

The surface system is characterized by a complex topography formed by several Wadis, see Fig. 48. The subsurface system of the investigation area consists of two major aquifers which are separated by an aquiclude but connected by a fault network, as displayed in Fig. 49. Based on a large number of well observations (more than 100 boreholes) the hydraulic conductivity distribution is estimated according to Fig. 50. Most of the available information such as topography and geology, hydrogeological parameters, well positions and pumping rates, wadis and springs, fault system, water levels and boundary conditions is available in a GIS project (Sawarieh et al. (2004)). GIS data can be directly imported into GeoSys (Chen et al. (2004)). The data base for this exemplary application for the Jordan Valley area was provided by Sawarieh et al. (2004).

7.1.3 Geometrical model

The three-dimensional structural model is established based on available geometric data. The geometric model consists of polylines (for wadis), plane surfaces (for faults), curved surfaces (for surface and aquifer topography as well as boundary conditions) and volumes (for the aquifer-aquitard-aquifer system). Fig. 52 displays all volumes (three-dimensional structures) and Fig. 53 highlights the embedded wadis and faults as well as surface topography (one-dimensional and

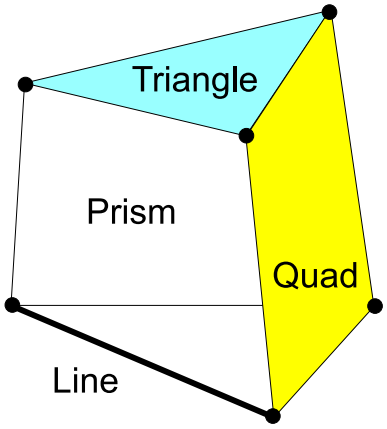

Figure 51: Combination of multi-dimensional finite elements

two-dimensional structures). Consistency of the geometric model is very important, in particular, for the meshing procedure. The spatial discretization (finite elements and differences) is assembled from coupled line (for wadis), triangular (for surface), quad (for faults) and prismatic (for aquifers) elements as summarized in Fig. 51.

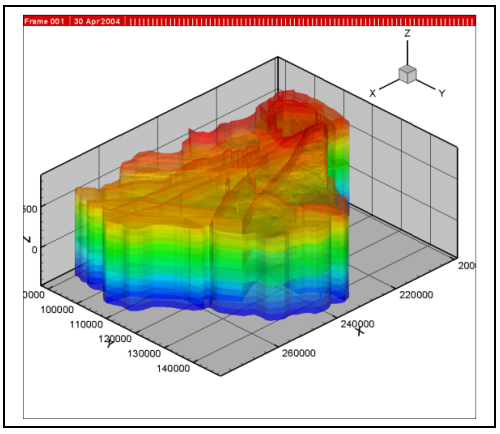

Figure 52: Three dimensional geometric model showing layering and faults

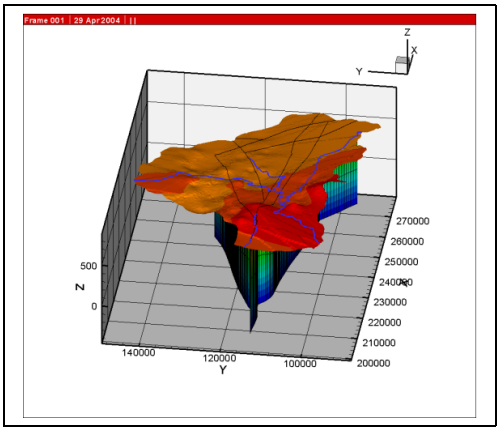

Figure 53: Three dimensional showing rivers, fault traces and the surface topography

7.1.4 Examples

We consider two examples. The first one is a very simple test case to check the integrity of the river flow model without coupling to the groundwater flow system. The second one is based on data from the central Jordan Valley area. Here first preliminary results are presented to show coupling effects between the surface / subsurface water compartments.

A simple test case is examined to test the river model separately. Figure 54

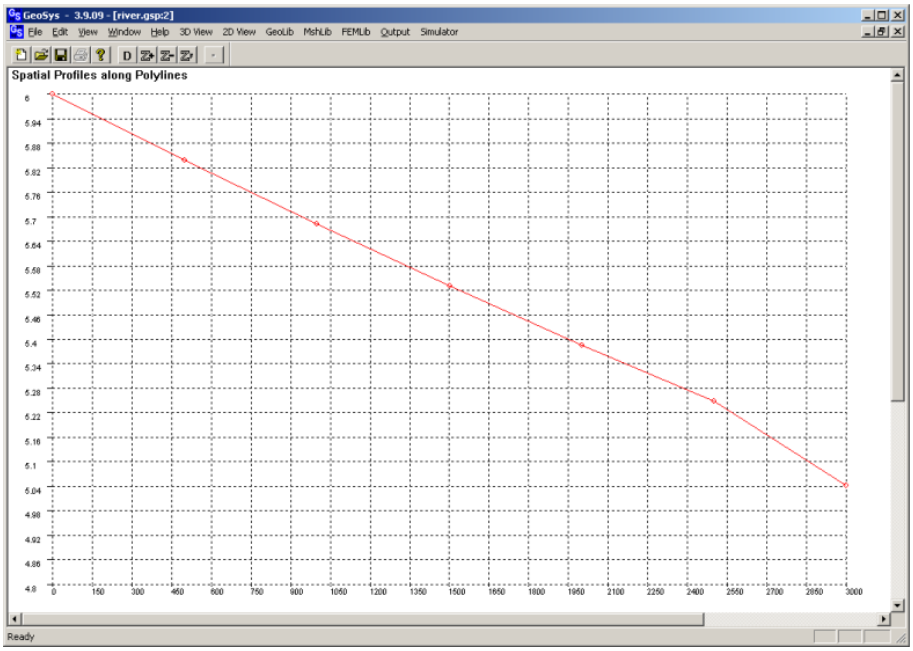

Figure 54: Water level along the river

displays the water depth along the river line for steady flow and constant discharge (Q=const). The boundary condition at left side (s=0) for water depth is h=6m.

Figures 55 and 56 show the hydraulic head distribution in the upper and lower aquifers, respectively. In the upper aquifer near the surface the influence of the Wadis can be clearly seen. They act as water divides. In the lower aquifer hydrostatic conditions dominate but influences of the fractures can be observed.

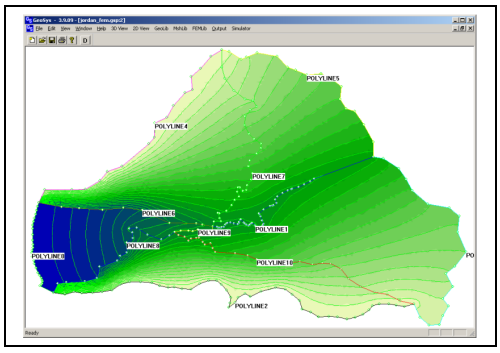

Figure 55: Hydraulic head in the upper aquifer

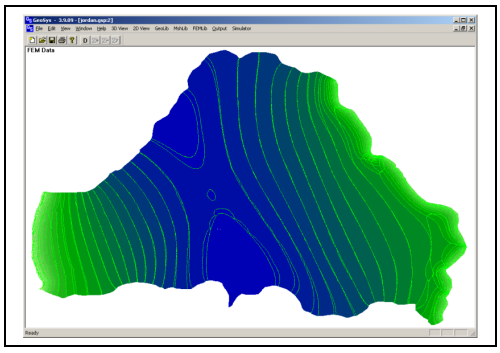

Figure 56: Hydraulic head in the lower aquifer

Fig. 58 illustrates the three-dimensional head distribution looked from west. The evidence of fracture influences can be detected. It is important to notice that the presented results are preliminary. Results of the modelling efforts will be presented elsewhere upon completion of the study. The intention of this paper is to give an overview of required methods and tools to develop models for holistic hydrosystem analysis.

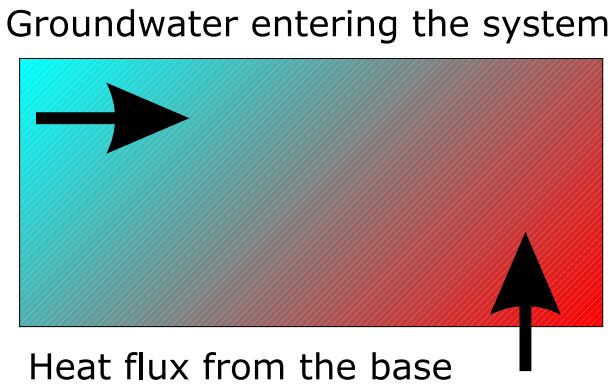

Figure 57: Geothermal basic process in the area

7.1.5 Geothermal processes

The thermal basic processes are illustrated in figure 57. There is a permanent heat flow from the base to the system. Through the North groundwater is entering the upper aquifer and through the East the lower aquifer. This groundwater has to cool the whole system; otherwise the temperature will increase permanently.

Figure 59 shows a first long-term simulation (30000 years) of the thermal system based on the hydraulic model presented above. The simulation shows a permanent increase of temperatures. The groundwater entering the system is not equilibrating the base heat flux. This indicates to possible defects in the current model. First, the outside groundwater recharge to the domain is underestimated. Second, the base heat flux is overestimated. This means, involving thermal data to the simulation, the hydraulic model can be improved.

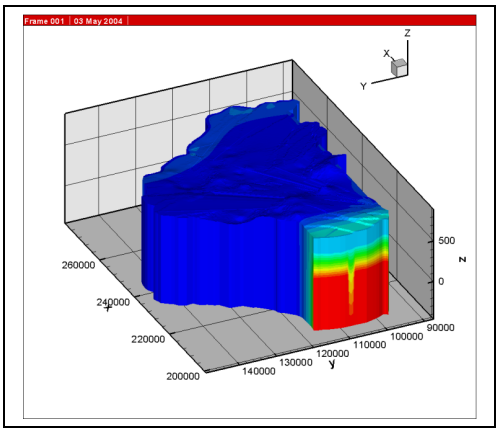

Figure 58: Hydraulic head from west, influence of the fault system

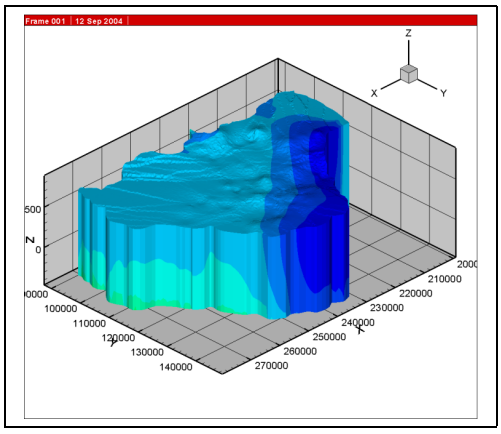

Figure 59: Temperature distribution in the model area

8 Summary and conclusions

The work done and presented in the thesis aims at providing the prerequisits needed to develop a software package to simulate hydrologic systems including groundwater and surface water processes. A new element type was implemented with two options for the evaluation of element matrices, i.e. a numerical integration and a analytical method. The analytical integration proves to be faster than the numerical method and thus provides an advantage especially for the simulation of nonlinear systems, where element matrices have to be calculated in every iteration. With the implementation of a moving mesh method a robust method for the calculation of unconfined groundwater flow has been implemented. Lastly, the new overland flow component forms an essential step towards developing a physically based, spatially distributed modelling tool. In combination with already existing program components now all relevant processes on the land phase as illustrated in Fig. 60 can be modelled.

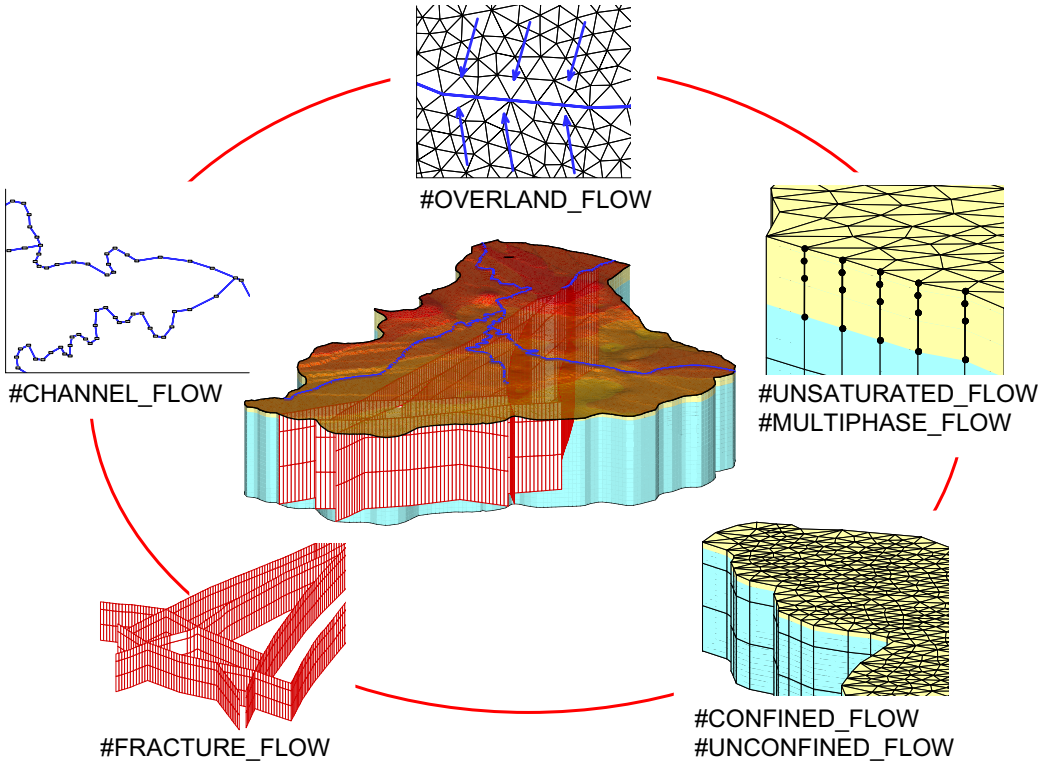

Figure 60: Integrated hydrosystem modelling

Now, the most important steps toward a integrated modelling concept concern the coupling of the different processes shown. Interaction of the following processes are possible

`#CHANNEL_FLOW` $\leftrightarrow$ `#UNSATURATED_FLOW`

#CHANNEL_FLOW	↔	#UNCONFINED_FLOW
#OVERLAND_FLOW	↔	#CHANNEL_FLOW
#OVERLAND_FLOW	↔	#UNSATURATED_FLOW
#UNSATURATED_FLOW	↔	#CONFINED_FLOW / UNCONFINED_FLOW

Closed form analytical solutions do not exist for most of these coupled processes. Validation of new program components is than best achieved using comprehensive field data or controlled laboratory experiments. With respect to coupling overland flow with unsaturated flow laboratory experiments are presented in literature Smith and Woolhiser (1971), Govindaraju and Kavvas (1991) and Fiedler and Ramirez (2000). Another form of model testing is to crosscheck results from different numerical codes using a variety of benchmarks examples. An interesting issue in this context is to compare the accuracy and performance of different coupling strategies chosen in the models tested.

References

Abbott, M. B., Bathurst, J. C., Cunge, J. A., OConnell, P. E., Rasmussen, J., 1987a. An introduction to the european hydrological system - système hydrologique européen, she, 1: History and philosophy of a physically-based, distributed modelling system. Journal of Hydrology, 45–59.

Abbott, M. B., Bathurst, J. C., Cunge, J. A., OConnell, P. E., Rasmussen, J., 1987b. An introduction to the european hydrological system - système hydrologique européen, she, 2: Structure of a physically-based, distributed modelling system. Journal of Hydrology, 61–77.

Ames, W. R., 1992. Numerical Methods for Partial Differential Equations. Academic Press, New York.

Bear, J., 1972. Dynamics of Fluids in Porous Media. Elsevier, New York.

Bear, J., Bachmat, Y., 1990. Introduction to modelling of transport phenomena in porous media. Kluwer Academic Publishers, Dordrecht.

Begin, Z. B., Erlich, A., Nathan, I., 1974. Lisan lake, the representative of the pleistocene age in the dead sea (in hebrew). Geological Survey of Israel Bulletin 63:30.

Beinhorn, M., Guttman, J. S., Sauter, M., Toll, M., Kolditz, O., April 2004. Groundwater modelling of the shallow aquifer in the Jericho area. In: 5th Int Symposium on the Eastern Mediterranean Geology, Thessaloniki, Greece. pp. 1483–1486.

Beinhorn, M., Kolditz, O., 2003a. Triangular prismatic elements PART I: Numerical integration. Tech. rep., Nr. 2003-2, Center for Applied Geosciences, University of Tübingen.

Beinhorn, M., Kolditz, O., 2003b. Triangular prismatic elements PART II: Analytical integration. Tech. rep., Nr. 2003-30, Center for Applied Geosciences, University of Tübingen.

Beinhorn, M., Kolditz, O., 2004a. Object oriented approach to groundwater modelling. submitted to Computers and Geosciences.

Beinhorn, M., Kolditz, O., June 2004b. Object-oriented approach to preprocessing and process modelling in water resources, application to the Jericho area. In: Proceedings of the 15th International Conference on Computational Methods in Water Resources (CMWR XV), Chapel Hill, NC, USA. Elsevier, pp. 1067 – 1077.

Bevc, D., Morrison, H. F., 1991. Borehole-to-surface electrical resistivity monitoring of a salt water injection experiment. Geophysics 56, 769–777.

Brooks, R. N., Corey, A. T., 1964. Properties of porous media affecting fluid flow. J. Irrig. Drain. Div. ASCE 92, 61–68.

Chen, C., Sawarieh, A., Kalbacher, T., Beinhorn, M., Wang, W., Kolditz, O., 2004. Gis based modeling with geosys/rockflow. Tech. rep., Nr. 2004-02, Center for Applied Geosciences, University of Tübingen.

Cross, J., Masters, I., Lewis, R., 1998. Why you should consider object-oriented programming techniques for finite element techniques. International Journal of Numerical Methods for Heat and Fluid Flow 9, 333–347.

Crow, A. S., Shikaze, S. G., Schwartz, F. W., 1999. A grid generating algorithm for simulating a fluctuating water tabel boundary in heterogeneous unconfined aquifers. Advances in Water Resources 22, 567–575.

Dagan, G., 1989. Flow and Transport in Porous Formations. Springer Verlag, Berlin.

Diersch, H.-J., 1985. Modellierung und numerische simulation geohydrodynamischer transportprozesse (modeling and numerical simulation of geohydrodynamic transport processes. Tech. rep., Habilitation (Dissertation B), Academy of Sciences of GDR, Berlin, Reprint WASY Ltd, Berlin 1991.

Diersch, H.-J., 2001a. Treatment of free surfaces in 2d and 3d groundwater modelling - user's manual/reference manual/white paper. release 4.9. Tech. rep., WASY Ltd, Berlin.

Diersch, H.-J., Kolditz, O., 2002. Variable-density flow and transport in porous media: approaches and challenges. Adv. Water Res. 25, 899–944.

Diersch, H.-J. G., 2001b. Consistent velocity approximation in the finite element simulation of density- dependent mass and heat transport processe - user's manual/reference manual/white paper. Release 4.9. Tech. rep., WASY Ltd, Berlin.

Diersch, H.-J. G., 2002. WASY Software FEFLOW - Reference Manual, PartII Applications, Chapter 14 - 17. Tech. rep., WASY Ltd, Berlin.

Dorgarten, H. W., Tsang, C. F., 1990. Modelling density-driven movement of liquid waste in deep sloping aquifers. Ground Water 29, 655–662.

Dubois-Pelerin, Y., Zimmermann, T., 1993. Object-oriented finite element programming 3. an efficient implementation in c++. Computer Methods in Applied Mathematics and Engineering 108, 165–183.

Feng, K., Molz, F. G., 1997. A 2-d diffusion based wetland model. Journal of Hydrology 196, 230–250.

Feng, Z., 1995. 2d or 3d frictional contact algorithms and applications in a large deformation context. Communications in Numerical Methods in Engineering 11, 409–416.

Fenton, G. A., Griffiths, D. V., 1997. A mesh deformation algorithm for free surface problems. International Journal for Numerical and Analytical Methods in Geomechanics 21, 817–824.

Fetter, C. W., 1992. Contaminant Hydrogeology. Macmillan Publishing Company, New York.

Fiedler, F. R., Ramirez, J., 2000. A numerical method for simulating discontinuous shallow flow over an infiltrating surface. International Journal for Numerical Methods in Fluids 32, 219–240.

Galand, J. C., Hervouet, N. G. J. M., 1991. Telemac- a new numerical model for solving shallow-water equations. Advances in Water Resources 14, 138–148.

Garcia, R., Kahawita, R. A., 1989. Numerical solution of the st. venant equations with the maccormack finite difference scheme. Int. J. Numerical Methods in Fluids 6, 507–527.

Giammarco, D., Todini, P. E., Lamberti, P., 1996. A conservative finite elements approach to overland flow: the control volume finite element formulation. J. Hydrol. 175, 267–291.

gmsh, 2004.
`http://www.geuz.org/gmsh/`.

gOcad, 2004.
`http://www.ensg.inpl-nancy.fr/GOCAD/`.

Golani, U., 1972. Groundwater resources in the Jericho region. Tech. rep., Tahal Report HR/72/016 (in hebrew).

Govindaraju, R. S., Jones, S. E., Kavvas, M. L., 1988. On the diffusion wave model for overland flow 1. solution for steep slopes. Water Resour. Res. 24, 734–744.

Govindaraju, R. S., Kavvas, M. L., 1991. Dynamics of moving overland flows over infiltrating surfaces at hillslopes. Water Resour. Res. 27, 1885–1898.

Gunduz, O., Aral, M. M., 2005. River networks and groundwater flow: a simultaneous solution of a coupled system. Journal of Hydrology 301, 216–234.

Hassanizadeh, S. M., Leijnse, T., 1988. On the modelling of brine transport in porous media. Water Resources Research 24, 321–330.

Haverkamp, R., Vauclin, M., Touma, J., Wierenga, P. J., Vachaud, G., 1977. A comparison of numerical simulation models for one-dimensional infiltration. J. Soil Science Society of America 41, 284–294.

Helmig, R., 1993. Theorie und numerik der mehrphasenströmungen in geklüftet-porösen medien. PhD-Thesis, Bericht Nr. 34/1993, Institut für Strömungsmechanik und Elektronisches Rechnen im Bauwesen, Universität Hannover.

Hoffmann, R., Dietrich, P., 2004. Geoelektrische Messungen zur Bestimmung von Grundwasserfließrichtungen und - geschwindigkeiten. Grundwasser, accepted.

Holzbecher, E., 1998. Modelling density-driven flow in porous media. Springer, Berlin.

Hromadka, T. V., Berenbrock, C. E., Freckleton, J. R., Guymon, G. L., 1985. A two-dimensional dambreak flood plain model. Adv. Water Resources 8.

Hromadka, T. V., McCuen, R. H., Yen, C. C., 1987. Comparison of overland flow hydrograph models. J. Hydr. Eng., ASCE 104, 1422–1440.

Hromadka, T. V., Yen, C. C., 1987. A diffusion hydrodynamic model. U.S. Geological Survey, Water Resources Investigations Report 87-4137.

Huyakorn, P., Springer, E., Guvanasen, V., Wadsworth, T., 1986. A three-dimensional finite-element model for simulating water flow in variably saturated porous media. Water Resources Research 22, 1790–1808.

Huyakorn, P., Thomas, S., 1984. Techniques for making finite elements competitive in modelling flow in variably saturated porous media. Water Resources Research 20, 1099–1115.

HYDROGeoLogic, 2005. `//http://www.hgl.com/flash/index.cfm`.

Hydrosphere, 2004.
`http://sciborg.uwaterloo.ca/ mclaren/public/` or
`http://www.modhms.com/software/hydrosphere.html`.

IGSM, 2005. `//http://modeling.water.ca.gov/hydro/model/indexigsm2.html`.

Istok, J. D., Humphrey, M. D., 1995. Laboratory investigation of buoyancy-induced flow (plume sinking during two-well tracer tests). Groundwater 33, 597–604.

Jaber, F. H., Mohtar, R. H., 2003. Stability and accuracy of two-dimensional kinematic wave overland flow modeling. Advances in Water Resources 26, 1189–1198.

Jain, S. C., 2001. Open-Channel Flow. John Wiley and Sons, New York.

Jalbert, M., Dane, J. H., Abriola, L. M., Pennell, K. D., 2000. A nondimensional evaluation of tracer sensitivity to density effects. Groundwater 38, 226–233.

Kalbacher, T., Beinhorn, M., Kolditz, O., Dezember 2003a. PrisGen - Mesh generator for prismatic elements. GeoSys-Report 2003-34, Center for Applied Geoscience, University of Tübingen.

Kalbacher, T., Wang, W., McDermott, C., Kolditz, O., Taniguchi, T., May 2003b. Development and application of a CAD interface for fractured rock. GeoSys-Report 2003-05, www.rockflow.net, Center for Applied Geoscience, University of Tübingen.

Kemna, A., Vanderborght, J., Kulessa, B., Vereecken, H., 2002. Imaging and characterisation of subsurface solute transport using electrical resistivity tomography (ert) and equivalent transport models. Journal of Hydrology 267, 125–146.

Kimmel, G. E., Braids, O. C., 1980. Leachate plumes in groundwater from Babylon and Islip landfills, Long Island, New York. U.S. Geol. Surv. Prof. Pap. 1085.

Koch, M., Zang, G., 1992. Numerical simulation of the effects of variable density in a contaminant plume. Ground Water 30, 731–742.

Kolditz, O., 2001. Non-linear flow in fractured rock. Int J. Numerical Methods in Fluid and Heat Transport 11, 547–576.

Kolditz, O., 2002. Computational methods in environmental fluid mechanics. Graduate Text Book, Springer Science Publisher, Berlin.

Kolditz, O., Bauer, S., 2003. A process-oriented approach to compute multi-field problems in porous media. Journal of Hydroinformatics, accepted for publication.

Kolditz, O., Bauer, S., 2004. A process-oriented approach to compute multi-field problems in porous media. Journal of Hydroinformatics, accepted for publication.

Kolditz, O., de Jonge, J., 2004. Non-isothermal two-phase flow in low-permeable porous media. Computational Mechanics 33, 345–364.

Kolditz, O., de Jonge, J., Beinhorn, M., Xie, M., Kalbacher, T., Wang, W., Bauer, S., McDermott, C., Chen, C., Beyer, C., Gronewold, J., Kemmler, D., Manabe, T., Legeida, D., Adamidis, P., 2003. GeoSys - Theory and users manual, release 3.9.11. GeoHydrology / HydroInformatics, Center for Applied Geoscience, University of Tübingen.

Kolditz, O., Ratke, R., Diersch, H.-J. G., Zielke, W., 1998. Coupled groundwater flow and transport: 1. Verification of variable density flow and transport models. Advances in Water Resources 21, 27–46.

LeBlanc, D. R., Garabedian, S. P., Hess, K. M., Gelhar, L. W., Quadri, R. D., Stollenwerk, K. G., Wood, W. W., 1991. Large scale natural gradient tracer test in sand and gravel Cape Cod, Massachusetts: Experimental design and observed tracer movement. Water Resources Research 27, 895–910.

Liedl, R., 2004. 1-d saint venant equations. Tech. rep., Nr. 2004-X, Center for Applied Geosciences, University of Tübingen.

MacFarlane, D. S., Cherry, J. A., Gillham, R. W., Sudicky, E. A., 1983. Migration of contaminants in groundwater at a landfill: A case study, 1, groundwater flow and plume deliniation. J. Hydrol. 63.

Mackie, R., 1992. Object-oriented programming of the finite element method. International Journal for Numerical Methods in Engineering 35, 425–436.

Manabe, T., Kalbacher, T., Kolditz, O., Taniguchi, T., Dezember 2003. TetMesh - Mesh generator for tetrahedral elements. GeoSys-Report 2003-35, University of Okayama and Center for Applied Geoscience, University of Tübingen.

Marie, A., Vengosh, A., 2001. Sources of salinity in ground water from Jericho area, jordan valley. Groundwater 39:2, 240–248.

Masters, I., Cross, J. T., Lewis, R. W., 1997. A review of object oriented programming techniques in finite element methods. In: Intnernational Conference for Numerical Methods in Thermal Problems. Pineridge Press, pp. 1001–1009.

Mentrey, P., Zimmermann, T., 1993. Object-oriented non-linear finite element analysis - application to j2 plasticity. Computers and Structures 49, 767–777.

Morgali, J. R., 1970. Laminar and turbulent overland flow hydrographs. J. Hydr. Div., ASCE, 441–460.

Morris, M., 1996. Geoelectrical monitoring of a tracer injection experiment: Modelling and interpretation. European Journal of Environmental and Engineering Geophysics 1, 15–34.

Nield, D. A., Bejan, A., 1999. Convection in porous media. 2nd ed. Springer, New York.

Ohtsubo, H., Kawamura, Y., Kubota, A., 1993. Development of the object-oriented finite element modelling system. Engineering with Computers 9, 187–197.

Oostrom, M., Hayworth, J. S., Dane, J. H., Güven, O., 1992. Behavior of dense aqueous phase leachate plumes in homogeneous porous media. Water Resources Research 28, 2123–2134.

Oswald, S. E., Kinzelbach, W., 2004. Three-dimensional physical benchmark experiments to test variable-density flow models. Journal of Hydrology 290, 22–42.

Paschke, N. W., Hoopes, J., 1984. Buoyant contaminant plumes in groundwater. Water Resources Research 20, 1183–1192.

Pebesma, E. J., Wesseling, C. G., 1998. Gstat: A program for geostatistical modelling, prediction and simulation. Computers and Geosciences 24, 17–31.

Peskin, A., Hardin, G., 1996. An object-oriented approach to general-purpose fluid-dynamics software. Computers and Chemical Engineering 20, 1043–1058.

Pidaparti, R., Hudli, A., 1996. Dynamic analysis of structures using object-oriented techniques. Computers and Structures 49, 149–156.

Ponce, V. M., Ruh-Ming, L., Simons, D. B., 1978. Applicability of kinematic and diffusion waves. J. Hydr. Div., ASCE 104, 353–360.

Ratke, R., Kolditz, O., Zielke, W., 1996. Rockflow: Dreidimensionales Dichtemodell DM2/3d. Tech. rep., Institut für Strömungsmechanik, Universität Hannover.

Richards, L. A., 1931. Capillary conduction of liquids through porous media. Physics 1, 318–333.

Rijn, L. C. V., 1986. Principles of Fluid Flow and Surface Waves in Rivers, Estuaries, Seas and Oceans. Aqua Publications, The Netherlands.

Sawarieh, A., Chen, C., Kalbacher, T., Beinhorn, M., Kolditz, O., November 2004. A gis based model for ground-water flow and heat transport in zarqa main/jiza areas, central jordan. In: Water Resources and Environmental Protection in the Middle East and North Africa , Amman, Jordan.

Schincariol, R. A., Schwartz, F. W., 1990. An experimental investigation of variable density flow and mixing in homogeneous and heterogeneous media. Water Resources Research 26, 2317–2329.

Schmitz, G. H., Liedl, R., Volker, R. E., 2002. Analytical solution to the zero-inertia problem for surge flow phenomena in non-prismatic channels. J. Hydraul. Engng. 128, 604–615.

Scholz, S., 1992. Elements of an object-oriented fem++ program in c++. Computers and Structures 43, 517–529.

Simmons, C. T., Fenstemaker, T. R., Sharp, J. M., 2001. Variable-density groundwater flow and solute transport in heterogeneous porous media: approaches, resolutions and future challenges. Journal of Contaminant Hydrology 52, 245–275.

Simpson, M. J., Clement, T. P., 2003. A theoretical analysis of the worthiness of henry and elder problems as benchmarks of density-dependent groundwater flow models. Advances in Water Resources 26, 17–31.

Simpson, M. J., Clement, T. P., 2004. Improving the worthiness of the henry problem as a benchmark for density-dependent ground water flow problems. Water Resources Research, W01504, doi:10.1029/2003WR002199 40.

Slater, L., Binley, A., Johnson, W. D. D. R., 2000. Cross-hole electrical imaging of a controlled saline tracer injection. J. Appl. Geophys. 44, 85–102.

Smith, R. E., Woolhiser, D. A., 1971. Overland flow on an infiltrating surface. Water Resour. Res. 7, 899–913.

Thorenz, C., 2001. Model adaptive simulation of multiphase and density driven flow in fractured and porous media. PhD-Thesis, Bericht Nr. 61/2001, Institut für Strömungsmechanik und Elektronisches Rechnen im Bauwesen, Universität Hannover.

Van Genuchten, M. T., 1980. A closed-form equation for predicting the hydraulic conductivity of unsaturated soils. Soil Sci. Soc. Am. J. 44, 892–898.

VanderKwaak, J. E., Loague, K., 2001. Hydrologic-response simulations for the r-5 catchment with a comprehensive physics-based model. Water Resources Research 37, 999–1013.

Vreugdenhil, C. B., 1994. Numerical Methods for Shallow-water flow. Kluwer academic publishers, Dordrecht.

WASY, 2005.
`http://www.wasy.de/deutsch/index.html`.

Weatherill, D., Simmons, C. T., Voss, C. I., Robinson, N., 2004. Testing density-dependent groundwater models: two-dimensional steady state unstable convection in infinite, finite and inclined porous layers. Advances in Water Resources 27, 547–562.

White, P. A., 1988. Measurement of ground-water parameters using salt-water injection and surface resistivity. Ground Water 26, 179–186.

Wood, M., Simmons, C. T., Hutson, J. L., 2004. A breakthrough curve analysis of unstable density driven flow and transport in homogeneous porous media. Water Resources Research 40, W03505, doi:10.1029/2003WR002668.

Xanthopoulos, T., Koutitas, C., 1976. Numerical simulation of a two-dimensional flood wave propagation due to dam-failure. J. Hydraul. Res. 14, 321–331.

Zang, W., Cundy, T. W., 1989. Modeling of two-dimensional overland flow. Water Resour. Res. 25, 2019–2035.

Zhang, H., Schwartz, F. W., Wood, W. W., Garabedian, S. P., LeBlanc, D. R., 1998. Simulation of variable density flow and transport of reactive and nonreactive solutes during a tracer test at Cape Cod, Massachusetts. Water Resources Research 34, 67–82.

Zhao, D. H., Shen, H. W., Tabios, I., Lai, J. S., Tan, W. Y., 1994. Finite-volume tow-dimensional unsteady flow model for river basins. J. of Hydr. Eng., ASCE 120, 863–883.

Zienkiewicz, O. C., Taylor, R. L., 2000. The Finite Element Method, 5th Edition. Vol. 1. Butterworth-Heinemann, Oxford.

Zimmermann, T., Dubois-Pelerin, Y., Bomme, P., 1992. Object-oriented finite element programming 1: Governing principles. Computers Methods in Applied Mechanics and Engineering 98, 291–303.

9 Appendix

9.1 Some mathematical notations

The Divergence operator
"Divergence of $\mathbf{q}$" (div $\mathbf{q}$ or $\nabla \cdot \mathbf{q}$) $\nabla \cdot \mathbf{q}$ tells us how much a flow rate might change at any given point. The divergence of a vector is given by

$$\nabla \cdot \mathbf{q} = \frac{\partial q_x}{\partial x} + \frac{\partial q_y}{\partial y} + \frac{\partial q_z}{\partial z}$$

Conservation of mass
The net mass outflow per unit volume per unit time must be equal to the time rate of change in mass per unit volume within the test volume. Hence:

$$\nabla \cdot (\rho \mathbf{q}) = \frac{\partial(\rho n)}{\partial t}$$

The Gradient
"del operator" ∇ or "the gradient p of grad p where ∇ is known as the "del" operator (or "that funny upside down triangle"). Partial derivatives are used to talk about the change of a function with direction in terms of a vector.

$$\nabla p = \begin{pmatrix} \frac{\partial p}{\partial x} \\ \frac{\partial p}{\partial x} \\ \frac{\partial p}{\partial z} \end{pmatrix}$$

The Gauss-Ostrogradskian integral theorem
The Gauss-Ostrogradskian integral theorem (or divergence theorem) can be used to transform surface into volume integrals for the flux term. It states that the flux of a vector field across a closed surface is equal to the divergence of the vector field throughout the enclosed volume.

$$\oint_{\partial\Omega} \mathbf{\Phi}^{\psi} \cdot d\mathbf{S} = \int_{\Omega} \nabla \cdot \mathbf{\Phi}^{\psi} d\Omega$$

Cyclic permutation

$$\begin{aligned} Q_\rho &= \frac{\partial}{\partial x_\alpha}\left(\frac{k_{\alpha\beta}}{\mu}(\frac{\partial p}{\partial x_\beta} + \rho g \frac{\partial z}{\partial x_\beta})\right) \quad , \quad \alpha, \beta = 1, 2, 3 \\ &= \frac{\partial}{\partial x_\alpha}\frac{1}{\mu}\left(k_{\alpha x}\frac{\partial p}{\partial x} + k_{\alpha y}\frac{\partial p}{\partial y} + k_{\alpha z}\frac{\partial p}{\partial z}\right) \end{aligned}$$

$$
\begin{aligned}
= & \frac{1}{\mu}\left(k_{xx}\frac{\partial^2 p}{\partial x \partial x} + k_{yx}\frac{\partial^2 p}{\partial x \partial y} + k_{zx}\frac{\partial^2 p}{\partial x \partial z}\right) \\
& + \frac{1}{\mu}\left(k_{xy}\frac{\partial^2 p}{\partial y \partial x} + k_{yy}\frac{\partial^2 p}{\partial y \partial y} + k_{zy}\frac{\partial^2 p}{\partial y \partial z}\right) \\
& + \frac{1}{\mu}\left(k_{xz}\frac{\partial^2 p}{\partial z \partial x} + k_{yz}\frac{\partial^2 p}{\partial z \partial y} + k_{zz}\frac{\partial^2 p}{\partial z \partial z}\right)
\end{aligned}
$$

Conductivity- and permeability tensor ($\mathbf{K}$ and $\mathbf{k}$)

$$\mathbf{K} = \mathbf{k}\frac{\rho g}{\mu}$$

The determinant of a matrix

$\det \mathbf{A}$ is the determinant of the matrix $\mathbf{A}$. The determinant is only defined for square matrices

$$\det \mathbf{A} = \sum_{j=1}^{n}(-1)^{1+j} a_{1j} \det \mathbf{A}_{1j}$$

with $\mathbf{A}$ the Matrix of the order (n-1) x (n-1) if line 1 and column j of $\mathbf{A}$ are cancelled.

- If $\mathbf{A} = a_{11}$. Then $\det \mathbf{A} = a_{11}$
- If $\mathbf{A} = \begin{bmatrix} a_{11} & a_{12} \\ a_{21} & a_{22} \end{bmatrix}$. Then $\det \mathbf{A} = a_{11}a_{22} - a_{12}a_{21}$
- If $\mathbf{A} = \begin{bmatrix} a_{11} & a_{12} & a_{13} \\ a_{21} & a_{22} & a_{23} \\ a_{31} & a_{32} & a_{33} \end{bmatrix}$. Then $\det \mathbf{A} = a_{11}(a_{22}a_{33} - a_{32}a_{23}) - a_{12}(a_{21}a_{33} - a_{31}a_{23}) + a_{13}(a_{21}a_{32} - a_{31}a_{22})$

Coordinate transformation

A coordinate transformation from local to global coordinates is performed using the Jacobian matrix $[J_{3D}]$. Using the chain rule the derivative of an interpolation function $\partial N/\partial r$ can be written as

$$\frac{\partial N}{\partial r} = \frac{\partial N}{\partial x}\frac{\partial x}{\partial r} = \frac{\partial N}{\partial x}[J_{3D}]$$

or as the inverse coordinate transformation

$$\frac{\partial N}{\partial x} = \frac{1}{\partial x/\partial r}\frac{\partial N}{\partial r} = [J_{3D}]^{-1}\frac{\partial N}{\partial x}$$

Jacobian matrix $[J_{3D}]$

For a one-dimensional element the Jacobian matrix $[J_{3D}]$ is given by

$$[J_{1D}] = \frac{\partial x}{\partial r} = \frac{\partial N_1}{\partial r} x_1 + \frac{\partial N_2}{\partial r} x_2 = -\frac{1}{2}\, x_1 + \frac{1}{2}\, x_2 \frac{1}{2}(x_2 - x_1) = \frac{1}{2} L^e$$

and

$$[J_{1D}^{-1}] = \frac{1}{[J_{1D}]} = \frac{2}{L^e}$$

and

$$\det[J_{1D}] = \frac{1}{2} L^e$$

9.2 Partial integration and further manipulation of the integral formulation of the governing groundwater flow equation

$$\int_\Omega \phi_i \left[S_0^p \phi_j \frac{dp_j}{dt} - \frac{\partial}{\partial x_\alpha} \left(\frac{k_{\alpha\beta}}{\mu} (\frac{\partial \phi_j}{\partial x_\beta} p_j + \rho g \frac{\partial \phi_j}{\partial x_\beta} z_j) \right) \right] d\Omega = \int_\Omega \phi_i Q_\rho d\Omega$$

$$A = \left(\frac{k_{\alpha\beta}}{\mu} (\frac{\partial \phi_j}{\partial x_\beta} p_j + \rho g \frac{\partial \phi_j}{\partial x_\beta} z_j) \right)$$

$$\int_\Omega \left[\left(\phi_i S_0^p \phi_j \frac{dp_j}{dt} \right) - \left(\phi_i \frac{\partial}{\partial x_\alpha} A \right) \right] d\Omega = \int_\Omega \phi_i Q_\rho d\Omega$$

$$\phi \nabla A = \nabla(\phi A) - A \nabla \phi$$

$$\phi_i \frac{\partial}{\partial x_\alpha} A = \frac{\partial}{\partial x_\alpha} (\phi_i A) - \frac{\partial \phi_i}{\partial x_\alpha} (A)$$

so partial integration leads to

$$\int_\Omega \left[\left(\phi_i S_0^p \phi_j \frac{dp_j}{dt} \right) - \left(\frac{\partial}{\partial x_\alpha} (\phi_i A) - \frac{\partial \phi_i}{\partial x_\alpha} (A) \right) \right] d\Omega = \int_\Omega \phi_i Q_\rho d\Omega$$

$$\int_\Omega \left[\left(\phi_i S_0^p \phi_j \frac{dp_j}{dt} \right) + \left(\frac{\partial \phi_i}{\partial x_\alpha} (A) \right) \right] d\Omega = \int_\Omega \left(\frac{\partial}{\partial x_\alpha} (\phi_i A) \right) \int_\Omega \phi_i Q_\rho d\Omega$$

applying the Gauss-Ostrogradskian integral theorem the Fluxes vertically to the planes can be written as

$$\frac{\partial}{\partial x_\alpha} (\phi_i A) = \frac{\partial}{\partial x_\alpha} (\phi_i q_n)$$

with the outward flux vector

$$q_n = -\frac{k_{\alpha\beta}}{\mu} (\frac{\partial \hat{p}}{\partial x_\beta} + \rho g \frac{\partial z}{\partial x_\beta}) n_\alpha$$

applying that leads to

$$-\int_{\Omega}\frac{\partial}{\partial x_{\alpha}}\phi_i q_n d\Omega = +\int_{\partial\Omega}\phi_i q_n dS$$

substitution leads to

$$\int_{\Omega}\left[\left(\phi_i S_0^p \phi_j \frac{dp_j}{dt}\right) + \frac{\partial \phi_i}{\partial x_{\alpha}}(A)\right] d\Omega = -\int_{\partial\Omega}\phi_i q_n dS + \int_{\Omega}\phi_i Q_{\rho} d\Omega$$

Rearrangement yields

$$\int_{\Omega}\left[\phi_i S_0^p \phi_j \frac{dp_j}{dt} + \frac{\partial \phi_i}{\partial x_{\alpha}}\frac{k_{\alpha\beta}}{\mu}\frac{\partial \phi_i}{\partial x_{\beta}} p_j\right] d\Omega$$
$$= -\int_{\Omega}\left[\frac{\partial \phi_i}{\partial x_{\alpha}}\frac{k_{\alpha\beta}}{\mu}\rho g \frac{\partial \phi_j}{\partial x_{\beta}})z_j d\Omega\right] - \int_{\partial\Omega}\phi_i q_n dS + \int_{\Omega}\phi_i d\Omega$$

9.3 Derivation of 1-D element matrix expressions for fluid flow

Conductance matrix

$$
\begin{aligned}
\mathbf{K}^e &= A^e \int_{-1}^{+1} \begin{bmatrix} \partial N_1/\partial r \\ \partial N_2/\partial r \end{bmatrix} [J_{1D}^{-1}]^T \left(\frac{k_{\mathsf{rel}}\mathbf{k}}{\mu}\right) \\
&\quad \begin{bmatrix} \partial N_1/\partial r \\ \partial N_2/\partial r \end{bmatrix}^T [J_{1D}^{-1}] \, \det[J_{1D}] \, dr \\
&= A^e \int_{-1}^{+1} \begin{bmatrix} -\frac{1}{2} \\ \frac{1}{2} \end{bmatrix} \left[\frac{2}{L^e}\right] \left(\frac{k_{\mathsf{rel}}\mathbf{k}}{\mu}\right) \begin{bmatrix} -\frac{1}{2} \\ \frac{1}{2} \end{bmatrix}^T \left[\frac{2}{L^e}\right] \frac{1}{2} L^e \, dr \\
&= \left(\frac{k_{\mathsf{rel}}\mathbf{k}}{\mu}\right)^e A^e \begin{bmatrix} \frac{1}{4} & -\frac{1}{4} \\ -\frac{1}{4} & \frac{1}{4} \end{bmatrix} \frac{2}{L^e} \int_{-1}^{+1} dr \\
&= \left(\frac{k_{\mathsf{rel}}\mathbf{k}}{\mu}\right)^e \frac{A^e}{L^e} \begin{bmatrix} 1 & -1 \\ -1 & 1 \end{bmatrix}
\end{aligned}
$$

Capacitance matrix

$$
\begin{aligned}
\mathbf{C}^e &= A^e \int_{-1}^{+1} \begin{bmatrix} N_1 \\ N_2 \end{bmatrix} S_0^e \begin{bmatrix} N_1 \\ N_2 \end{bmatrix}^T \det[J_{1D}] \, dr \\
&= A^e \int_{-1}^{+1} \begin{bmatrix} N_1 \\ N_2 \end{bmatrix} S_0^e \begin{bmatrix} N_1 \\ N_2 \end{bmatrix}^T \frac{1}{2} L^e \, dr \\
&= \frac{A^e S_0^e L^e}{2} \int_{-1}^{+1} \begin{bmatrix} N_1 \\ N_2 \end{bmatrix} \begin{bmatrix} N_1 \\ N_2 \end{bmatrix}^T dr \\
&= \frac{A^e S_0^e L^e}{2} \int_{-1}^{+1} \begin{bmatrix} \frac{(1-r)^2}{4} & \frac{1-r^2}{4} \\ \frac{1-r^2}{4} & \frac{(1+r)^2}{4} \end{bmatrix} dr \\
&= \frac{A^e S_0^e L^e}{2} \int_{-1}^{+1} \begin{bmatrix} A & B \\ C & D \end{bmatrix} dr
\end{aligned}
$$

$$
\int_{-1}^{+1} A = \int_{-1}^{+1} \frac{(1-r)^2}{4} \, dr = \frac{1}{4} \left| -\frac{1}{3}(1-r)^3 \right|_{-1}^{1} = \frac{2}{3}
$$

$$
\int_{-1}^{+1} B = \int_{-1}^{+1} C = \int_{-1}^{+1} \frac{1-r^2}{4} \, dr = \frac{1}{4} \left| r - \frac{1}{3} r^3 \right|_{-1}^{1} = \frac{1}{3}
$$

$$
\int_{-1}^{+1} D = \int_{-1}^{+1} \frac{(1+r)^2}{4} \, dr = \frac{1}{4} \left| \frac{1}{3}(1-r)^3 \right|_{-1}^{1} = \frac{2}{3}
$$

$$
\begin{aligned}
\mathbf{C}^e &= \frac{A^e S_0^e L^e}{2} \int_{-1}^{+1} \begin{bmatrix} A & B \\ C & D \end{bmatrix} dr \\
&= \frac{A^e S_0^e L^e}{2} \begin{bmatrix} \frac{2}{3} & \frac{1}{3} \\ \frac{1}{3} & \frac{2}{3} \end{bmatrix} \\
&= S_0^e \frac{A^e L^e}{6} \begin{bmatrix} 2 & 1 \\ 1 & 2 \end{bmatrix}
\end{aligned}
$$

Gravity forces

$$
\begin{aligned}
\mathbf{g}^e &= \int_{\Omega^e} \nabla \mathbf{N} \left(\frac{k_{\mathsf{rel}} \mathbf{k}}{\mu} \rho \mathbf{g} \right) d\Omega^e \\
&= [\mathbf{K}^e] \times (z) \\
&= \left(\frac{k_{\mathsf{rel}} \mathbf{k}}{\mu} \right)^e \frac{A^e}{L^e} \begin{bmatrix} 1 & -1 \\ -1 & 1 \end{bmatrix} \times (z) \\
&= \left(\frac{k_{\mathsf{rel}} \mathbf{k}}{\mu} \right)^e \frac{A^e}{L^e} \begin{bmatrix} 1 & -1 \\ -1 & 1 \end{bmatrix} \times \begin{bmatrix} 0 \\ z_2 - z_1 \end{bmatrix} \\
&= \left(\frac{k_{\mathsf{rel}} \mathbf{k}}{\mu} \right)^e \frac{A^e}{L^e} \begin{bmatrix} 0 - 1\,(z_2 - z_1) \\ 0 + 1\,(z_2 - z_1) \end{bmatrix} \\
&= \left(\frac{k_{\mathsf{rel}} \mathbf{k}}{\mu} \right)^e \frac{A^e}{L^e} \begin{bmatrix} 0 + 1\,(z_1 - z_2) \\ 0 - 1\,(z_1 - z_2) \end{bmatrix} \\
&= \left(\frac{k_{\mathsf{rel}} \mathbf{k}}{\mu} \rho \mathbf{g} \right) \frac{A^e}{L^e} (z_1 - z_2) \begin{bmatrix} +1 \\ -1 \end{bmatrix}
\end{aligned}
$$

9.4 Some detailed calculations for the analytical evaluation of element matric expressions for triangular prismatic elements, fluid flow

Capacitance matrix

$$
\begin{aligned}
C_{ij} &= \int_\Omega N_i S_0 N_j \, d\Omega = S_0 \int_V N_i^\Delta N_j^\Delta N_i^t N_j^t \, dV \\
&= S_0 \int_\Delta N_i^\Delta N_j^\Delta dA \times \int_z N_i^t N_j^t \, dz \\
&= S_0 \int_\Delta N_i^\Delta N_j^\Delta dA \times \int_{-1}^{1} N_i^t N_j^t \, det[J_{3D}^z] \, dt \\
&= S_0 \; det[J_{3D}^z] \underbrace{\int_\Delta N_i^\Delta N_j^\Delta dA}_{\mathbf{C}^\Delta} \times \underbrace{\int_{-1}^{1} N_i^t N_j^t dt}_{\mathbf{C}^t}
\end{aligned}
$$

Linear component of the capacitance matrix $\mathbf{C}^t$:

$$
C_{ij}^t = \int_{-1}^{1} N_i^t N_j^t dt \;=\; \int_{-1}^{1} \begin{bmatrix}
N_1^t N_1^t & N_1^t N_1^t & N_1^t N_1^t & N_1^t N_2^t & N_1^t N_2^t & N_1^t N_2^t \\
N_1^t N_1^t & N_1^t N_1^t & N_1^t N_1^t & N_1^t N_2^t & N_1^t N_2^t & N_1^t N_2^t \\
N_1^t N_1^t & N_1^t N_1^t & N_1^t N_1^t & N_1^t N_2^t & N_1^t N_2^t & N_1^t N_2^t \\
N_2^t N_1^t & N_2^t N_1^t & N_2^t N_1^t & N_2^t N_2^t & N_2^t N_2^t & N_2^t N_2^t \\
N_2^t N_1^t & N_2^t N_1^t & N_2^t N_1^t & N_2^t N_2^t & N_2^t N_2^t & N_2^t N_2^t \\
N_2^t N_1^t & N_2^t N_1^t & N_2^t N_1^t & N_2^t N_2^t & N_2^t N_2^t & N_2^t N_2^t
\end{bmatrix} dt
$$

$$
\begin{aligned}
\int_{-1}^{1} N_1^t N_1^t \, dt &= \int_{-1}^{1} \left(\frac{1-t}{2}\right)^2 dt = \frac{1}{4} \left| -\frac{1}{3}(1-t)^3 \right|_{-1}^{1} = \frac{2}{3} \\
\int_{-1}^{1} N_1^t N_2^t \, dt &= \int_{-1}^{1} N_2^t N_1^t \, dt = \int_{-1}^{1} \left(\frac{1-t}{2}\right)\left(\frac{1+t}{2}\right) dt \\
&= \frac{1}{4} \int_{-1}^{1} 1 - t^2 dt = \frac{1}{4} \left| t - \frac{1}{3} t^3 \right|_{-1}^{1} = \frac{1}{3} \\
\int_{-1}^{1} N_2^t N_2^t \, dt &= \int_{-1}^{1} \left(\frac{1+t}{2}\right)^2 dt = \frac{1}{4} \left| \frac{1}{3}(1+t)^3 \right|_{-1}^{1} = \frac{2}{3}
\end{aligned}
$$

Triangular component of the capacitance matrix $\mathbf{C}^\Delta$:

$$
\begin{aligned}
c_{11}^\Delta &= \int_\Delta N_1^\Delta N_1^\Delta \, dA = \frac{2!0!0!}{(2+0+0+2)!} \, 2A = \frac{2}{12} \, A \\
c_{12}^\Delta &= \int_\Delta N_1^\Delta N_2^\Delta \, dA = \frac{1!1!0!}{(1+1+0+2)!} \, 2A = \frac{1}{12} \, A
\end{aligned}
$$

$$
\begin{aligned}
c_{13}^{\Delta} &= \int_{\Delta} N_1^{\Delta} N_3^{\Delta}\, dA = \frac{1!0!1!}{(1+0+1+2)!}\, 2A = \frac{2}{12}\, A \\
c_{21}^{\Delta} &= \int_{\Delta} N_2^{\Delta} N_1^{\Delta}\, dA = \frac{1!1!0!}{(1+1+0+2)!}\, 2A = \frac{1}{12}\, A \\
c_{22}^{\Delta} &= \int_{\Delta} N_2^{\Delta} N_2^{\Delta}\, dA = \frac{0!2!0!}{(0+2+0+2)!}\, 2A = \frac{2}{12}\, A \\
c_{23}^{\Delta} &= \int_{\Delta} N_2^{\Delta} N_3^{\Delta}\, dA = \frac{0!1!1!}{(0+1+1+2)!}\, 2A = \frac{1}{12}\, A \\
c_{31}^{\Delta} &= \int_{\Delta} N_3^{\Delta} N_1^{\Delta}\, dA = \frac{1!0!1!}{(1+0+1+2)!}\, 2A = \frac{1}{12}\, A \\
c_{32}^{\Delta} &= \int_{\Delta} N_3^{\Delta} N_2^{\Delta}\, dA = \frac{1!0!1!}{(1+0+1+2)!}\, 2A = \frac{1}{12}\, A \\
c_{33}^{\Delta} &= \int_{\Delta} N_3^{\Delta} N_3^{\Delta}\, dA = \frac{0!0!2!}{(0+0+2+2)!}\, 2A = \frac{2}{12}\, A \\
\mathbf{c}^{\Delta} &= \begin{bmatrix} 2 & 1 & 1 \\ 1 & 2 & 1 \\ 1 & 1 & 2 \end{bmatrix} \frac{A}{12}
\end{aligned}
$$

Conductance Matrix

$$
\begin{aligned}
K_{ij}^{xx} &= \int_{\Omega} \frac{\partial N_i}{\partial x}\frac{\partial N_j}{\partial x}\, d\Omega = \int_{\Omega} \frac{\partial}{\partial x}(N_i^{\Delta} N_i^t)\frac{\partial}{\partial x}(N_j^{\Delta} N_j^t)\, d\Omega \\
&= \left(\frac{\partial N_i^{\Delta}}{\partial x} N_i^t + N_i^{\Delta}\frac{\partial N_i^t}{\partial x}\right)\left(\frac{\partial N_j^{\Delta}}{\partial x} N_j^t + N_j^{\Delta}\frac{\partial N_j^t}{\partial x}\right)\, d\Omega = \int_{\Omega} \frac{\partial N_i^{\Delta}}{\partial x}\frac{\partial N_j^{\Delta}}{\partial x} N_i^t N_j^t\, dA\, dz \\
&= \int_{\Delta} \frac{\partial N_i^{\Delta}}{\partial x}\frac{\partial N_j^{\Delta}}{\partial x}\, dA \times \int_z N_i^t N_j^t\, dz = \int_{\Delta} \frac{\partial N_i^{\Delta}}{\partial x}\frac{\partial N_j^{\Delta}}{\partial x}\, dA \times \int_{-1}^{1} N_i^t N_j^t\, det[J_{3D}^z]\, dt \\
&= det[J_{3D}^z] \int_{\Delta} \frac{\partial N_i^{\Delta}}{\partial x}\frac{\partial N_j^{\Delta}}{\partial x}\, dA \times \int_{-1}^{1} N_i^t N_j^t\, dt \\
&= det[J_{3D}^z] A \underbrace{\frac{\partial N_i^{\Delta}}{\partial x}\frac{\partial N_j^{\Delta}}{\partial x}}_{\mathbf{K}^{\Delta x}} \times \underbrace{\int_{-1}^{1} N_i^t N_j^t\, dt}_{\mathbf{C}^t} \\
K_{ij}^{yy} &= \int_{\Omega} \frac{\partial N_i}{\partial y}\frac{\partial N_j}{\partial y}\, d\Omega = det[J_{3D}^z] A \underbrace{\frac{\partial N_i^{\Delta}}{\partial y}\frac{\partial N_j^{\Delta}}{\partial y}}_{\mathbf{K}^{\Delta y}} \times \underbrace{\int_{-1}^{1} N_i^t N_j^t\, dt}_{\mathbf{C}^t} \\
K_{ij}^{zz} &= \int_{\Omega} \frac{\partial N_i}{\partial z}\frac{\partial N_j}{\partial z}\, d\Omega = \int_{\Omega} \frac{\partial}{\partial z}(N_i^{\Delta} N_i^t)\frac{\partial}{\partial z}(N_j^{\Delta} N_j^t)\, d\Omega \\
&= \int_{\Omega} N_i^{\Delta} N_j^{\Delta}\frac{\partial N_i^t}{\partial z}\frac{\partial N_j^t}{\partial z} + \frac{\partial N_i^{\Delta}}{\partial z}\frac{\partial N_j^{\Delta}}{\partial z} N_i^t N_j^t\, d\Omega = \int_{\Delta} N_i^{\Delta} N_j^{\Delta}\, dA \times \int_z \frac{\partial N_i^t}{\partial z}\frac{\partial N_j^t}{\partial z}\, dz \\
&= \int_{\Delta} N_i^{\Delta} N_j^{\Delta}\, dA \times \int_{-1}^{1} \frac{\partial N_i^t}{\partial z}[J_{3D}^z]^{-1}\frac{\partial N_j^t}{\partial z}[J_{3D}^z]^{-1}\, det[J_{3D}^z]\, dz \\
&= [J_{3D}^z]^{-1} \int_{\Delta} N_i^{\Delta} N_j^{\Delta}\, dA \times \int_{-1}^{1} \frac{\partial N_i^t}{\partial t}\frac{\partial N_j^t}{\partial t}\, dt
\end{aligned}
$$

$$\int_{-1}^{1} \frac{\partial N_i^t}{\partial t} \frac{\partial N_j^t}{\partial t}\, dt = \frac{1}{4} \begin{bmatrix} 1 & 1 & 1 & -1 & -1 & -1 \\ 1 & 1 & 1 & -1 & -1 & -1 \\ 1 & 1 & 1 & -1 & -1 & -1 \\ -1 & -1 & -1 & 1 & 1 & 1 \\ -1 & -1 & -1 & 1 & 1 & 1 \\ -1 & -1 & -1 & 1 & 1 & 1 \end{bmatrix} \int_{-1}^{1} 1\, dt$$

$$= \frac{1}{2} \begin{bmatrix} 1 & 1 & 1 & -1 & -1 & -1 \\ 1 & 1 & 1 & -1 & -1 & -1 \\ 1 & 1 & 1 & -1 & -1 & -1 \\ -1 & -1 & -1 & 1 & 1 & 1 \\ -1 & -1 & -1 & 1 & 1 & 1 \\ -1 & -1 & -1 & 1 & 1 & 1 \end{bmatrix}$$

9.5 Some detailed calculations for the analytical evaluation of element matric expressions for triangular prismatic elements, mass transport

Diffusion dispersion matrix

$$
\begin{aligned}
D_{ij}^{xx} &= \int_\Omega \frac{\partial N_i}{\partial x}\frac{\partial N_j}{\partial x}\,d\Omega = \int_\Omega \frac{\partial}{\partial x}(N_i^\Delta N_i^t)\frac{\partial}{\partial x}(N_j^\Delta N_j^t)\,d\Omega \\
&= \int_\Omega \left(\frac{\partial N_i^\Delta}{\partial x}N_i^t + N_i^\Delta\frac{\partial N_i^t}{\partial x}\right)\left(\frac{\partial N_j^\Delta}{\partial x}N_j^t + N_j^\Delta\frac{\partial N_j^t}{\partial x}\right)\,d\Omega \\
&= \int_\Omega \frac{\partial N_i^\Delta}{\partial x}\frac{\partial N_j^\Delta}{\partial x}N_i^t N_j^t\,dA\,dz \\
&= \int_\Delta \frac{\partial N_i^\Delta}{\partial x}\frac{\partial N_j^\Delta}{\partial x}\,dA \times \int_z N_i^t N_j^t\,dz \\
&= det[J_{3D}^z]\,A\underbrace{\frac{\partial N_i^\Delta}{\partial x}\frac{\partial N_j^\Delta}{\partial x}}_{\mathbf{K}^{\Delta x}} \times \underbrace{\int_{-1}^{1} N_i^t N_j^t\,dt}_{\mathbf{C}^t} = K_{ij}^{xx}
\end{aligned}
$$

$$
\begin{aligned}
D_{ij}^{xy} &= \int_\Omega \frac{\partial N_i}{\partial x}\frac{\partial N_j}{\partial y}\,d\Omega = \int_\Omega \frac{\partial}{\partial x}(N_i^\Delta N_i^t)\frac{\partial}{\partial y}(N_j^\Delta N_j^t)\,d\Omega \\
&= \int_\Omega \left(\frac{\partial N_i^\Delta}{\partial x}N_i^t + N_i^\Delta\frac{\partial N_i^t}{\partial x}\right)\left(\frac{\partial N_j^\Delta}{\partial y}N_j^t + N_j^\Delta\frac{\partial N_j^t}{\partial y}\right)\,d\Omega \\
&= \int_\Omega \frac{\partial N_i^\Delta}{\partial x}\frac{\partial N_j^\Delta}{\partial y}N_i^t N_j^t\,dA\,dz \\
&= det[J_{3D}^z]\,A\underbrace{\frac{\partial N_i^\Delta}{\partial x}\frac{\partial N_j^\Delta}{\partial y}}_{\mathbf{D}^{\Delta xy}} \times \underbrace{\int_{-1}^{1} N_i^t N_j^t\,dt}_{\mathbf{C}^t}
\end{aligned}
$$

$$
\begin{aligned}
D_{ij}^{xz} &= \int_\Omega \frac{\partial N_i}{\partial x}\frac{\partial N_j}{\partial z}\,d\Omega = \int_\Omega \frac{\partial}{\partial x}(N_i^\Delta N_i^t)\frac{\partial}{\partial z}(N_j^\Delta N_j^t)\,d\Omega \\
&= \int_\Omega \left(\frac{\partial N_i^\Delta}{\partial x}N_i^t + N_i^\Delta\frac{\partial N_i^t}{\partial x}\right)\left(\frac{\partial N_j^\Delta}{\partial z}N_j^t + N_j^\Delta\frac{\partial N_j^t}{\partial z}\right)\,d\Omega \\
&= \int_\Omega \frac{\partial N_i^\Delta}{\partial x}N_j^\Delta N_i^t\frac{\partial N_j^t}{\partial z}\,dA\,dz \\
&= \int_\Delta \frac{\partial N_i^\Delta}{\partial x}N_j^\Delta\,dA\int_z N_i^t\frac{\partial N_j^t}{\partial z}\,dz \\
&= \int_\Delta \frac{\partial N_i^\Delta}{\partial x}N_j^\Delta\,dA\int_{-1}^{1} N_i^t\frac{\partial N_j^t}{\partial t}[J_{3D}^z]^{-1}det[J_{3D}^z]\,dt
\end{aligned}
$$

$$= \underbrace{\int_{\Delta} \frac{\partial N_i^{\Delta}}{\partial x} N_j^{\Delta} dA}_{\mathbf{D}^{\Delta xx}} \times \int_{-1}^{1} N_i^t \frac{\partial N_j^t}{\partial t}\, dt$$

$$\begin{aligned} D_{ij}^{yx} &= \int_{\Omega} \frac{\partial N_i}{\partial y}\frac{\partial N_j}{\partial x}\, d\Omega = \int_{\Omega} \frac{\partial}{\partial y}(N_i^{\Delta} N_i^t)\frac{\partial}{\partial x}(N_j^{\Delta} N_j^t)\, d\Omega \\ &= \int_{\Omega} \left(\frac{\partial N_i^{\Delta}}{\partial y} N_i^t + N_i^{\Delta}\frac{\partial N_i^t}{\partial y}\right)\left(\frac{\partial N_j^{\Delta}}{\partial x} N_j^t + N_j^{\Delta}\frac{\partial N_j^t}{\partial x}\right)\, d\Omega \\ &= \int_{\Omega} \frac{\partial N_i^{\Delta}}{\partial y}\frac{\partial N_j^{\Delta}}{\partial x} N_i^t N_j^t\, dA\, dz \\ &= det[J_{3D}^z]\, A \underbrace{\frac{\partial N_i^{\Delta}}{\partial y}\frac{\partial N_j^{\Delta}}{\partial x}}_{\mathbf{D}^{\Delta yx}} \times \underbrace{\int_{-1}^{1} N_i^t N_j^t\, dt}_{\mathbf{C}^t} \end{aligned}$$

$$\begin{aligned} D_{ij}^{yy} &= \int_{\Omega} \frac{\partial N_i}{\partial y}\frac{\partial N_j}{\partial y}\, d\Omega = \int_{\Omega} \frac{\partial}{\partial y}(N_i^{\Delta} N_i^t)\frac{\partial}{\partial y}(N_j^{\Delta} N_j^t)\, d\Omega \\ &= \int_{\Omega} \left(\frac{\partial N_i^{\Delta}}{\partial y} N_i^t + N_i^{\Delta}\frac{\partial N_i^t}{\partial y}\right)\left(\frac{\partial N_j^{\Delta}}{\partial y} N_j^t + N_j^{\Delta}\frac{\partial N_j^t}{\partial y}\right)\, d\Omega \\ &= \int_{\Omega} \frac{\partial N_i^{\Delta}}{\partial y}\frac{\partial N_j^{\Delta}}{\partial y} N_i^t N_j^t\, dA\, dz \\ &= det[J_{3D}^z]\, A \underbrace{\frac{\partial N_i^{\Delta}}{\partial y}\frac{\partial N_j^{\Delta}}{\partial y}}_{\mathbf{K}^{\Delta y}} \times \underbrace{\int_{-1}^{1} N_i^t N_j^t\, dt}_{\mathbf{C}^t} = K_{ij}^{yy} \end{aligned}$$

$$\begin{aligned} D_{ij}^{yz} &= \int_{\Omega} \frac{\partial N_i}{\partial y}\frac{\partial N_j}{\partial z}\, d\Omega = \int_{\Omega} \frac{\partial}{\partial y}(N_i^{\Delta} N_i^t)\frac{\partial}{\partial z}(N_j^{\Delta} N_j^t)\, d\Omega \\ &= \int_{\Omega} \left(\frac{\partial N_i^{\Delta}}{\partial y} N_i^t + N_i^{\Delta}\frac{\partial N_i^t}{\partial y}\right)\left(\frac{\partial N_j^{\Delta}}{\partial z} N_j^t + N_j^{\Delta}\frac{\partial N_j^t}{\partial z}\right)\, d\Omega \\ &= \int_{\Omega} \frac{\partial N_i^{\Delta}}{\partial y} N_j^{\Delta} N_i^t \frac{\partial N_j^t}{\partial z}\, dA\, dz \\ &= \underbrace{\int_{\Delta} \frac{\partial N_i^{\Delta}}{\partial y} N_j^{\Delta} dA}_{\mathbf{D}^{\Delta yz}} \times \int_{-1}^{1} N_i^t \frac{\partial N_j^t}{\partial t}\, dt \end{aligned}$$

$$D_{ij}^{zx} = \int_{\Omega} \frac{\partial N_i}{\partial z}\frac{\partial N_j}{\partial x}\, d\Omega = \int_{\Omega} \frac{\partial}{\partial z}(N_i^{\Delta} N_i^t)\frac{\partial}{\partial x}(N_j^{\Delta} N_j^t)$$

$$
\begin{aligned}
&= \int_\Omega \left(\frac{\partial N_i^\Delta}{\partial z} N_i^t + N_i^\Delta \frac{\partial N_i^t}{\partial z}\right)\left(\frac{\partial N_j^\Delta}{\partial x} N_j^t + N_j^\Delta \frac{\partial N_j^t}{\partial x}\right)\, d\Omega \\
&= \int_\Omega N_i^\Delta \frac{\partial N_j^\Delta}{\partial x}\frac{\partial N_i^t}{\partial z} N_j^t \, dA\, dz \\
&= \underbrace{\int_\Delta N_i^\Delta \frac{\partial N_j^\Delta}{\partial x} dA}_{\mathbf{D}^{\Delta zx}} \times \int_{-1}^{1} \frac{\partial N_i^t}{\partial t} N_j^t \, dt
\end{aligned}
$$

$$
\begin{aligned}
D_{ij}^{zy} &= \int_\Omega \frac{\partial N_i}{\partial z}\frac{\partial N_j}{\partial y}\, d\Omega = \int_\Omega \frac{\partial}{\partial z}(N_i^\Delta N_i^t)\frac{\partial}{\partial y}(N_j^\Delta N_j^t)\, d\Omega \\
&= \int_\Omega \left(\frac{\partial N_i^\Delta}{\partial z} N_i^t + N_i^\Delta \frac{\partial N_i^t}{\partial z}\right)\left(\frac{\partial N_j^\Delta}{\partial y} N_j^t + N_j^\Delta \frac{\partial N_j^t}{\partial y}\right)\, d\Omega \\
&= \int_\Omega N_i^\Delta \frac{\partial N_j^\Delta}{\partial y}\frac{\partial N_i^t}{\partial z} N_j^t \, dA\, dz \\
&= \underbrace{\int_\Delta N_i^\Delta \frac{\partial N_j^\Delta}{\partial y} dA}_{\mathbf{D}^{\Delta zy}} \times \int_{-1}^{1} \frac{\partial N_i^t}{\partial t} N_j^t \, dt
\end{aligned}
$$

$$
\begin{aligned}
D_{ij}^{zz} &= \int_\Omega \frac{\partial N_i}{\partial z}\frac{\partial N_j}{\partial z}\, d\Omega = \int_\Omega \frac{\partial}{\partial z}(N_i^\Delta N_i^t)\frac{\partial}{\partial z}(N_j^\Delta N_j^t)\, d\Omega \\
&= \int_\Omega \left(\frac{\partial N_i^\Delta}{\partial z} N_i^t + N_i^\Delta \frac{\partial N_i^t}{\partial z}\right)\left(\frac{\partial N_j^\Delta}{\partial z} N_j^t + N_j^\Delta \frac{\partial N_j^t}{\partial z}\right)\, d\Omega \\
&= \int_\Omega N_i^\Delta N_j^\Delta \frac{\partial N_i^t}{\partial z}\frac{\partial N_j^t}{\partial z}\, dA\, dz \\
&= [J_{3D}^z]^{-1} \underbrace{\int_\Delta N_i^\Delta N_j^\Delta dA}_{\mathbf{K}^{\Delta z}} \times \int_{-1}^{1} \frac{\partial N_i^t}{\partial t}\frac{\partial N_j^t}{\partial t}\, dt = K_{ij}^{zz}
\end{aligned}
$$

$$
\int_{-1}^{1} N_i^t \frac{\partial N_j^t}{\partial t}\, dt = \int_{-1}^{1} \begin{bmatrix}
N_1^t\frac{\partial N_1^t}{\partial t} & N_1^t\frac{\partial N_1^t}{\partial t} & N_1^t\frac{\partial N_1^t}{\partial t} & N_1^t\frac{\partial N_2^t}{\partial t} & N_1^t\frac{\partial N_2^t}{\partial t} & N_1^t\frac{\partial N_2^t}{\partial t} \\
N_1^t\frac{\partial N_1^t}{\partial t} & N_1^t\frac{\partial N_1^t}{\partial t} & N_1^t\frac{\partial N_1^t}{\partial t} & N_1^t\frac{\partial N_2^t}{\partial t} & N_1^t\frac{\partial N_2^t}{\partial t} & N_1^t\frac{\partial N_2^t}{\partial t} \\
N_1^t\frac{\partial N_1^t}{\partial t} & N_1^t\frac{\partial N_1^t}{\partial t} & N_1^t\frac{\partial N_1^t}{\partial t} & N_1^t\frac{\partial N_2^t}{\partial t} & N_1^t\frac{\partial N_2^t}{\partial t} & N_1^t\frac{\partial N_2^t}{\partial t} \\
N_2^t\frac{\partial N_1^t}{\partial t} & N_2^t\frac{\partial N_1^t}{\partial t} & N_2^t\frac{\partial N_1^t}{\partial t} & N_2^t\frac{\partial N_2^t}{\partial t} & N_2^t\frac{\partial N_2^t}{\partial t} & N_2^t\frac{\partial N_2^t}{\partial t} \\
N_2^t\frac{\partial N_1^t}{\partial t} & N_2^t\frac{\partial N_1^t}{\partial t} & N_2^t\frac{\partial N_1^t}{\partial t} & N_2^t\frac{\partial N_2^t}{\partial t} & N_2^t\frac{\partial N_2^t}{\partial t} & N_2^t\frac{\partial N_2^t}{\partial t} \\
N_2^t\frac{\partial N_1^t}{\partial t} & N_2^t\frac{\partial N_1^t}{\partial t} & N_2^t\frac{\partial N_1^t}{\partial t} & N_2^t\frac{\partial N_2^t}{\partial t} & N_2^t\frac{\partial N_2^t}{\partial t} & N_2^t\frac{\partial N_2^t}{\partial t}
\end{bmatrix} dt
$$

$$\int_{-1}^{1} \frac{\partial N_i^t}{\partial t} N_j^t \, dt = \int_{-1}^{1} \begin{bmatrix} \frac{\partial N_1^t}{\partial t} N_1^t & \frac{\partial N_1^t}{\partial t} N_1^t & \frac{\partial N_1^t}{\partial t} N_1^t & \frac{\partial N_1^t}{\partial t} N_2^t & \frac{\partial N_1^t}{\partial t} N_2^t & \frac{\partial N_1^t}{\partial t} N_2^t \\ \frac{\partial N_1^t}{\partial t} N_1^t & \frac{\partial N_1^t}{\partial t} N_1^t & \frac{\partial N_1^t}{\partial t} N_1^t & \frac{\partial N_1^t}{\partial t} N_2^t & \frac{\partial N_1^t}{\partial t} N_2^t & \frac{\partial N_1^t}{\partial t} N_2^t \\ \frac{\partial N_1^t}{\partial t} N_1^t & \frac{\partial N_1^t}{\partial t} N_1^t & \frac{\partial N_1^t}{\partial t} N_1^t & \frac{\partial N_1^t}{\partial t} N_2^t & \frac{\partial N_1^t}{\partial t} N_2^t & \frac{\partial N_1^t}{\partial t} N_2^t \\ \frac{\partial N_2^t}{\partial t} N_1^t & \frac{\partial N_2^t}{\partial t} N_1^t & \frac{\partial N_2^t}{\partial t} N_1^t & \frac{\partial N_2^t}{\partial t} N_2^t & \frac{\partial N_2^t}{\partial t} N_2^t & \frac{\partial N_2^t}{\partial t} N_2^t \\ \frac{\partial N_2^t}{\partial t} N_1^t & \frac{\partial N_2^t}{\partial t} N_1^t & \frac{\partial N_2^t}{\partial t} N_1^t & \frac{\partial N_2^t}{\partial t} N_2^t & \frac{\partial N_2^t}{\partial t} N_2^t & \frac{\partial N_2^t}{\partial t} N_2^t \\ \frac{\partial N_2^t}{\partial t} N_1^t & \frac{\partial N_2^t}{\partial t} N_1^t & \frac{\partial N_2^t}{\partial t} N_1^t & \frac{\partial N_2^t}{\partial t} N_2^t & \frac{\partial N_2^t}{\partial t} N_2^t & \frac{\partial N_2^t}{\partial t} N_2^t \end{bmatrix} dt$$

$$\begin{aligned}
\int_{-1}^{1} N_1^t \frac{\partial N_1^t}{\partial t} \, dt &= +\frac{1}{2} \int_{-1}^{1} \frac{1+t}{2} dt = +\frac{1}{4} \left| t + \frac{1}{2} t^2 \right|_{-1}^{1} = +\frac{1}{4} \left(1 + \frac{1}{2} + 1 + \frac{1}{2} \right) = +\frac{1}{2} \\
\int_{-1}^{1} N_1^t \frac{\partial N_2^t}{\partial t} \, dt &= -\frac{1}{2} \int_{-1}^{1} \frac{1+t}{2} dt = -\frac{1}{4} \left| t + \frac{1}{2} t^2 \right|_{-1}^{1} = -\frac{1}{4} \left(1 + \frac{1}{2} + 1 - \frac{1}{2} \right) = -\frac{1}{2} \\
\int_{-1}^{1} N_2^t \frac{\partial N_1^t}{\partial t} \, dt &= +\frac{1}{2} \int_{-1}^{1} \frac{1-t}{2} dt = +\frac{1}{4} \left| t - \frac{1}{2} t^2 \right|_{-1}^{1} = +\frac{1}{4} \left(1 - \frac{1}{2} + 1 + \frac{1}{2} \right) = +\frac{1}{2} \\
\int_{-1}^{1} N_2^t \frac{\partial N_2^t}{\partial t} \, dt &= -\frac{1}{2} \int_{-1}^{1} \frac{1-t}{2} dt = -\frac{1}{4} \left| t - \frac{1}{2} t^2 \right|_{-1}^{1} = -\frac{1}{4} \left(1 - \frac{1}{2} + 1 + \frac{1}{2} \right) = -\frac{1}{2}
\end{aligned}$$

$$\int_{-1}^{1} N_i^t \frac{\partial N_j^t}{\partial t} \, dt = \frac{1}{2} \begin{bmatrix} 1 & 1 & 1 & -1 & -1 & -1 \\ 1 & 1 & 1 & -1 & -1 & -1 \\ 1 & 1 & 1 & -1 & -1 & -1 \\ 1 & 1 & 1 & -1 & -1 & -1 \\ 1 & 1 & 1 & -1 & -1 & -1 \\ 1 & 1 & 1 & -1 & -1 & -1 \end{bmatrix}$$

$$\int_{-1}^{1} \frac{\partial N_i^t}{\partial t} N_j^t \, dt = \frac{1}{2} \begin{bmatrix} 1 & 1 & 1 & 1 & 1 & 1 \\ 1 & 1 & 1 & 1 & 1 & 1 \\ 1 & 1 & 1 & 1 & 1 & 1 \\ -1 & -1 & -1 & -1 & -1 & -1 \\ -1 & -1 & -1 & -1 & -1 & -1 \\ -1 & -1 & -1 & -1 & -1 & -1 \end{bmatrix}$$

Tracer Advection Matrix

$$
\begin{aligned}
B^x_{ij} &= \int_\Omega (N^\Delta_i N^t_i)\frac{\partial}{\partial x}(N^\Delta_j N^t_j)\,d\Omega = \int_\Omega N^\Delta_i N^t_i \left(\frac{\partial N^\Delta_j}{\partial x}N^t_j + N^\Delta_j \frac{\partial N^t_j}{\partial x}\right) d\Omega \\
&= \int_\Omega N^\Delta_i \frac{\partial N^\Delta_j}{\partial x} N^t_i N^t_j \,d\Omega = \int_\Delta N^\Delta_i \frac{\partial N^\Delta_j}{\partial x}\,dA \times \int_z N^t_i N^t_j \,dz \\
&= \int_\Delta N^\Delta_i \frac{\partial N^\Delta_j}{\partial x}\,dA \times \int_{-1}^{1} N^t_i N^t_j \, det[J^z_{3D}]\,dt \\
&= det[J^z_{3D}] \underbrace{\int_\Delta N^\Delta_i \frac{\partial N^\Delta_j}{\partial x}\,dA}_{\mathbf{B}^{\Delta x}} \times \underbrace{\int_{-1}^{1} N^t_i N^t_j \,dt}_{\mathbf{C}^t}
\end{aligned}
$$

$$
\begin{aligned}
B^z_{ij} &= \int_\Omega (N^\Delta_i N^t_i)\frac{\partial}{\partial z}(N^\Delta_j N^t_j)\,d\Omega = \int_\Omega N^\Delta_i N^t_i \left(\frac{\partial N^\Delta_j}{\partial z}N^t_j + N^\Delta_j \frac{\partial N^t_j}{\partial z}\right) d\Omega \\
&= \int_\Omega N^\Delta_i N^\Delta_j N^t_i \frac{\partial N^t_j}{\partial z}\,d\Omega = \int_\Delta N^\Delta_i N^\Delta_j \,dA \times \int_z N^t_i \frac{\partial N^t_j}{\partial z}\,dz \\
&= \int_\Delta N^\Delta_i N^\Delta_j \,dA \times \int_{-1}^{1} N^t_i \frac{\partial N^t_j}{\partial t}[J^z_{3D}]^{-1}\, det[J^z_{3D}]\,dt \\
&= \underbrace{\int_\Delta N^\Delta_i N^\Delta_j \,dA}_{\mathbf{C}^\Delta} \times \int_{-1}^{1} N^t_i \frac{\partial N^t_j}{\partial t}\,dt
\end{aligned}
$$

$$
\begin{aligned}
\mathbf{b}^{\Delta x} &= \frac{\partial N^\Delta_j}{\partial x}\int_\Delta N^\Delta_i \,dA \\
&= \frac{\partial N^\Delta_j}{\partial x}\int_\Delta N^\Delta_i \,dA \\
&= \begin{bmatrix} (y_2 - y_3) \\ (y_3 - y_1) \\ (y_1 - y_2) \end{bmatrix} \frac{1}{2A} \begin{bmatrix} \frac{1!\,0!\,0!}{(1+0+0+2)!}2A \\ \frac{0!\,1!\,0!}{(0+1+0+2)!}2A \\ \frac{0!\,0!\,1!}{(0+0+1+2)!}2A \end{bmatrix} \\
&= \begin{bmatrix} (y_2 - y_3) \\ (y_3 - y_1) \\ (y_1 - y_2) \end{bmatrix} \frac{1}{2A} \begin{bmatrix} 1 \\ 1 \\ 1 \end{bmatrix} \frac{1}{3}A
\end{aligned}
$$

9.6 Exemplary source code of the implementation for the evaluation of element matrices

Numerical scheme

```
/* Schleife ueber GaussPunkte */
for (i = 0; i < anzgplin; i++)  {
  for (j = 0; j < anzgptri; j++)  {

  r = MXPGaussPktTri(anzgptri,j,0);
  s = MXPGaussPktTri(anzgptri,j,1);
  t = MXPGaussPkt(anzgplin,i);

  CalcPrismElementJacobiMatrix(index, r, s, t, invjac, &detjac);
  MTranspoMat(invjac, 3, 3, TransInvjac);

  /* Wichtung der Gausspunkte */
  fkt = MXPGaussFktTri(anzgptri, j) * MXPGaussFkt(anzgplin,i) * detjac;

  /*------------------------------------------------------------------*/
  /*---- Capacitance matrix ------------------------------------------*/
  /*------------------------------------------------------------------*/
  /* Omega T * Omega * fkt */
  MOmegaPrism(OmPrism, r, s, t);
  MMultVecVec(OmPrism, nn, OmPrism, nn, zwi, nn, nn);
  for (l = 0; l < nn2; l++)  {
    capacitance_matrix[l] += (zwi[l] * fkt);
  }
  /*------------------------------------------------------------------*/
  /*---- Conductance matrix ------------------------------------------*/
  /*------------------------------------------------------------------*/
  /* tkmyt = (J^-1)T * (K/my) * J^-1 */
  MMultMatMat(kmmy, 3, 3, invjac, 3, 3, zwa, 3, 3);
  MMultMatMat(TransInvjac, 3, 3, zwa, 3, 3, tkmyt, 3, 3);

  /* GradOmega T */
  MGradOmegaPrism( r, s, t, GradOmPrism);             /*3Zeilen 6 Spalten*/
  MTranspoMat(GradOmPrism, 3, nn, TransGradOmPrism);  /*6Zeilen 3 Spalten*/
  /* GradOmega T * tkmyt */
  MMultMatMat(TransGradOmPrism,nn,3,tkmyt,3,3, zwi, nn, 3);
  /* GradOmega T * tkmyt * GradOmega */
  MMultMatMat(zwi,nn,3,GradOmPrism,3,nn,zwu,6,6);
  /* GradOmega T * tkmyt * GradOmega * fkt */
  for (l = 0; l < nn2; l++) {
    conductance_matrix[l] += (zwu[l] * fkt);
```

```
  }

  }  /*Ende Schleife über Anzahl der GaussPunkte im Dreieck */
}    /*Ende Schleife über Anzahl der GaussPunkte in z Richtung*/
```

Analytical scheme

```
/*-------------------------------------------------------------------------*/
/*---- Capacitance matrix -------------------------------------------------*/
/*-------------------------------------------------------------------------*/
Get_NTrinangle_x_NTrinangle(index, Tri_x_Tri);
MMultMatSkalar(Tri_x_Tri,DetJac3Dz,3,3);
GetPriMatFromTriMat(Tri_x_Tri, capacitance_matrix);
MMultMatMat2(capacitance_matrix, 6, 6, Ct, capacitance_matrix);
MMultMatSkalar(capacitance_matrix,storativity,6,6);

/*-------------------------------------------------------------------------*/
/*---- Conductance matrix -------------------------------------------------*/
/*-------------------------------------------------------------------------*/
/* Calc Kijxx */
fac1 = DetJac3Dz * area;
CalcGradXTri(index, GradXTri);
MMultVecVec(GradXTri,3,GradXTri,3,GradXTri_x_GradXTri,3,3);
MMultMatSkalar(GradXTri_x_GradXTri,fac1,3,3);
GetPriMatFromTriMat(GradXTri_x_GradXTri, Kijxx);
MMultMatMat2(Kijxx, 6, 6, Ct, Kijxx);
MMultMatSkalar(Kijxx,k_xx,6,6);

/* Calc Kijyy */
CalcGradYTri(index, GradYTri);
MMultVecVec(GradYTri,3,GradYTri,3,GradYTri_x_GradYTri,3,3);
MMultMatSkalar(GradYTri_x_GradYTri,fac1,3,3);
GetPriMatFromTriMat(GradYTri_x_GradYTri, Kijyy);
MMultMatMat2(Kijyy, 6, 6, Ct, Kijyy);
MMultMatSkalar(Kijyy,k_yy,6,6);

/* Calc Kijzz */
Get_NTrinangle_x_NTrinangle(index, Tri_x_Tri);
MMultMatSkalar(Tri_x_Tri,InvJac3Dz,3,3);
GetPriMatFromTriMat(Tri_x_Tri, Kijzz);
MMultMatMat2(Kijzz, 6, 6, GradNGradN, Kijzz);
MMultMatSkalar(Kijzz,k_zz,6,6);

for (i=0;i<nn2;i++) {
  conductance_matrix[i] = Kijxx[i] + Kijyy[i] + Kijzz[i];
}
```

9.7 Finite difference equations for channel flow

explicit FTCS scheme

$$\begin{aligned}(a_i^n + 2b_i^n h_i^n)\frac{h_i^{n+1} - h_i^n}{\Delta t} &+ \\ \frac{a_{i+1}^n u_{i+1}^n h_{i+1}^n - a_{i-1}^n u_{i-1}^n h_{i-1}^n}{2\Delta s} &+ \\ \frac{b_{i+1}^n u_{i+1}^n (h^2)_{i+1}^n - b_{i-1}^n u_{i-1}^n (h^2)_{i-1}^n}{2\Delta s} &= 0\end{aligned}$$

$$\begin{aligned}(a_i^n + 2b_i^n h_i^n)\frac{h_i^{n+1}}{\Delta t} &= \\ (a_i^n + 2b_i^n h_i^n)\frac{h_i^n}{\Delta t} &- \\ \frac{a_{i+1}^n u_{i+1}^n h_{i+1}^n - a_{i-1}^n u_{i-1}^n h_{i-1}^n}{2\Delta s} &- \\ \frac{b_{i+1}^n u_{i+1}^n (h^2)_{i+1}^n - b_{i-1}^n u_{i-1}^n (h^2)_{i-1}^n}{2\Delta s}&\end{aligned}$$

$$\begin{aligned}h_i^{n+1} &= h_i^n \\ &- \frac{a_{i+1}^n u_{i+1}^n h_{i+1}^n - a_{i-1}^n u_{i-1}^n h_{i-1}^n}{a_i^n + 2b_i^n h_i^n}\frac{\Delta t}{2\Delta s} \\ &- \frac{b_{i+1}^n u_{i+1}^n (h^2)_{i+1}^n - b_{i-1}^n u_{i-1}^n (h^2)_{i-1}^n}{a_i^n + 2b_i^n h_i^n}\frac{\Delta t}{2\Delta s}\end{aligned}$$

explicit upstream scheme

$$\begin{aligned}\frac{u_i^{n+1} - u_i^n}{\Delta t} + u_i^n\frac{u_i^n - u_{i-1}^n}{\Delta s} + g\frac{h_i^n - h_{i-1}^n}{\Delta s} &= g(S_0 - S_f), \quad u_i^n \geq 0 \\ \frac{u_i^{n+1} - u_i^n}{\Delta t} + u_i^n\frac{u_{i+1}^n - u_i^n}{\Delta s} + g\frac{h_i^n - h_{i-1}^n}{\Delta s} &= g(S_0 - S_f), \quad u_i^n < 0\end{aligned}$$

$$\begin{aligned}u^{n+1} &= u_i^n - u_i^n(u_i^n - u_{i-1}^n)\frac{\Delta t}{\Delta s} - g(h_i^n - h_{i-1}^n)\frac{\Delta t}{\Delta s} + g(S_0 - S_f)\Delta t, \quad u_i^n \geq 0 \\ u^{n+1} &= u_i^n - u_i^n(u_{i+1}^n - u_i^n)\frac{\Delta t}{\Delta s} - g(h_i^n - h_{i-1}^n)\frac{\Delta t}{\Delta s} + g(S_0 - S_f)\Delta t, \quad u_i^n < 0\end{aligned}$$

$$\begin{aligned}\frac{u_i^{n+1} - u_i^n}{\Delta t} + u_i^n\frac{u_i^n - u_{i-1}^n}{\Delta s} + g\frac{h_i^n - h_{i-1}^n}{\Delta s} &= g(S_0 - S_f), \quad u_i^n \geq 0 \\ \frac{u_i^{n+1} - u_i^n}{\Delta t} + u_i^n\frac{u_{i+1}^n - u_i^n}{\Delta s} + g\frac{h_i^n - h_{i-1}^n}{\Delta s} &= g(S_0 - S_f), \quad u_i^n < 0\end{aligned}$$

$$u^{n+1} = u_i^n - u_i^n(u_i^n - u_{i-1}^n)\frac{\Delta t}{\Delta s} - g(h_i^n - h_{i-1}^n)\frac{\Delta t}{\Delta s} + g(S_0 - S_f)\Delta t, \quad u_i^n \geq 0$$

$$u^{n+1} = u_i^n - u_i^n(u_{i+1}^n - u_i^n)\frac{\Delta t}{\Delta s} - g(h_i^n - h_{i-1}^n)\frac{\Delta t}{\Delta s} + g(S_0 - S_f)\Delta t, \quad u_i^n < 0$$

9.8 List of publications

Beinhorn, M., Kolditz, O., Sauter, M., May 2002. Density dependent flow modelling: Application to the Jordan Valley. In 17th Salt Water Intrusion Meeting, Delft, The Netherlands, pp. 155-161.

Beinhorn, M., Kolditz, O., 2003. Triangular prismatic elements PART I: Numerical integration. Technical report, Nr. 2003-2, Center for Applied Geosciences, University of Tübingen.

Beinhorn, M., Kolditz, O., 2003. Triangular prismatic elements PART II: Analytical integration. Technical report, Nr. 2003-30, Center for Applied Geosciences, University of Tübingen.

Beinhorn, M., Guttman, J. S., Sauter, M., Toll, M., Kolditz, O., April 2004. Groundwater modelling of the shallow aquifer in the Jericho area. In 5th Int Symposium on the Eastern Mediterranean Geology, Thessaloniki, Greece, pp. 1483-1486

Beinhorn, M., Kolditz, O., June 2004. Object-oriented approach to preprocessing and process modelling in water resources, application to the Jericho area. In Proceedings of the 15th International Conference on Computational Methods in Water Resources (CMWR XV), Chapel Hill, NC, USA, Elsevier, pp. 1067-1077.

Beinhorn, M., Kolditz, O., 2004. Object oriented approach to groundwater modelling. submitted to Computers and Geosciences.

Beinhorn, M., Dietrich, P., Kolditz, O., 2004. 3-D numerical evaluation of density effects on tracer tests. submitted to Journal of Contaminant Hydrology.

Beinhorn, M., Guttman, J., Kolditz, O., 2004. Groundwater flow and transport model of the Jericho area. Technical report, Nr. 2004-14, Center for Applied Geosciences, University of Tübingen.

Kolditz, O., Beinhorn, M., Liedl, R., July 2004. An object-oriented groundwater / river model. In: Groundwater Quality, 4th International Conference, Ontario, Canada.

Chen, C., Sawarieh, A., Kalbacher, T., Beinhorn, M., Wang, W. and Kolditz, O., 2004. A GIS based 3-D Hydrosystem Model Application to the Zarqa Main/Jiza area in Central Jordan, Journal of Environmental Hydrology (accepted for publication)